UNIVERSITITA DEGLI STUDI DI UDINE
DIPARTIMENTO DI MATEMATICA & INFORMATICA

DOCTORATE OF PHILOSOPHY
IN MATHEMATICS & PHYSICS
XXVII CYCLE

COMPARATIVE INVESTIGATION OF SILICON PHOTOMULTIPLIERS AS POSSIBLE PHOTON DETECTORS FOR THE CHERENKOV TELESCOPE ARRAY

SUPERVISOR: Prof. **Alessandro De Angelis**

CO-SUPERVISOR: Prof. **Diego Cauz**
Prof. **Giovanni Pauletta**

CANDIDATE: Carlo Stella

To my little girls.

Index

List of figures

Introduction

The study of universe and its evolution stimulates the scientific observation of radiation in a spectrum ranging, from radio waves to ultra high energy gamma rays. While the study of visible radiation has a long history, the observation of gamma rays by means of satellites, for low energy, and ground telescopes, for high energy, was born at the end of XX century. This new type of astronomy allows one to study gamma-ray sources such as stellar nurseries, pulsars and active galactic nuclei and to investigate physics phenomena such as dark matter and quantum gravity.

Although the gamma radiation is absorbed in the atmosphere, the Imaging Air Cherenkov Telescopes (IACT) can observe it indirectly. When the radiation crosses the atmosphere, it produces secondary particles which generate cherenkov radiation in UV and visible band. This radiation is detected at ground level by cherenkov telescopes whose mirror systems focus the radiation on suitable photo-detector systems. In the current IACTs, e.g. MAGIC or H.E.S.S., the photo sensors are the well-established photomultiplier tube (PMT) technology, which have a high efficiency light electrical pulse and are sensitive to UV and visible radiation.

One of most interesting improvements in CTA observatory will be the use of silicon photomultipliers (SiPM) as photon detectors for the telescope cameras. SiPMs are one of the most recent developments in the field of fast semiconductor photo-sensors. A SiPM is essentially a finely pixelated matrix of Geiger-mode avalanche photodiodes (GM-APDs) where each GM-APD cell

is a reverse-biased p-n junction which operates above breakdown voltage (V_{bd}). In this mode, photon or thermal excitation in the depleted region will produce a pair of charge carriers (electron-hole) which, through impact ionization, can trigger an electron-hole avalanche saturating the active area. In the most common SiPM a passive quenching, employed to manage the avalanche, resets the cell to a quiet state so that it becomes photosensitive again. SiPMs have many key advantages compared with photomultiplier tube technology, such as low voltage operation (typically $\sim$ 20 - 100 Volts), low power consumption ($\leq$ 50 μW/mm^2), resistance to high light levels (critical to the continuation of observation during bright moonlight periods with cherenkov telescopes), excellent pulse height resolution, insensitivity to magnetic fields and single photon sensitivity. However, these devices have also some negative aspects as dark noise (fake pulses caused by random thermal excitation in the depleted region), cross-talk (by-product of a pixel avalanche is photons which can propagate inside the SiPM and generate fake avalanche in other pixels) and afterpulses (charger carriers trapped during the avalanche, which can generate a second avalanche in the same pixel).

SiPMs stand as a very promising technology to replace current photomultiplier tube (PMT) based cameras and many companies (e.g. Excelitas, FBK AdvanSiD, Hamamatsu Photonics, Ketek, SensL) produce a large number of different types of SiPMs. The aim of this dissertation is to investigate what is being offered by different manufacturers and to perform a comparative investigation of their characteristics, in order to evaluate how well they could fulfil CTA requirements.

Both static and dynamic properties were studied as a function of temperature under controlled conditions by performing the measurements as a function of temperature in a climatic chamber in which the humidity was controlled by a flux of purified dry air. Control and data acquisition were managed by LabView and, wherever possible, the procedure was automated and organized

such as to enable a number of SiPMs to be characterized in sequence by a system of relays. Numerical and analytical methods were applied to the data collected, to estimate the SiPMs' characteristics as breakdown voltage, dark noise frequency, cross-talk and gain.

The results highlight the differences in the behaviour of SiPMs produced by different manufacturers. Their comparison will be useful to identify SiPM devices that would be most suitable for the CTA projects and more for IACT technique. Moreover, the assembled probe station is a new, cheap, "fast", scalable and modular system to define the features of silicon photomultipliers with the potential to become a useful instrument in mass SiPMs' characterization.

1

Very High Energy Gamma-Ray Astrophysics

In the history of astronomy and astrophysics new ways to see the universe always generated progress in the knowledge of cosmos. Galileo Galilei opened up a new era of astronomical observation thanks to the use of his telescope, showing how the universe can be interesting if looked with the use of new techniques and technology.

Examples in astrophysics and astronomy are the use of photographic imaging techniques coupled with optical telescopes, which gave rise to modern cosmology. The use of electrometer and cloud chamber for astrophysical observation and the adoption of photographic emulsion as tracking device opened up the pioneering observation of cosmic rays. The new radio telescope allowed the universe in the radiowave range and led to the discovery of radio galaxies, pulsars and quasars, extreme energetic objects hidden in the visible . The employment of infrared-detectors uncovered the dense interstellar dust clouds, birthplace of stars, and gave experimental access to the very first phases of stellar evolution, long before hydrogen burning starts.

The high energy and very high energy radiations (X-ray and γ-ray) do not reach the earth at ground level, therefore their direct detection required

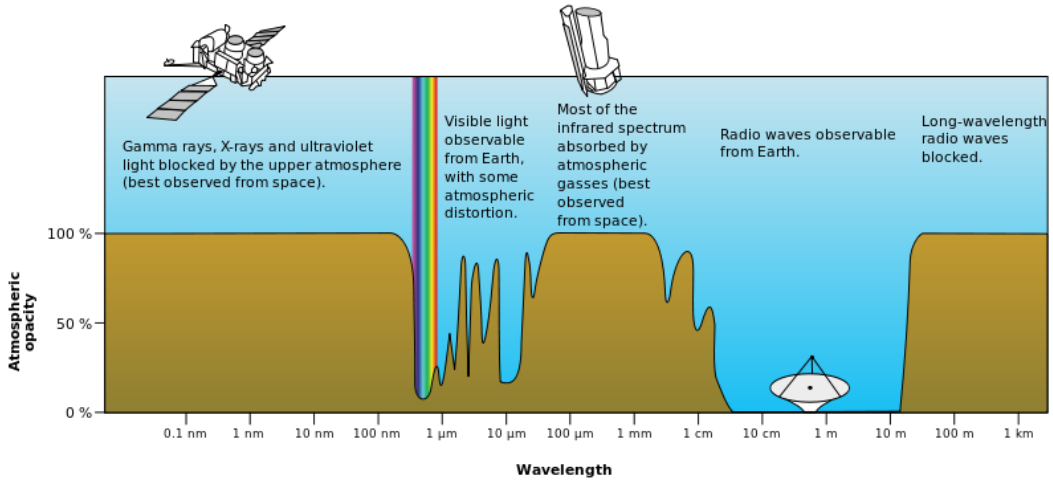

Figure 1.1: Atmospheric opacity at the different wavelenghts.

instruments outside the atmosphere. X-ray astrophysics begin with the use of rocket and satellite technology and the Sco X-1 was the first X-ray source discovered in 1962 by R. Giacconi and B. Rossi with rocket-borne Geiger counters [1].

The early steps of γ-ray astrophysics concentrated on direct observation using balloon-technique and satellite detectors, but the relevant results came with indirect observation using the Imaging Atmospheric Cherekov Telescope technique (IACTt). Following the first observations of atmospheric Cherenkov radiation and the theoretical predictions for ground-based (indirect) detection of cosmic γ-rays, the Cherenkov telescope (CT), based on IACTt, established a firm result in 1989, with the discovery of the first steady source of γ photons at very high energy (VHE, roughly more than 10 GeV), the Crab Nebula, which became the standard candle for the subsequent γ sources.

γ-rays with energies from GeV to TeV cannot conceivably be generated by thermal emission from hot celestial objects. For this reason γ-ray astronomy is a privileged window on the "non-thermal" Universe and constituents, such as Supernovae, Supernova Remnants, Black Holes, Active Galactic Nuclei and

Gamma Ray Burst (respectively SN, SNR, BH, AGN and GRB hereafter).

1.1 The Gamma-Ray Window

Cosmic-rays are photons and particles with high energy (roughly more than 10^6 eV) which strike the Earth from the space. Their primary composition consist of charged particle as proton (roughly 90%), helium nuclei (approximately 9%), ionized heavier elements (about 1%) and electrons ($e^{\pm}/p \sim 1\%$), radiation component is a tiny fraction of total cosmic-ray ($\gamma/p \sim 0.1\%$).

Figure 1.2 show the flux of cosmic-ray as a function of energy, which is referred to as the *energy spectrum*. The change of slope around $10^{15.5}$ eV is called the "knee" of the spectrum, while the variation which occurs around $10^{18.5}$ eV is referred to as the "ankle". The energy spectrum show a dependence on the energy E of the particle,which can be approximate by a power law $dN/dE \propto E^{-\alpha}$ with $\alpha \simeq -2.5$ before the knee and after the ankle, and $\alpha \simeq -3$ between the knee and the ankle.

Cosmic protons with energy below the knee have probably confined inside our Galaxy by its magnetic field, which is of the order of 1 μG. Charged particle with energies above 10^{17} eV might denote their extragalactic origin, because the galactic magnetic field could not trap them. In both case the initial direction of protons is deflected by galactic field, so it is difficult to find out.

The source positions of γ-rays are easier and more reliable to determine than protons, because photon are not curved by magnetic field. For this reason and their wide energy range, γ-rays are incredible "messengers" from high energy Universe.

In this work γ-rays are classified with energy ranges:

- low energy (LE) for γ-ray energies ranging from 1 MeV to 10 MeV;

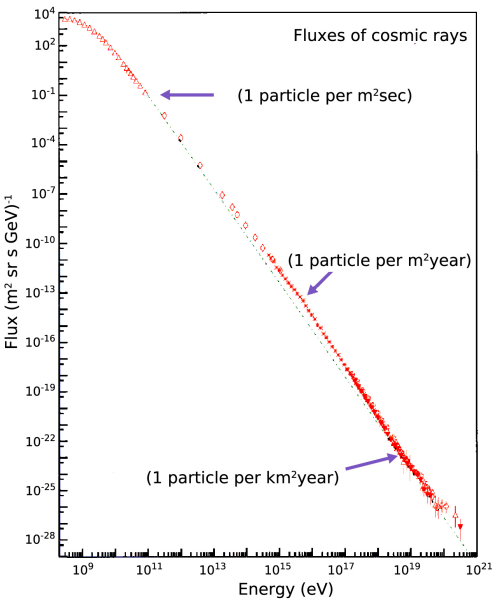

Figure 1.2: Energy spectrum of cosmic rays.

- medium energy (ME) for γ-ray energies ranging from 10 MeV to 30 MeV;
- high energy (HE) for γ-ray energies ranging from 30 MeV to 30 GeV;
- very high energy (VHE) for γ-ray energies ranging from 30 GeV to 30 TeV;
- ultra high energy (UHE) for γ-ray energies ranging from 30 TeV to 30 PeV;
- extremely high energy (EHE) for γ-ray energies above 30 PeV.

The lower energies corresponds to the region of nuclear γ emission, while the radiation in the highest band can be generated, for example, when highly relativistic particles, accelerated in the gigantic shock waves, interact with photons and magnetic fields.

VHE γ-rays can be used to monitor γ-ray sources, to explore distant regions of our own Galaxy or even other galaxies, since they are not deflected by magnetic field. Moreover, the energy of highest band of γ-rays have energies far beyond the terrestrial accelerators, so they can be used to probe fundamental physics as Dark Matter, Quantum Gravity or Super Symmetry.

1.2 Production Process of Cosmic Gamma Rays

The emission of γ-ray is always associated to the presence of accelerated charged particles in VHE regime. For this reason, the search for cosmic sources of γ-rays is related to the identification of the regions in the Universe where high energy hadrons and leptons (and possibly even exotic particles) are in large quantity.

Gravity is the main source for HE particle emission by astronomical objects like AGN, while it is currently believed that the particles with energy up to 10^{15} - 10^{16} eV are accelerated in galactic objects like SNR. Particles with energy between the knee and the ankle can have various origins while the particles with energy above the ankle value originated most probably from extra-galactic sources.

There are several possible processes for the production of γ-ray radiation from energetic particles, each of which takes place in specific energy ranges. Normally, several of these mechanisms co-act to shape the γ-ray outflow from a given source. In addition, the presence of gas, plasma and radiation fields in the vicinity of the emitters can strongly shape the observed emission.

The most relevant processes of energy transmission from charge particles to γ-rays are electron bremsstrahlung, Inverse Compton scattering (IC) and Synchrotron Radiation (SR). Other primary γ photons are generated by π^0 decay (the main γ production mechanism in a hadronic environment) or nuclear transitions; there is also the possibility of obtaining characteristic photon si-

gnals from annihilation or decay of heavy particles or from the self-annihilation of the still unknown Dark Matter. The main processes are briefly recalled in the following.

1.2.1 Leptonic Models

When a relativistic electron is moving inside a magnetic field H, it is driven by Lorentz force to follow a curved trajectory. Due to continuous acceleration towards the center of its orbit, the electron will lose energy emitting synchrotron radiation strongly beamed into a cone of half angle $\alpha \sim m_e c^2/E$ (fig. 1.3a), where m_e is the electron mass and E its energy.

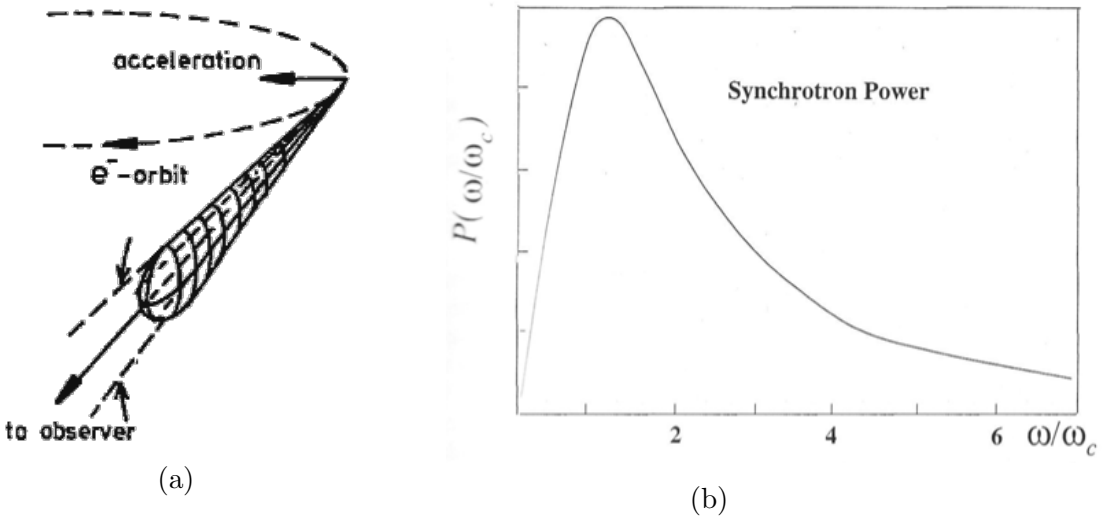

(a) (b)

Figure 1.3: γ-ray emission cone from synchrotron radiation (*a*) and synchrotron radiation power as a function of emission radiation frequency (*b*).

At relativistic energies the radiation occurs with a continuum spectral distribution peaked about w_c (fig. 1.3b), the critical frequency at which the maximum power is emitted, expressed as

$$w_c = (\frac{3}{2})(\frac{eH}{mc})\gamma^2 \sin\theta \tag{1.1}$$

with θ the angle formed between the electron velocity and the direction of the magnetic field H and γ the Lorentz factor [2]. In typical galactic magnetic fields, the energy can be approximated by

$$E_\gamma \simeq 0.05(\frac{E_e}{TeV})^2(\frac{H}{3\mu G})eV. \tag{1.2}$$

Equation 1.2 shows that high energy SR is produced in astronomical regions with very strong magnetic fields, e.g. close to a neutron star surface (where H $\geq 10^{12}$ G).

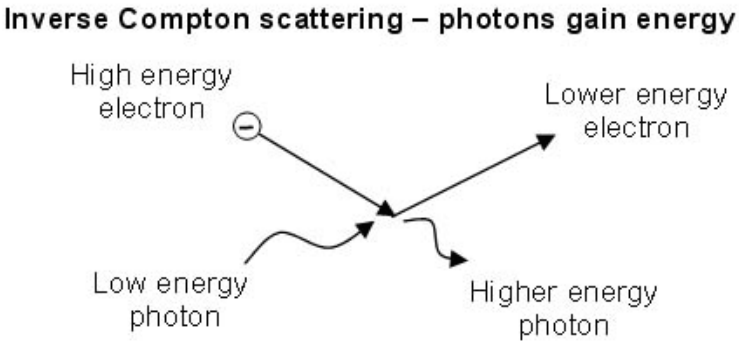

Figure 1.4: Inverse comptin scattering.

The inverse compton process is the other important production mechanism of γ-rays in leptonic model. Figure 1.4 shows a typical IC scattering in which a low energy photon is hit by a relativistic particle, tipically electrons. With this process a considerable fraction of the electron energy can be transferred to the photon. The scattered radiation has a continuous spectrum with a maximum corresponding to head-on collision which can be expressed by the formula:

$$\varepsilon_{max} = 4\gamma^2 E_e \tag{1.3}$$

where E_e is the energy of the incident electron and ε is the energy of outcoming photon [3]. The strong dependence of ε on the electron Lorentz factor γ ($\sim 10^2$ - 10^3) can give a possible increase of 10^4 - 10^6 times the photon energy.

One basic scheme to explain HE and VHE γ-rays from astrophysical sources is the combined action of SR and IC, which is the basis of the Synchrotron Self Compton (SSC) model. In the simplest "one-component" SSC model, ultra-relativistic electrons, accelerated in magnetic fields, emit SR in the form of a spectrum peaked in the infrared/X-ray range and then such photons interact with their own parent electron population via IC.

Typical multi-wavelength SSC spectra reproduce the photon *Spectral Energy Distribution* (SED) of the highest energy sources observed with its two peak component (SR and IC). This behaviour has been verified with high accurancy by observations of the Crab Nebula (fig.1.5), a steady VHE gamma emitter in the Milky Way often used to calibrate VHE gamma instrument as well as by jets of many AGNs.

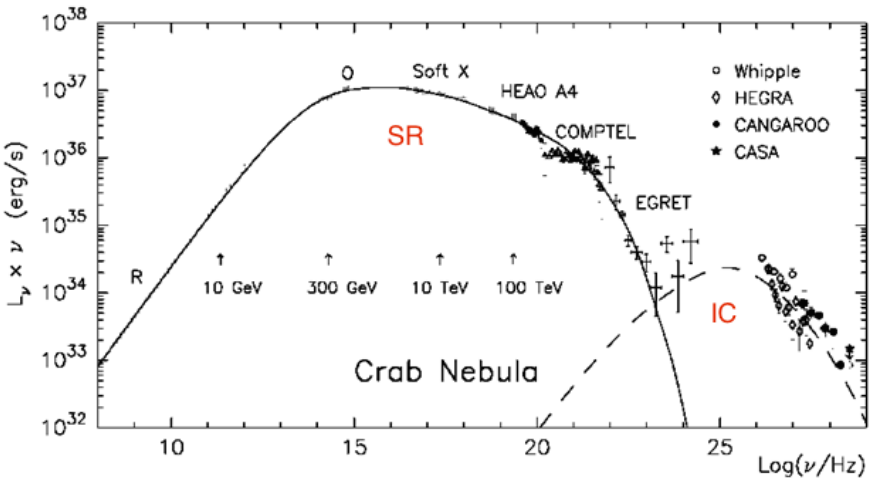

Figure 1.5: Spectral Energy Distribution of the Crab Nebula. It shows the two component, SR at the lowest band and IC at the higest one [4].

1.2.2 Hadronic Models

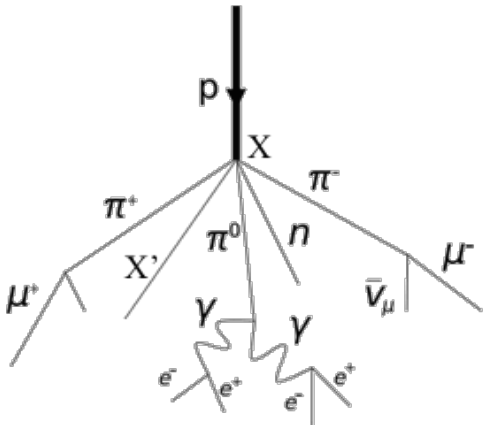

Figure 1.6: Interaction of relativistic protons with interstellar medium matter.

The interaction of relativistic protons with interstellar medium matter (fig 1.6) or radiation (γ_i) produces hadronic cascade, made mainly of pions as π^0 and $\pi^{\pm}$. On the average one pion out of three is neutral and subject to decay electromagnetically in photons with a short life time of $8.6 \cdot 10^{-17}$s.

$$p + X \rightarrow \pi^0 + X' \tag{1.4}$$

$$p + \gamma_i \rightarrow \Delta^+ \rightarrow p + \pi^0 \tag{1.5}$$

$$\pi^0 \rightarrow \gamma\gamma \tag{1.6}$$

where X and X' represents others secondary particles.

The decay of a rest pion produce two γ-rays with an energy distribution peaking at a broad maximum of $E_\gamma = \frac{m_{\pi^0}c^2}{2} \simeq 67.5$ MeV (half of the π^0 mass), while the photons generated from a π^0 decaying with velocity $v = c\beta$ will have energy (in the lab frame):

$$\varepsilon = \frac{1}{2}\gamma m_{\pi^0}c^2(1 + \beta\cos\theta) = \frac{1}{2}m_{\pi^0}c^2\frac{1 + \beta\cos\theta}{\sqrt{1-\beta^2}} \tag{1.7}$$

with γ the π^0 Lorentz factor and θ the angle of the emitted photon with respect to the π^0 direction [3]. The γ-rays emitted can reach the VHE and in principle their energy spectrum is distinguishable from those of electromagnetic origin.

1.3 Astrophysical Sources of VHE Gamma Rays

In the last decade the use of Cherenkov Telescope produce an impressive discovery of VHE γ-ray sources. They can be divided in different category, but a first important distinction is between galactic and extragalactic source.

1.3.1 Galactic Sources

Due to their vicinity, the galactic source of γ-rays are of basic interest in γ-ray astronomy. They are often observed as unique opportunity to carry out studies on the morphology of the emission region, moreover, the photons do not suffer absorption of cosmological background light.

SNR are the left over a SN explosion of a massive star when it run out the fuel of fusion process and the gravitational pressure is not more opposed by the nuclear reactions. SN can be classified as SN I and SN II types depending on the amount of energy released in the explosion: SN I can reach 10^{44} J, while SN II can emit up to 10^{46} J and sometimes leave a neutron star.

SNRs is interpreted as a superposition of SR emission, from radio to soft-γ wavelengths, and a IC part ranging from soft to VHE γ energy. The SR emission is due to the interaction of relativistic electrons with magnetic fields, while the IC peak come from the scattering of relativistic electrons with target radiation fields, such as synchrotron or CMB radiation.

SNRs can be divided essentially in two category shell-type SNRs and Pulsar Wind Nebulae (PWN). In the first case there is no relic of the SN inside the nebula, while if a fast rotating magnetized neutron star (pulsar) remain in the center of the nebulae it is a PWN. Pulsars are produced in SN II explosions

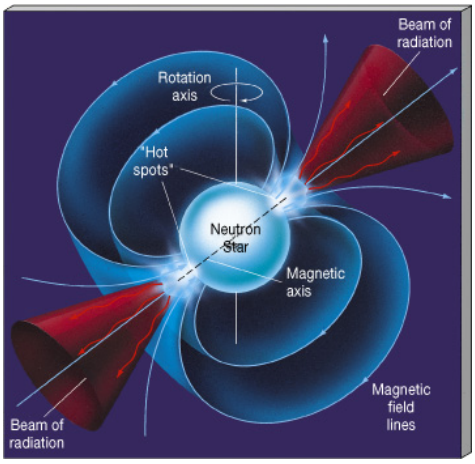

(a)

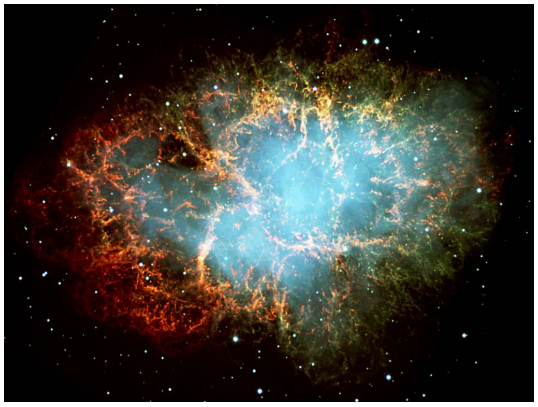

(b)

Figure 1.7: Artistic view of a PWN (*a*) and an image of the Crab Nebula (*b*).

their masses is between 1.4 $M_\odot$ and 3 $M_\odot$ with a diameter of about 10 km, they are the densest known object in the Universe after Black Holes.

The PWN are the most VHE γ-ray sources within the Milky Way and the best known and observed example of such systems is the Crab Nebula (fig. 1.7b). Located at a distance of 2 kpc and born in 1054 A.D., by a SN II explosion, the Crab Nebula is the most important source used as standard "calibration candle" for ground-based and satellite borne γ-rays experiment. The reason of this application is its radiation emission in almost all wavelengths of the electromagnetic spectrum from 10^{-5} eV (radio) to nearly 10^{14} eV (γ-rays).

Another interesting galactic γ-ray sources are binary systems, i.e. system where there is a mass transferred to a very massive object (neutron star, BH) from a partner star (usually a blue giant or white dwarf) orbiting around them. The involved object in the binary systems define their characteristics i.e. the *microquasar* (μQ) is a binary system with a BH as massive object which produce relativistic jets. The relativistic charged particles interacting with the magnetic fields produce SR (from radio to X-rays) and the UV photons

emitted scatter with the jet relativistic electrons through the IC mechanism. The γ-rays peak emitted by μQ can reach the GeV-TeV energies.

1.3.2 Extragalactic Sources

As already mentioned the Universe is not completely transparent to γ-rays, due to their interaction with the photons of the EBL. For this reason, it is believed that we cannot observe γ-rays in the VHE range from objects at high redshifts (let say greater than z $\simeq$ 1 for energies above 100 GeV).

The most common extragalactic sources of γ-rays and are the *Active Galactic Nuclei* (AGN), which are galaxies with an active core, brighter and more energetic that the one of usual galaxies. The core mass for AGNs ranges between $10^6 M_\odot$ and $10^9 M_\odot$, concentrated in a region of the solar system size. This object must be a Super-Massive Black holes (SMBH). For their extreme physics condition AGNs are special laboratories.

The AGNs are believed to be the most powerful sources of non-thermal energies in the Universe and they have been classified into different categories: Seyfert galaxies, radio galaxies, quasars, blazars and others, depending on the observed features. Moreover, they show very variable fluxes, spanning from radio to TeV range and an emission which can grow by orders of magnitude when the quasar is *flaring*.

A unified theory reduces the differences in the observed phenomena to the orientation of the source relative to our line of sight. In this unified scheme the SMBH is surrounding by a rotating plasma accretion disk, which is heated up and emits from optical to X-ray wavelengths with a thermal spectrum peaked in X-ray band. A thick dust obscuring torus, situated farther outside, absorbs the emission from the accretion disc and turn its in IR radiation. Two narrow jets emerge from the SMBH perpendicularly to the disc plane and extend for several kiloparsecs (fig. 1.8a). The typical emission from a jet is non-thermal and fits the SSC model (fig. 1.8b).

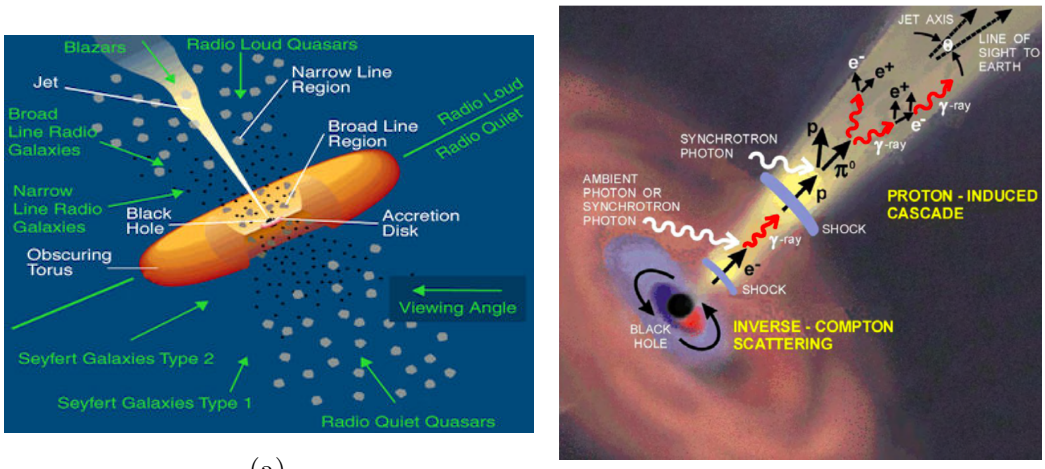

(a) (b)

Figure 1.8: Schematic view of the standard AGN unified model (*a*) and a particular of an AGN jet, with a sketch of SSC emission (*b*).

When the jet is mostly aligned with the direction of observation, the peculiar object view by the observer is know as a blazar. Due to the polar view of the jets, the bulk relativistic motion of the emitting plasma causes radiation to be beamed in a forward direction, making the variability appear more rapid and the luminosity higher than in the rest frame for the Lorentz dilation. For this reason the blazars are consider the most "active" kind of AGNs.

The other kind of extragalactic γ-rays sources are the *Gamma-Ray Burst* (GRB), the most energetic and violent short-term events occurring in the Universe. The GRBs are flashes of gamma rays emanating from random places at random times, with a frequency of about 1-2 per day and an average duration of a few seconds (from few milliseconds to several minutes). This prompt emission is followed by an afterglow of less energetic photons in all further domains of electromagnetic radiation, which can last from days to years.

The most observed GRBs appear to be collimated emissions caused by the collapse of the core of a rapidly rotating, high-mass star into a black hole, while a subclass of GRBs (the "short" bursts) appear to originate from a

different process, most probably the merging of a neutron stars in a binary system.

1.4 The Propagation of Gamma Rays

During the travel from the cosmic source towards the observer the γ-rays can be absorbed by interstellar (or intergalactic) particles or by *Extragalactic Background Light* (EBL). In the first case the process involved is:

$$\gamma + (\gamma) \rightarrow e^- + e^+ \tag{1.8}$$

where (γ) is a virtual photon of the particle field, while the EBL absorption process is:

$$\gamma + \gamma_{EBL} \rightarrow e^- + e^+ \tag{1.9}$$

where γ_{EBL} is a photon from EBL. A straightforward calculation shows that the absorption of VHE γ-ray by matter is negligible, while the EBL low-energy photons are responsible for the opacity of the Universe to γ-rays, which increases with the γ-rays energy.

The EBL is the second largest background after the *Cosmic Microwave Background* (CMB) and the Universe is almost isotropically filled with EBL soft photons, excluding the galactic plane. While the CMB originated by the decoupling of matter and radiation following the Big Bang and the structure of the Universe in that moment, the EBL consists of the sum of starlight emitted by galaxies throughout their whole cosmic history, plus additional contributions, like radiations from the first stars formed before galaxies were assembled or dust scattered light. Therefore, the EBL contains important information both the evolution of baryonic components of galaxies and the structure of the Universe in the pre-galactic era.

The energy density spectrum of EBL has been measured by different experiments and it is characterized by two pronounced peaks. The first peak at ~ 1 μm, know as the stellar component, is associated by light emitted by stars and it is redshifted the history of the Universe. The second at ~ 100 μm comes from the re-processing of the starlight by dust and for this reason is called the dust component.

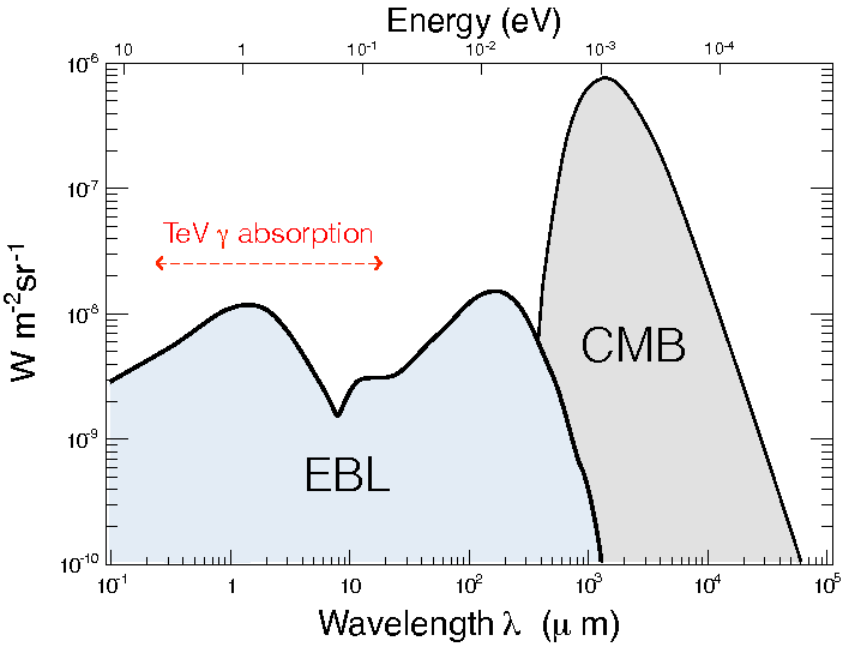

Figure 1.9: Schematic Spectral Energy Distributions.

The γ-rays absorption by EBL occurs when the center-of-mass energy of the photon-photon system exceeds twice the squared rest energy of the electron. The corresponding cross-section is described by Bethe-Heitler formula derived in a QED framework:

$$\sigma(E_\gamma, \varepsilon) \simeq 1.25 \cdot 10^{-25}(1-\beta^2) \cdot \left[2\beta(\beta^2-2) + (3-\beta^4)\ln\left(\frac{1+\beta}{1-\beta}\right)\right] \mathrm{cm}^2 \quad (1.10)$$

$\beta = \sqrt{1-(m_e c^2)^2/(E_\gamma \cdot \varepsilon)}$, m_e is the rest mass of electron, E_γ the energy of the (hard) incident photon and ε that of the (soft) background photon. The cross-section in 1.10 is maximized when ε(eV) $\simeq$ 500 GeV/E, then for example if $E = 1$ TeV the max absorption is for photon with energy $\varepsilon =$ 0.5 eV, corresponding to a near-infrared EBL photon. Therefore, VHE γ-rays interact mainly with optical or infrared photons, while the CMB photons become dominant at $E_\gamma \sim 1$ PeV.

The high cross-section of the interaction of γ-rays with EBL cause the opacity of Universe, at least beyond 100 GeV, therefore a γ-ray source can not be observed if its distance is beyond the *Gamma Ray Horizon* (also named *attenuation edge*). For this reason the γ-ray flux (F_{obs}), for a given energy E_γ and redshift z, can be written as an exponential cutoff:

$$F_{obs}(E_\gamma, z) = F_{int}(E_\gamma) \cdot e^{-\tau(E_\gamma, z)} \tag{1.11}$$

where F_{int} is the intrinsic flux of the source and $\tau(E_\gamma, z)$ is the *optical depth* as a function of γ-ray energy and the redshift z [5]. The *Gamma Ray Horizon* for a photon of energy E_γ is then defined as the distance corresponding to the redshift z for which $\tau(E_\gamma, z) = 1$, i.e. the path length which attenuates the photon flux by a factor $1/e$.

Due to the energy dependence of τ, the determination of emitted γ-ray SED can be difficult, even for small difference of optical depth. However, if the opacity of the Universe to γ-rays is known, in principle it is possible derive the original emission spectra of TeV sources and test the emission models.

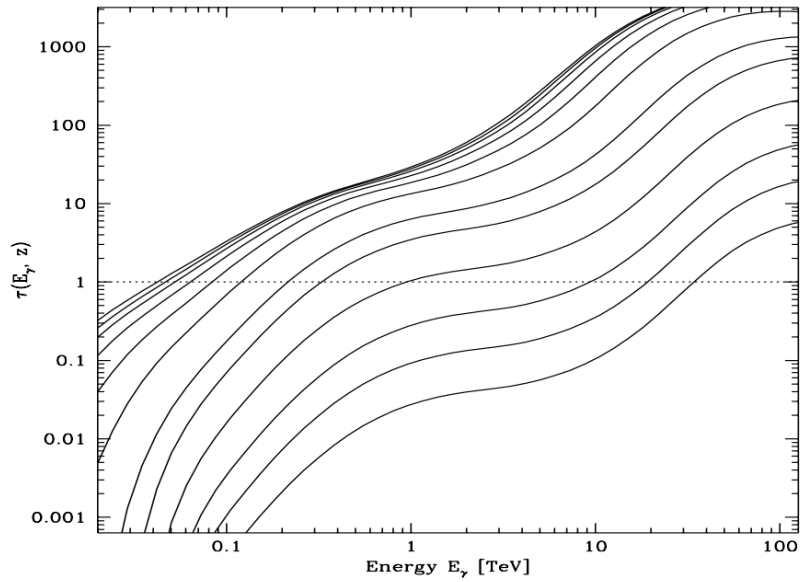

Figure 1.10: The optical depth by photon-photon collision as a function of the photon energy for sources located at z = 0.003, 0.01, 0.03, 0.1, 0.3, 0.5, 1, 1.5, 2, 2.5, 3, 4 from bottom to top [6].

2

The New Cherenkov Telescope Array Observatory

2.1 The Cherenkov Technique

As mentioned in 1.1, the γ-rays are "messengers" from outer space and high energy Universe. Unfortunately VHE γ astrophysics was developed only in the last decade, because the detection of VHE radiation is a complex experimental problem. The photons can be detected directly from the ground only in small energy bands in the optical and radio range. Moreover, the flux of VHE γ-rays is very low ($\propto E^{-2.5}$ or lower), in practice VHE radiation can only be observed by detectors with big effective area and high sensitivity.

The Cherenkov Telescope Array (CTA) will be a large array of Cherenkov telescopes of different sizes, based on the proven technology of Imaging Air Cherenkov Telescope (IACT) and deployed on an unprecedented scale. This technology uses the Imaging Air Cherenkov Telescope technique (IACTt) to detect VHE γ-rays, which is based on the detection of Cherenkov photons generated in Earth atmosphere by electromagnetic showers originated by VHE radiation.

An important index of an observatory performances is expressed by the

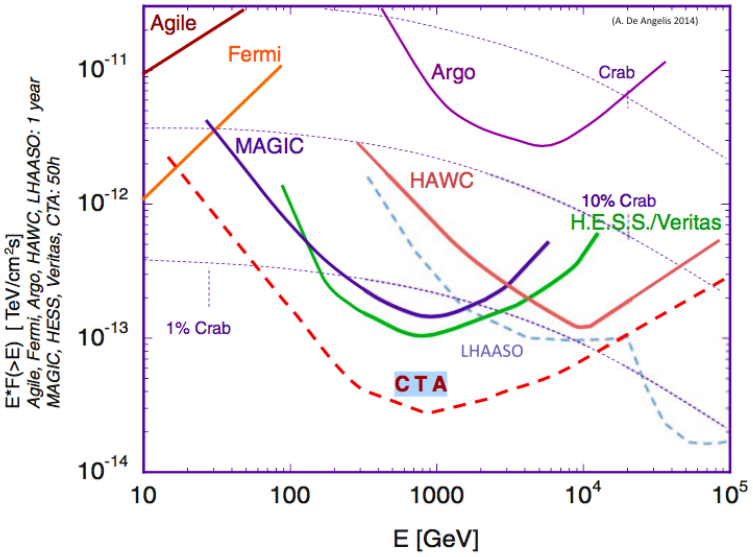

Figure 2.1: Foreseen CTA sensitivity in the energy interval 0.01-100 TeV compared with that of the present Cherenkov Arrays [12].

sensitivity, defined as the minimum γ-rays flux, which returns 5σ significance in 50 h of observation. Figure 2.1 shows the Cherenkov Telescope Array (CTA) sensitivity compared with the current VHE γ detectors.

The aim of this chapter is to explain how the VHE γ-rays can be indirectly detected by CTA and to describe the design of the future CTA telescopes.

2.1.1 Extended Air Showers (EAS)

The Extended Air Shower (EAS) originates in the high atmosphere by the interaction between atmospheric nuclei (mainly oxygen and nitrogen) and a high energy cosmic ray (hadrons, charged light leptons and VHE photons), also called primary cosmic ray (CR). The loss of energy of CR, in the interaction, generates secondary particles and photons, which give rise to an avalanche of photons and particles with velocity nearly at the vacuum speed of light. Since the CR has relativistic energies, the shower is strongly collimated along

the incoming direction of CR. The physical process, involved in creation of the shower, depends on the nature and on the energy of the CR. For this reason the showers can be divided in two groups, hadronic showers and electromagnetic (EM) showers. In the first case a proton or a nucleus generates the shower, while, in the second case, the shower is generated by VHE cosmic electrons, positrons or γ-rays.

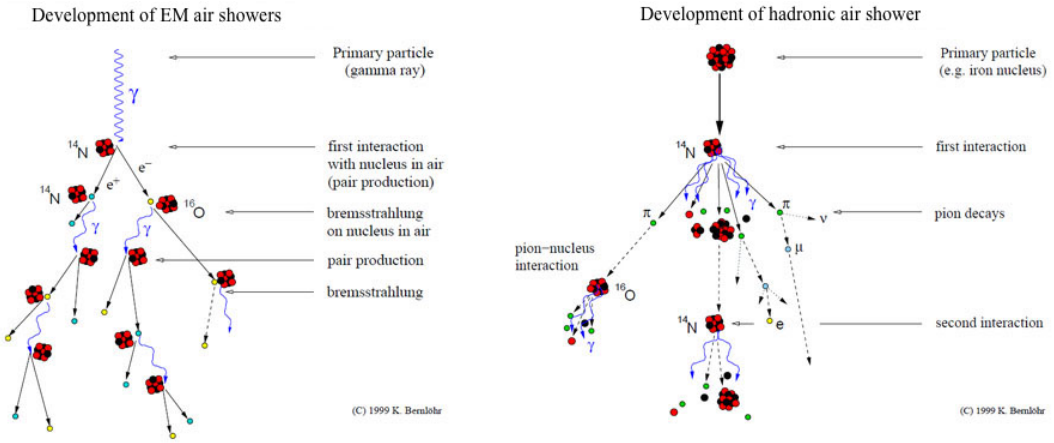

Figure 2.2: EM and hadronic shower.

Electromagnetic Shower

In the development of EM showers generated, for example, by a primary VHE γ-rays, the two main processes involved are:

1. Pair-production,

2. Bremsstrahlung effect.

In a pair-production a high energy photon interacts with an atmospheric nucleus and the photon is converted in a e^-e^+ pair. The electron and positron are accelerated by charged nuclei of atmosphere and can emit high energy radiations by the Bremsstrahlung effect. At the *Standard Temperature Pressure*

(STP) conditions the free mean path of a photon before pair creation (interaction length) is $X_0^\gamma = 47\text{g/cm}^2$, which is very similar to the radiation length of Bremsstrahlung effect $X_0^e \simeq \frac{7}{9} X_0^\gamma \simeq 36.66\text{g/cm}^2$.

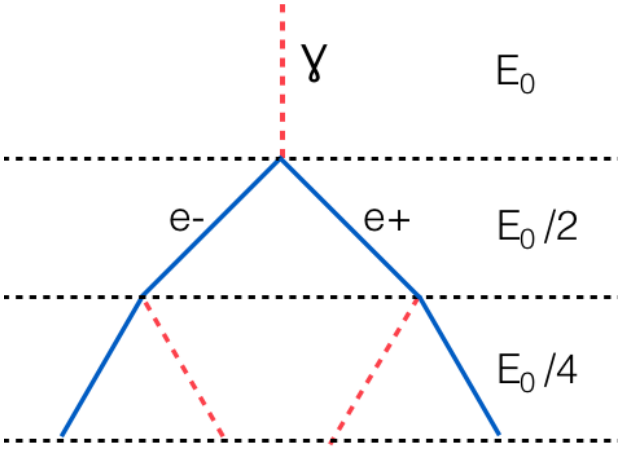

Figure 2.3: Heitler model. Each level corresponds to one radiation length X_0.

Figure 2.3 shows the interaction of a VHE γ-ray with the atmosphere in the Heitler model, which is a simple model to describe the characteristics of the EM shower's development in good approximation.

Considering only pair-production and bremsstrahlung effect in the development of the EM cascade, energy equally divided between the produced particles in each process and the radiation length equal to the interaction length ($X_0^\gamma \simeq X_0^e \simeq X_0$), then, after n radiation length X_0, there will be $N(n) = 2^n$ particles equally distributed between electrons, positrons and photons, each of them with the mean energy $E(n) = E_0/2^n$ (E_0 is the energy of CR). The shower stops producing new particles or photons at the critical energy $E_c \sim 83$ MeV, when the ionization becomes the dominant process in the energy loss. The electrons rapidly cool off through the thermalisation and the shower quickly dies out. The maximal development of the shower is at n_{max} radiation length, with the length of the shower L_{sh} and N_{max} particles.

All of these parameters are dependent on E_0 and the relationships can be expressed by the formulas:

$$E_c = \frac{E_0}{2^{n_{max}}} \rightarrow n_{max} = \frac{\log(\frac{E_0}{E_c})}{\log(2)} \tag{2.1}$$

$$L_{sh} = n_{max} X_0 \simeq \frac{\log(\frac{E_0}{E_c})}{\log(2)} X_0 \tag{2.2}$$

$$N_{max} = 2^{n_{max}} = \frac{E_0}{E_c} \tag{2.3}$$

The width of the shower is, instead, independent of E_0 and it is described by Molière radius r_M:

$$r_M = E_M \frac{X_0}{E_c} = (21\text{MeV}) \frac{X_0}{E_c}. \tag{2.4}$$

With complex model and some approximations, it is possible to obtain analytical solutions of the shower equations. Considering the Compton effect and the photo-production mechanism negligible (Rossi B approximation), Greisen calculated the mean number of electrons $< N_e >$ above the critical energy E_c:

$$< N_e(t, E_0) >= \frac{0.31}{\sqrt{\ln(E_0/E_c)}} e^{t(1-1.5\ln(s))} \tag{2.5}$$

with:

$$t = X/X_0 \approx \frac{X_{air}}{X_0 \cdot \cos(\theta_{sh})} e^{-\frac{H}{H_0}} \tag{2.6}$$

$$s = \frac{3t}{t + 2\ln(E_0/E_c)} \tag{2.7}$$

$$\Delta N_e(s) \simeq \frac{9}{14}(s - 1 - 3\ln(s)) \cdot N_e(s) \tag{2.8}$$

with E_0 the energy of CR, $X_{air} = 1013$ g/cm^2 the column height of air at ground level, H the height above the sea level, $H_0 \simeq 8$ km the scale height of the atmospheric pressure and θ_{sh} the incident angle of the shower. The

slant depth t determines the thickness of the atmosphere in units of X_0. In formula 2.8, the parameter s is called "shower age" and describes the level of development of the shower. It can be expressed by the formula:

$$s = \frac{3t}{t + 2t_{max}} \tag{2.9}$$

where t_{max} is equal to $\ln(E_0/E_c)$. The shower age assumes well-defined values in specific moments of the development of the shower, it is 0 at the first interaction, 1 at the shower maximum development and 3 at the death of the shower. Excluding fluctuations of the height of the first interaction in atmosphere, the shower fluctuations can be expressed as $\Delta N_e(s)$. They can be rather large from shower to shower and thus have important consequences e.g. for the energy estimation of CR.

Hadronic Shower

As mentioned previously, a Hadronic Shower is generated by a proton or a nucleus, and the strong interaction with the nuclei in the atmosphere produces pions ($\sim$ 90%), kaons ($\sim$ 10%) and light baryons (p, $\bar{p}$, n, $\bar{n}$). UHE hadronic CR can also generates heavier charmed mesons and baryons. The particles generated, in the first interactions of the CR with atmosphere, form the hadronic core of the cascade. In the first stage of the shower, the energy per nucleon is above the pion production threshold ($\sim$ 1GeV), the strong interaction of core with the nuclei of atmosphere is dominant and the hadronic particles are generated. In the final stage of the shower, when the mean energy per nucleon is lower than 1 GeV, the dominant processes are ionization and decays and the shower starts to die out.

The hadronic core can be divided into three component:

• The hadronic component, which is formed by high energy nucleons and mesons. In the final stage of this component charged pions and kaons decay into muons and neutrinos through the channel:

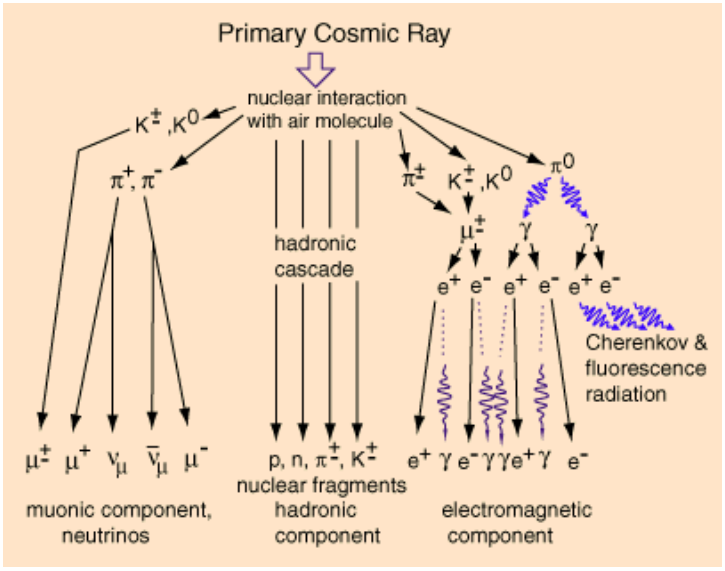

Figure 2.4: Hadronic shower.

$$\pi^{\pm} \rightarrow \mu^{\pm} + \nu_{\mu}(\bar{\nu_{\mu}}) \tag{2.10}$$

$$K^{\pm} \rightarrow \pi^{\pm} + \pi^{0} \tag{2.11}$$

$$K^{\pm} \rightarrow \mu^{\pm} + \nu_{\mu}(\bar{\nu_{\mu}}) \tag{2.12}$$

$$K^{0}_{L} \rightarrow \pi^{\pm} + \mu^{\mp} + \nu_{\mu}(\bar{\nu_{\mu}}) \tag{2.13}$$

• The muonic component, which is fed by the decays of hadronic component (2.10, 2.12 and 2.13). Muons mainly lose energy with ionization, even if they can decay into electron and positron through the reactions:

$$\mu^{+} \rightarrow e^{+} + \nu_{e} + \bar{\nu_{\mu}} \tag{2.14}$$

$$\mu^{-} \rightarrow e^{-} + \bar{\nu_{e}} + \nu_{\mu} \tag{2.15}$$

However, only a small fraction of muons decay before reaching the ground, due to their lifetime ($2.2 \cdot 10^{-6}$ s)

• The electromagnetic component, which is generated by the decay of neutral pions:

$$\pi^0 \rightarrow \gamma + \gamma \tag{2.16}$$

In hadronic showers about one third of the pions is neutral and, therefore, about one third of the energy in hadronic interaction is transfered to electromagnetic component. The photons have very high energies and can generate an electromagnetic cascade, interacting with atmosphere nuclei, which can be confused as a "genuine" EM shower.

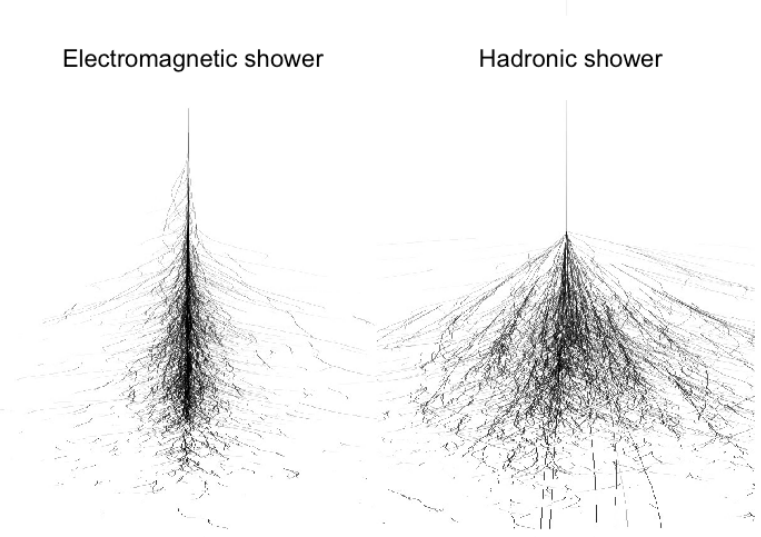

Figure 2.5: The different lateral extension of EM and hadronic showers.

The most peculiar characteristic, to discern EM shower from hadronic shower, is their lateral extension (fig. 2.5). Due to the large transverse momentum in hadronic interaction the EM shower is narrow and more concentrated along the direction of the primary than hadron shower, which is irregular

and contain several EM sub-shower with divergent direction. The distinction is evident above 100 GeV, where is one of the most important factor to discriminate between EM shower and hadron shower.

2.1.2 Cherenkov Light and the Imaging Air Cherenkov Telescopes

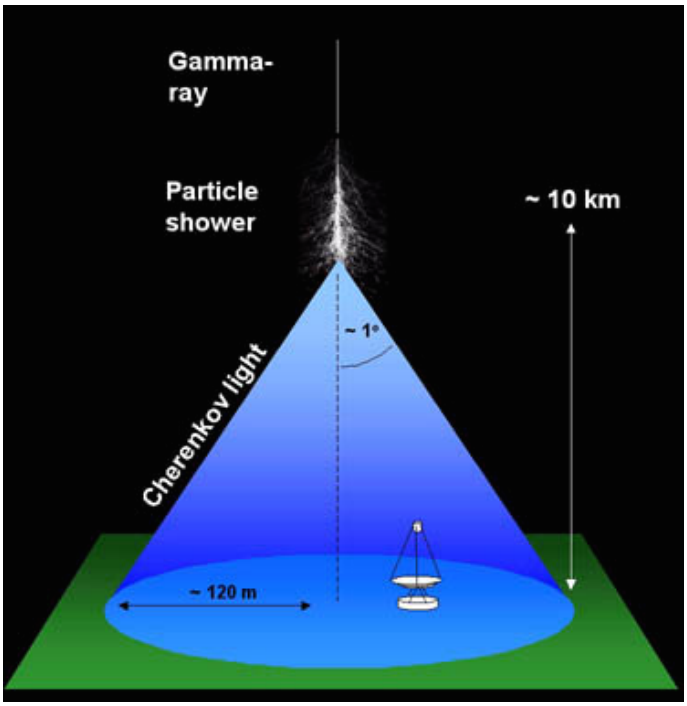

Figure 2.6: VHE γ-rays observation with Cherekov telescopes.

The Imaging Atmospheric Cherenkov Telescopes (IACTs) do not detect the primary γ-ray, because the VHE radiations do not reach the earth at the ground, but they observe the Cherenkov photons generated by charged particles in atmospheric cascade. The air shower indeed contains a large number of relativistic charged particle, which surpass the local speed of light in the air and, therefore, they emit Cherenkov radiation. When these photons reach an IACT, they are collected by a large mirror and focused into a camera made

by an array of photodetectors (mainly photomultiplier tubes (PMTs)), which converts the light into electronic signal. Finally the data acquisition system and the data analysis study the camera signals to reconstruct the shower development.

Cherenkov effect

A charged particle, which moves through a transparent dielectric (like air) with a velocity faster than the speed of light in the medium, can radiate Cherenkov light. When the charged particles pass close to the air atoms, they can temporally polarize it in distinct modes tied to their speed (fig.2.7). In the case of relativistic charged particles, the following reorientation of the electric dipoles induces light emission.

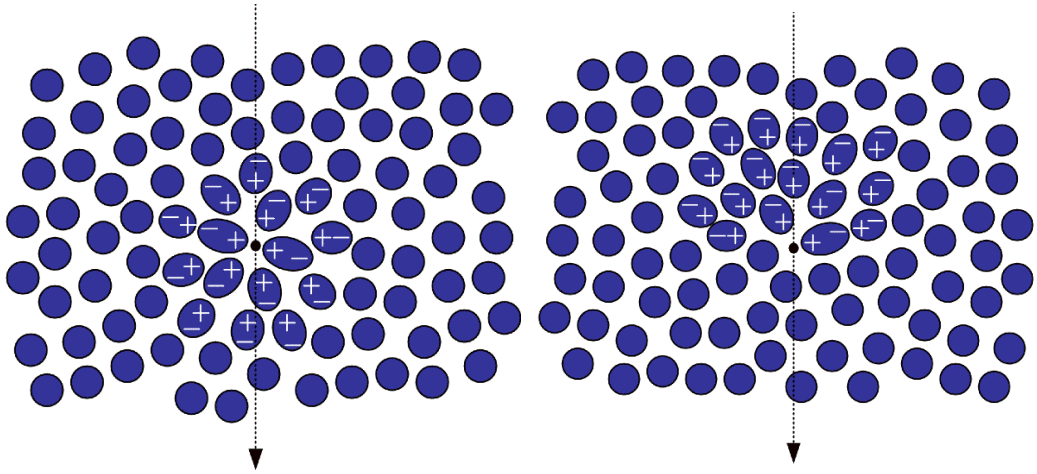

(a) (b)

Figure 2.7: Representation of the polarization induced by a charged particle. (a) Symmetric polarization generated by a slow moving charged particle. (b) Asymmetric polarization inducted by a relativistic charged particle.

The emitted radiation is in the form of shock waves (fig. 2.8a), therefore, the emission angle of the radiation (called Cherenkov angle) can be deduced

by simple geometrical arguments using *Huygens*'s principle (fig. 2.8b) into the equation:

$$\cos(\theta) = \frac{\Delta t \cdot c/n}{\Delta t \cdot \beta c} = \frac{1}{\beta n} \tag{2.17}$$

with n the refraction index of the dielectric, βc the particle velocity and c the speed of light in vacuum. Formula 2.17 shows the dependence of Cherenkov angle on particle velocity βc. The maximum value of Cherenkov angle is obtained with $\beta = 1$ and its value is $\theta_{max} = \arccos(1/n)$.

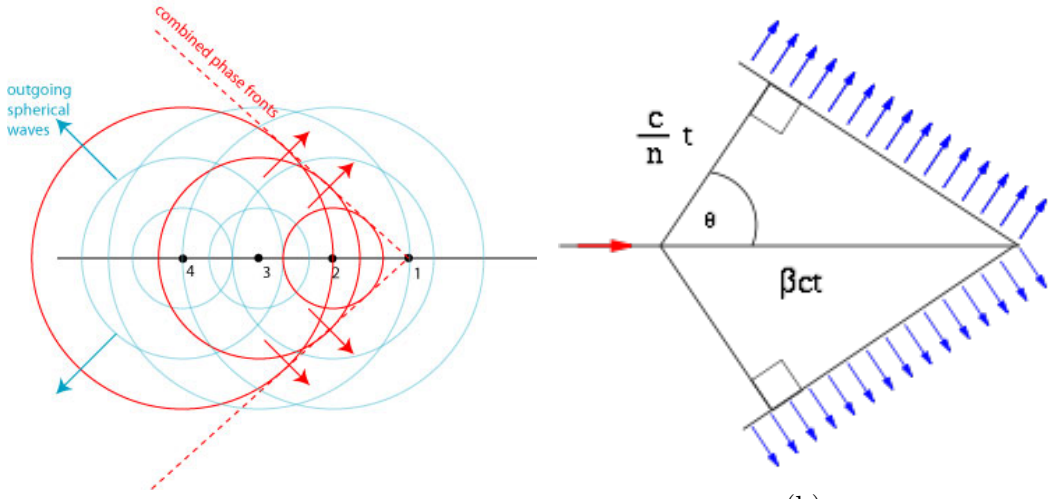

(a) (b)

Figure 2.8: Emission angle of Cherenkov radiation.

Since the minimum particle speed to produce Cherenkov light is $\beta_{min} c = c/n$, the energy threshold of Cherenkov effect for a charged particle of rest mass m_0 is the kinetic energy:

$$E_{th} = \gamma m_0 c^2 = \frac{m_0 c^2}{\sqrt{1 - \beta_{min}^2}} = \frac{m_0 c^2}{\sqrt{1 - 1/n^2}} \tag{2.18}$$

with $\beta_{min} = 1/n$ and γ the Lorentz factor.

In the case of relativistic charged particle from an atmospheric shower it is necessary to take into account the exponential variation of air pressure as

a function of the height h and its effects on atmospheric refractive index. In the isothermal atmosphere approximation the atmospheric density is:

$$\rho(h) = \rho_0 \cdot e^{\frac{-h}{h_0}} \tag{2.19}$$

with $h_0 = 7.1$ km the shale height factor and $\rho_0 = 1.22 \cdot 10^{-3}$ g/cm^3 the atmospheric density at sea level. In first approximation the refractive index is:

$$n(h) = 1 + n_h = 1 + n_0 \cdot e^{\frac{-h}{h_0}} \tag{2.20}$$

with $n_0 = 2.9 \cdot 10^{-4}$. Since $n_h \ll 1$ and neglecting the dependence of the refractive index on the wavelength λ, the energy threshold as a function of height h is:

$$E_{th} = \frac{m_0 c^2}{\sqrt{1 - 1/n^2}} \simeq \frac{m_0 c^2}{\sqrt{2n_0 \cdot e^{\frac{-h}{h_0}}}} \tag{2.21}$$

while the maximum Cherenkov angle θ_{max} at the different height h can be obtained by:

$$\cos(\theta_{max}) = \frac{1}{1 + n_0 \cdot e^{\frac{-h}{h_0}}} \simeq 1 - n_0 \cdot e^{\frac{-h}{h_0}}. \tag{2.22}$$

This formula shows that at higher altitude (greater h) the maximum Cherenkov angle is smaller (fig. 2.9).

The shower can be divided in three component: the head, which corresponds to the zone of CR's first interactions, the tail, which is the last part of the shower and the core which is the shower between the head and the tail. Assuming the velocity of the charged particle $\beta \simeq 1$, one can determinate the altitude of Cherenkov emission, *i.e.* the origin of the photon (head, core or tail), with the formula:

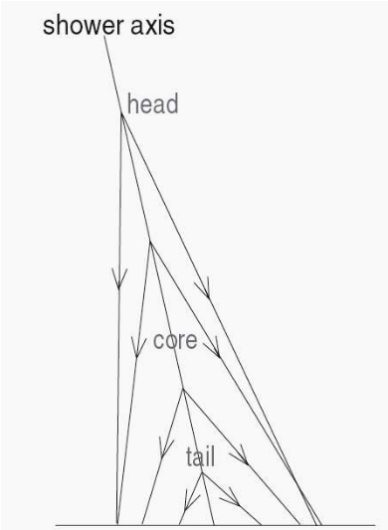

Figure 2.9: Cherenkov angle at different heights.

$$h = \frac{R_c}{\tan(\theta)} \sin^2(\psi) + h_{obs} \tag{2.23}$$

where h is the height of the Cherenkov emission, θ is the Cherenkov angle, ψ is the angle of shower axis with ground and R_c is the distance between the impact point of the photon and the shower axis.

The number of photons emitted per unit path length (x), per unit wavelength (λ) by a particle of charge ze is:

$$\frac{d^2N}{dxd\lambda} = \frac{2\pi\alpha z^2}{\lambda^2}\Big(1 - \frac{1}{\beta^2 n^2(\lambda)}\Big) \tag{2.24}$$

where α is the fine structure constant. Therefore, the Cherenkov spectrum can be obtained by forumla (2.24), ignoring the index of refraction dependency on λ and integrating between two wavelengths:

$$\frac{dN}{dx} = \int_{\lambda_1}^{\lambda_2} \frac{d^2N}{dxd\lambda} d\lambda = 2\pi\alpha z^2 \Big(\frac{1}{\lambda_2} - \frac{1}{\lambda_1}\Big) \sin^2(\theta) \tag{2.25}$$

where θ is the Cherenkov angle.

In an EM shower, a primary γ-ray generates about 500 photons of Cherenkov radiation, per GeV of energy, with wavelengths between 300 nm and 600 nm. Most of these photons are in the UV range, due to the strong λ^2 dependency of formula (2.24). The original light spectrum is not observed by CT due to two principal factors:

1. Scattering,

2. Absorption.

In atmosphere, the scattering angles of photons are larger than the Cherenkov angle and scattered photons are usually lost for a CT. In good atmospheric condition, the dominant scattering process of light transmission losses is the Rayleigh scattering, which is caused by air molecules with diameter of the order of few nm. The cross-section of this process is proportional to λ^{-4}, therefore affects the UV/blue range of the spectrum. Another important scattering losses process is the Mie scattering, which is due to aerosol particles larger than photon wavelength. This scattering process is dominant in poor atmospheric conditions and its cross-section is proportional to $\lambda^{-(1\div1.5)}$.

The absorption processes act on light with wavelength lower than 280 nm ($\lambda < 280$ nm) or greater than 800 nm ($\lambda > 800$ nm). In the first case, ozone (O_3), oxygen (O_2) and nitrogen (N_2) absorb the electromagnetic radiation (UV absorption), while, for $\lambda > 800$ nm, the light is absorbed by water (H_2O) and carbon dioxide (CO_2) molecules. Figure (2.10) shows the comparison between the emitted Cherenkov spectra at 10 km and the one at 2 km above the sea level, the UV range is the most affected. The spectrum of light detected (solid curve) peaks around 330 nm, rather close to the ultraviolet and blue region. Consequently, the photodetectors of CT must be maximised in the interval between 300 and 450 nm.

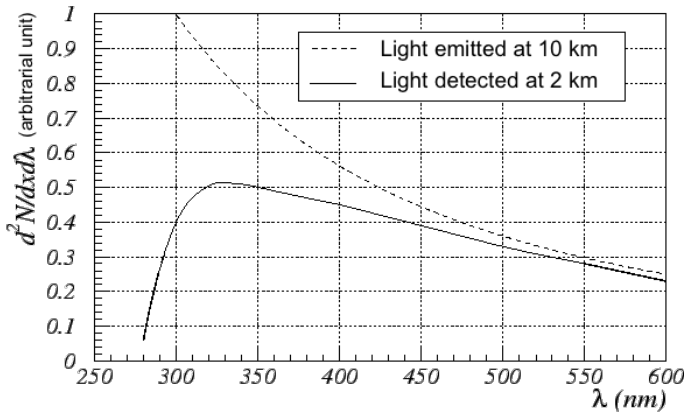

Figure 2.10: Spectral of Cherenkov light by vertical γ-ray shower at 10 km height (dashed line) and the corresponding spectra at 2 km above the sea level (solid curve), affected by absorption, Rayleigh and Mie scattering.

IACT technique

As mentioned previously, an IACT is not directly exposed to primary γ-rays, but it collects and detects a fraction of the Cherenkov light, produced by EM shower, with a reflecting surface and a central camera (usually an array of PMT). The reflector focuses the light on the camera, while the photosensors of detector convert the photons into electrical pulses and then the electronic read-out system form an image of the EAS from the electrical signal. Setting a polar coordinate system in the focal plane of a parabolic reflector and under parallax approximation, the focused position (ρ, ϕ) can be obtained from the incoming direction of each photon (ψ, Φ) with the formula:

$$\rho \simeq \sin(\psi) \cdot f \simeq \psi \cdot f \tag{2.26}$$

$$\phi = \Phi \tag{2.27}$$

with f the reflecting surface focal length, ψ the photon incident angle respect to the telescope axis and ρ the distance in the focal plane from the focal point

to the reflected photon. Photons emitted by the shower at higher altitude have smaller Cherenkov angle, therefore, they are focused closer to the camera center than the photons emitted at lower altitude. Figure (2.11) shows the image formed in the camera which has approximately an elliptical shape. This kind of focusing allows to reconstruct a three dimensional shower from a bidimensional image, thus the IACT technique can study the main characteristics of EM shower and its primary γ-ray.

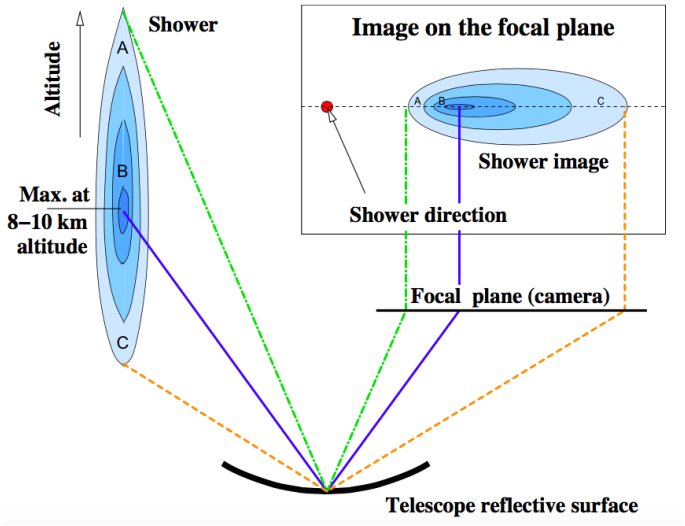

Figure 2.11: Schematic sequence creation of the shower imaging in a CT, where A is the head of the shower, B the core and C the tail.

The morphology of the images can be used to obtain information about the primary VHE γ-rays with a Hillas Analysis applied to the image parameters. The main parameters are derived from the photon distribution of the image, others are related to a defined position in the camera, which is usually related to the expected source position (normally at the camera centre) or to the arrival time of the Cherenkov signal. The main parameters of Hillas Analysis are summarize in table (2.1)

Since strong backgrounds can reduce the sensitivity of IACTs, the first use

Image Parameter	Description
Size	The number of photons of the image is correlated to the CR energy.
Width	The ellipse minor axis is correlated with the transversal development of the shower (see fig. 2.12).
Lenght	The ellipse major axis is correlated with the longitudinal development of the shower (see fig. 2.12).
MeanX ($\bar{X}$)	X-coordinate of ellipse center (see fig. 2.12).
MeanY ($\bar{Y}$)	Y-coordinate of ellipse center (see fig. 2.12).
CoG	The Center Of the Gravity is the point in the camera with coordinate ($\bar{X}$, $\bar{Y}$) (see fig. 2.12).
Dist	The distance between the center of ellipse and the nominal position of source observed (see fig. 2.12) is correlated to the impact parameter of the shower.
Alpha (α)	The angle between the major axis of the ellipse and the direction from the image CoG to the nominal position of source observed (see fig. 2.12) is correlated with the nature of CR. It is large for hadronic CR and small for γ CR.
Number of islands	The number of distinct islands in the shower image is correlated to the fragmentation of the air shower and can be used to reject hadronic showers
Time gradient	The time gradient measures the magnitude of the time profile of the event.
Time RMS	The time RMS measures the arrival time spread of the Cherenkov photons in the pixels belonging to the image.

Table 2.1: The main parameters of Hillas analysis.

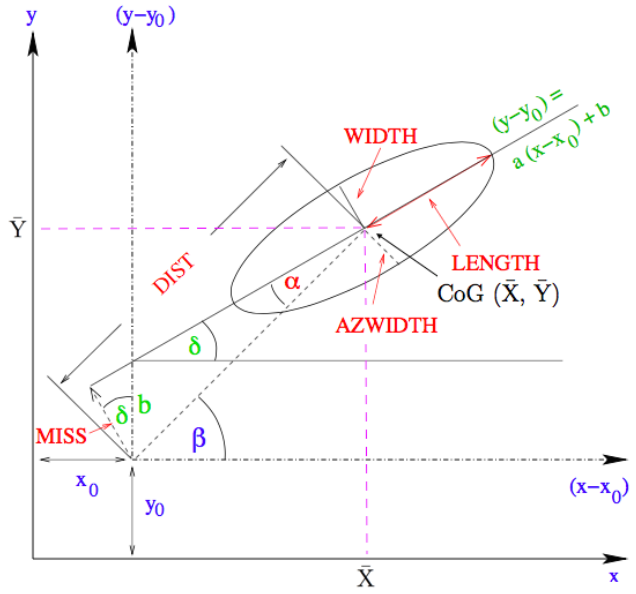

Figure 2.12: Graphic representation of some image parameters described in table (2.1). The nominal position of the observed source is (x_0, y_0).

of Hillas Analysis is to reject the signal from the background sources and only in a second moment to characterize the event. The main source of background for IACT are:

• The light of the night sky (LONS) is the sum of light from bright and faint stars, galactic plane, ionospheric airglow, polar light, moonlight and artificial light. It is a continuous source of background for the Cherenkov light of EM shower from a VHE γ-ray and it is a limiting factor for trigger level of IACT. For this reason the LONS is a main factor of contamination and must be rejected. The method used to reduce the LONS is a next neighbour coincident system of several pixel in a short gate of the order of 5 ns, which decreases the LONS to an acceptable level.

• The showers generated by hadrons are the main background of the IACT's observations, more of 99% of recorded images has hadronic origin. Due to the quite irregular images, compared to those formed by VHE γ-ray's showers,

this sort of background can be highly suppressed by an image analysis. The efficiency of the rejection of hadronic showers background can be larger than 99%.

• The muons with relativistic speed generate Cherenkov light in atmosphere, which is a source of background for IACTs. However, they produce typical ring or arc images, which can be easily recognized and rejected.

• The cosmic electrons and positrons, especially with energy below 100 GeV, are a non-negligible source of background, since their air showers have the same characteristics of ones inducted by VHE γ-ray. For this reason the cosmic light leptons are an irreducible but isotropical source of noise.

The possibility, for Cherenkov photons from an EAS, to trigger an IACT, is strictly correlated to the comparison between the level of their signals and the level of Night Sky Background (LONS or NSB) on the CT camera.

Combining formula (2.3) with (2.25) and limiting λ_1 and λ_2 for the Rayleigh scattering and Mie scattering, the number of Cherekov photons at ground is approximately proportional to the energy E_0 of the primary VHE γ-ray. Therefore, the number of photo-electrons, measured by the detector, can be approximated by the formula:

$$S = \rho_\gamma A\epsilon \propto E_0 A\epsilon \tag{2.28}$$

with ρ_γ the Cherenkov photon density at ground, A the reflecting surface area and ϵ the quantum efficienty of the photo-detector. The noise produced by NSB can be written as:

$$N = \Phi_N \Omega A\epsilon\tau \tag{2.29}$$

where Φ_N is the NSB light flux, Ω the solid angle seen by the single photo-detector and τ the integration time of the front-end electronics. Therefore, the signal-to-noise ratio is:

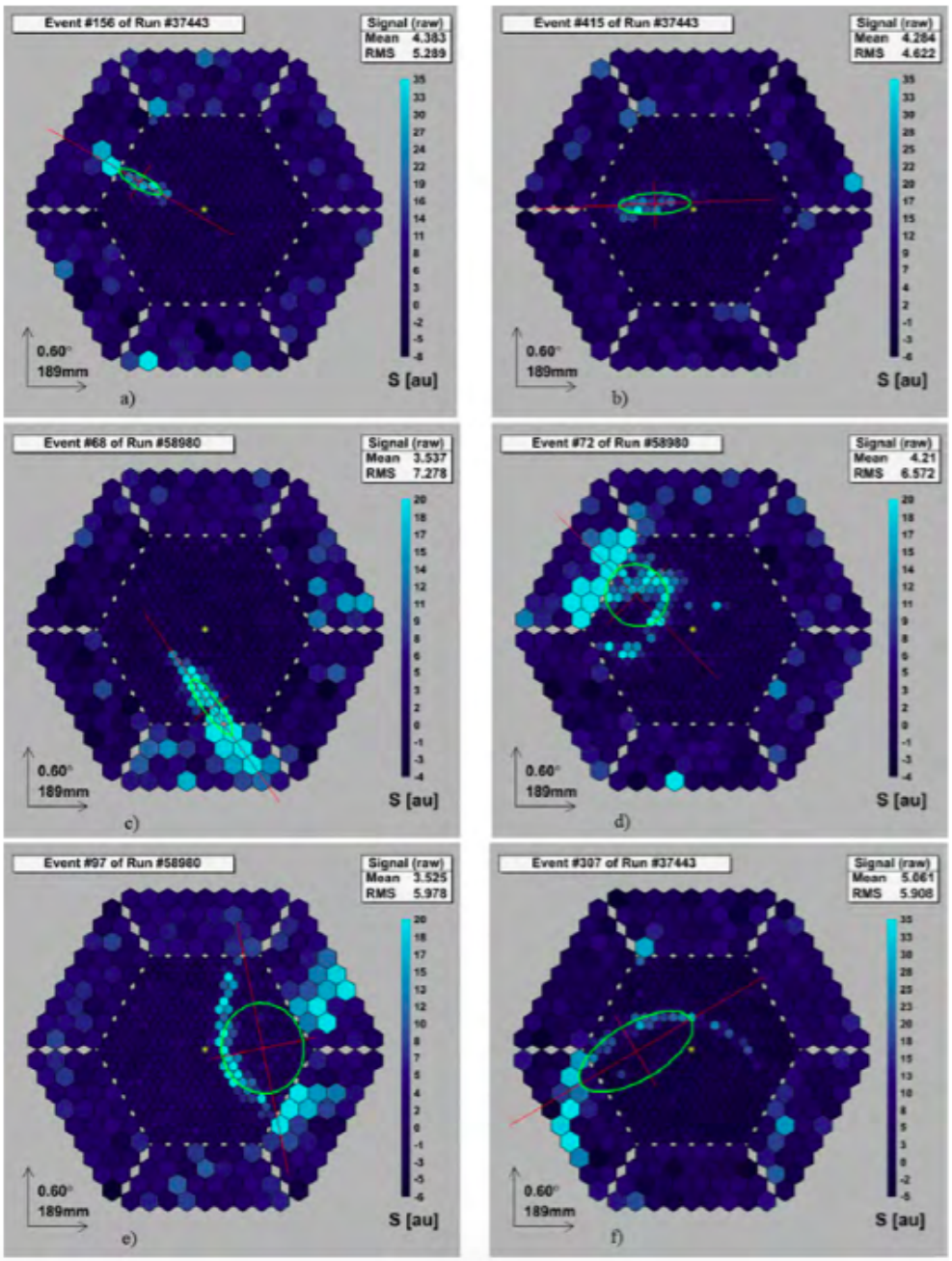

Figure 2.13: Different shower images by the MAGIC Telescope. Figures (a) and (b) show images by candidate γ particle, while figures (c), (d), (e) and (f) show images by candidate hadrons and muons.

$$\frac{S}{\sqrt{N}} = \rho_\gamma \cdot \sqrt{\frac{A\epsilon}{\Phi_N \Omega \tau}} \propto E_0 \cdot \sqrt{\frac{A\epsilon}{\Phi_N \Omega \tau}} \tag{2.30}$$

Defining the energy threshold E_{th} as the minimum energy of the CR to trigger the system with a fixed significance signal-to-noise, it is proportional to:

$$E_{th} \propto \sqrt{\frac{\Phi_N \Omega \tau}{A\epsilon}} \tag{2.31}$$

This formula shows the dependence of E_{th} from the quantum efficiency of the photo-detector (ϵ) and from the integration time of the front-end electronics (τ).

2.1.3 Current Main IACT Experiments

At the moment there are four large IACTs operating in the world: CANGAROO III, H.E.S.S., MAGIC and VERITAS, two are situated in the southern hemisphere and two in the northern hemisphere.

• CANGAROO III is a collaboration between Japan and Australia for a VHE γ-rays observatory, which is placed near Woomea in Australia. The structure is composed of four telescopes with a diameter of 10 m and a surface of 57 m^2 each, operating since March 2004.

• H.E.S.S. is a collaboration between Germany, France, United Kingdom, Ireland, Austria, Poland, Czech Republic, Armenia, Australia, Sweden, South Africa and Namibia. The observatory is located in Namibia near the Gamsberg mountain and it is formed by four telescope with a reflecting surface of 108 m^2 each and a large size telescope with a reflecting surface of 614 m^2 in the centre of the array. Four telescopes have been operating since early 2003, while the large size telescope has been inaugurated in September 2012.

• VERITAS is a collaboration between Canada, Ireland, United Kingdom and USA. The observatory is located near Tucson in Arizona and it is formed by four telescope with 12 m optical reflectors each. The array of CT has been

operativing since April 2007, but the prototype's telescope had been activated in February 2004

• MAGIC is a collaboration between Germany, Italy, Spain and Switzerland. The observatory is located in the Canary Island of La Palma and it is composed of two telescope with a reflecting surface of 236 m^2 each. The first telescope has been operativin since mid 2004, the second one since 2010.

2.2 The Cherenkov Telescope Array Observatory

The latest generation of the Imaging Atmospheric Cherenkov Telescopes has allowed the observation of high energy universe, establishing a new branch of astronomy. All these observatories have a close data policy with a limited access to the data for external scientists. This policy can be applied by the current IACTs, because the relative limited number of detected sources can be analysed and interpreted by the manpower in the IACT's group.

The creation and the operation of CTA-observatory will bring together and combine the experiences and the abilities of all groups working with IACT. An international collaboration will stimulate significant advances in technical, operation and data access, it will provide full-sky view from a southern and a northern site with unprecedented performances and it will assure an open data policy to the entire astrophysics (and particle physics) community.

The CTA observatory aims to exceed the science performances of current IACTs in different aspects:

- **Sensitivity:** CTA will be about 10 times more sensitive than current cherenkov telescope observatories.

- **Energy range:** CTA will cover three to four orders of magnitude in energy range. A wide-band coverage of electromagnetic spectrum is

crucial in very high energy astrophysics.

- **Angular resolution:** CTA will reach an angular resolution in the arc-minute range (a factor 5 better than the current instruments).

- **Temporal resolution:** CTA will resolve flaring and time-variable emission on sub-minute time scales.

Moreover, CTA will operate in a wide range of configurations, thanks to the large number of individual telescopes. This flexibility will allow CTA to observe in-deep individual objects with a unprecedented sensibility, to monitor simultaneous tens of potentially flaring objects and to survey wide region of the sky.

2.2.1 The Cherenkov Telescope Array Layout

The CTA community aims at a full-sky coverage and, for this reason, it plans to build two sites for the observatory, one in the southern hemisphere and another one in the norther hemisphere. Due to its position, the southern site will study the centre of the galactic plane and observe most of the galactic sources, it is therefore designed to optimize the sensitivity over the full energy range. Otherwise, the northern site will be in a perfect position to monitor and discover extragalactic source, therefore it will be optimised only for the highest energy.

As mentioned in the previous paragraph, the range of CTA will cover three to four orders of energy magnitude. Since one size of CT is optimized only for 1.5 - 2 decades in energy, three sizes of CT will form the array of CTA:

- **The low-energy range $\leq$ 100 GeV:** The observation of showers with energy of few tens of GeV requires an efficiently sampling and detecting system and a cherenkov light collecting of the order of 10%. For this

reason the CTA baseline design assumes a small number of large size telescope (LST), with a dish diameter of 20-30 m.

- **The core energy range from 100 GeV to 10 TeV:** Current IACT observatories have acquire a great experience in shower detection and reconstruction in this energy range, therefore the appropriate solution for CTA is an array of medium size telescope (MST) of 10-12 m diameter with a spacing of about 100 m. With this design the telescope array will be larger than the light pool, allowing a higher quality of shower reconstruction and improving array sensitivity.

- **The high-energy range above 10 TeV:** Showers with energy above 10 TeV emit light with a large yield, so the cherenkov light can be detected well beyond the 150 m radius of a typical light pool. In these cases there are two option: a large number of telescope with mirror of a few m^2 and a spacing of 100 to 200 m, or a smaller number of telescope with mirror of a tens m^2 and a spacing of several 100 m. The CTA baseline design assumes a large number of small size telescope (SST), with a diameter of 5-8 m.

An important parameter in the design of Cherenkov Telescope system is the array configuration, which will affect the sensibility of the array. Using simulations, several different telescope configurations have been studied to optimize the CTA design. Figure (2.14) shows a possible scheme for northern site, while figure (2.15) shows a possible scheme for southern one.

2.2.2 The Reflecting Surface of SST, MST and LST

A Cherenkov Telescope is primarily characterised by its mirror, its photon collection efficiency and its photo detection efficiency. Excluding the total reflective area, the other important parameters of mirror system are:

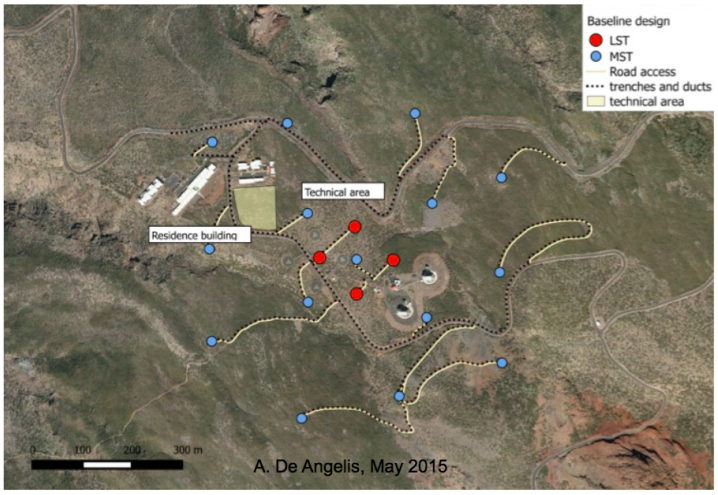

Figure 2.14: A CTA North possible scheme.

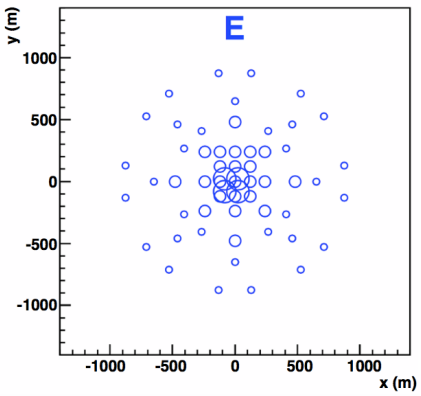

Figure 2.15: A CTA South possible scheme.

- **The point spread function:** The PSF indicates how well the mirror system concentrates light from a point source. If the RMS width of the PSF is less than 1/2 of camera pixel diameter the light containment is about 40%, for a Gaussian PSF, while for a RMS width better than 1/3 of pixel diameter, the containment is about 68%.

- **The time dispersion:** Due to its reflection point on the mirror, the cherenkov light can arrive at the camera through different paths. The result of this variability is a dispersion in the arrival time of photons on the detector, which should not exceed the width of 3 ns of Cherenkov light pulse from a gamma-ray shower.

In a Cherenkov Telescope, the reflector is usually segmented into individual mirrors, which are usually disposed in a parabolic layout or in a Davies-Cotton design. In the parabolic arrangement, the time dispersion is minimized and the approximate RMS width of the PSF, for a reflector of diameter d and focal length f, is:

$$\sigma_\zeta^2 = \frac{1}{512}\frac{\delta^2}{F^4} + \frac{1}{16}\frac{\delta^4}{F^2} \tag{2.32}$$

$$\sigma_\eta^2 = \frac{1}{1536}\frac{\delta^2}{F^4} \tag{2.33}$$

with F the focal ratio ($F = f/d$), δ the field angle, σ_ζ the width in the radial direction and σ_η the width in the azimuthal direction.

Figure 2.16 shows a typical Davies-Cotton design for a Cherenkov Telescope where the spherical mirrors of focal length f are disposed in on a sphere of radius f. For a Davies-Cotton reflector with a planar surface the approximate RMS width of PSF is:

$$\sigma_\zeta^2 = \frac{1}{1024}\frac{\delta^2}{F^4}\left(1 - \frac{1}{4F^2}\right) + \frac{1}{256}\frac{\delta^4}{F^2}\left(4 + \frac{35}{6F^2}\right) \tag{2.34}$$

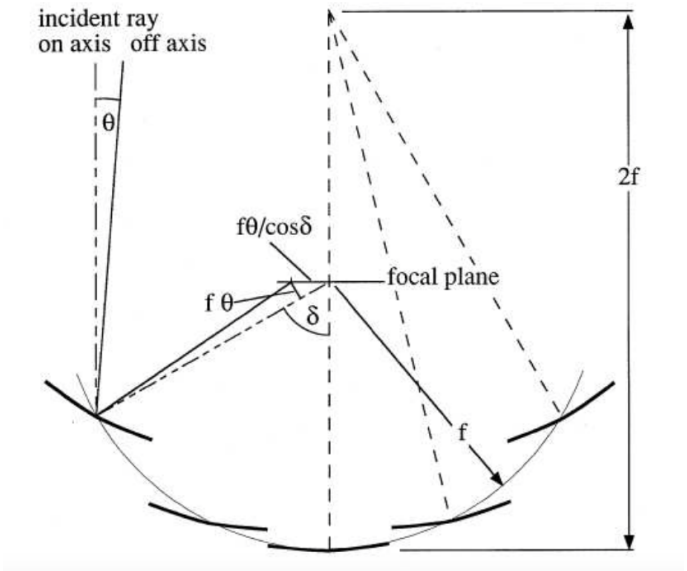

Figure 2.16: Davies-Cotton mirror layout, with mirrors of focal length f disposed on a sphere of radius f.

$$\sigma_\eta^2 = \frac{1}{1536}\frac{\delta^2}{F^4}\left(\frac{10}{9} + \frac{9}{32F^6}\right) \tag{2.35}$$

Respect to parabolic reflectors, in this case the difference between radial and azimuthal width is smaller. Considering the time dispersion of a Davies-Cotton layout, the only possible reflector for LST is a parabolic dish to achieve the performances goals for CTA large telescope. On the other hand Davies-Cotton single-reflector is the best solution for SST and MST at the moment. Until now dual mirror telescopes have never been used in Cherekov astronomy, however dual mirror designs are under study, with particular emphasis on the Schwardzschild-Couder design and some prototypes for SST (e.g. ASTRI) are under test. Although current CTA project plans to build single-reflector telescope for SST and MST, the dual-reflector design is a promising alternative.

2.2.3 The Photo Detection System in CTA

In a Cherenkov Telescope, the camera is the component employed in the photo detection. It has usually a cylindrical shell, which provides mechanical support for light sensor, read-out system, trigger system, cooling system and some associated systems as light-collection Winston cones and plexiglass input window. It is fixed to the arms of the telescope in the focal plane of the reflector. Each system of the camera is designed to optimize its photo detection efficiency.

Due to the high performances established by CTA project, the photo sensors must respect some important criteria:

- **Spectral sensitivity:** As mentioned in paragraph 2.1.2, the Cherenkov light suffers some scattering and absorption effects caused by atmosphere. For this reason the camera photo-sensor must be optimized to detect between 300 nm and 600 nm which is the spectrum range of the Cherenkov light at the ground.

- **Sensor area:** CTA designed pixel size is around 0.1° for the LST, 0.18° for the MST and 0.25° for the SST. For conventional single reflector telescope these angular size correspond to linear dimension of 40 mm, 50 mm and 35 mm, respectively. If a two-mirror design will be adopted for SST and MST, a pixel with linear dimension of 6 mm will correspond to angular size of 0.2° and 0.07°, respectively.

- **Sensor uniformity:** CTA design parameters constrain the sensor non-uniformities below 10%.

- **Dynamic range and linearity:** The sensors should be able to detect single photons and provide a dynamic range of up to 5000 photo-electrons, with linearity deviations below a few per cent.

- **Temporal response:** The sensors should be able to preserve the timing of the Cherenkov light pulse detected with a sub-nanoseconds precision in pulse arrival times, for large light pulses.

- **Lifetime and aging:** CTA project plans to use sensors with a lifetime of 10 years with an annual exposure of about 2000 hours. Moreover, they should have good short and medium term stability, and only gradual aging.

- **Rate of spurious or fake signals (Afterpulse and Cross-talk):** The contamination of real signals by spurius signals, such as afterpulses and cross-talk, should not exceed $\sim 0.1\%$ and 1%, respectively.

In the current IACTs, the photo detectors are usually photomultiplier tubes (PMTs) with bialkali photocathodes. This model of PMT provides the highest QE and it is sensitive to the radiation in the wavelength range between 300 nm and 600 nm (200-600nm with a quartz window). PMTs are the baseline solution in CTA design, new photo sensors are under study with particular emphasis on silicon photomultipliers (SiPMs) and multi-anode photomultipliers (MAPMTs).

3

The Detection of Photons: Present and Future Detectors in CTA

Photomultiplier tube (PMT) is an electron tube device, which converts light into a measurable electric current. In the last century, this technology has been used in many experiments, thanks to its high sensitivity and gain. New products, however, are growing into a viable alternative to PMT, *i.e.* the multi-anode photomultiplier tube (MAPMT) and the silicon photomultiplier (SiPM), also called multi-pixel photo counter. This chapter presents the structure, the mode of operation, the operating parameters and the performances of these devices and shows the benefits of using SiPMs in Cherenkov telescopes.

3.1 Photomultiplier Tube

Created by Elster and Geiter in 1913, the PMTs, also called vacuum photomultiplier tubes, are important devices in many branches of physics, for example, particle physics, gamma-ray astrophysics and medical physics. Many type of PMTs have been produced from 1913 but the typical photomultiplier tube has the schematic diagram shown in figure 3.1.

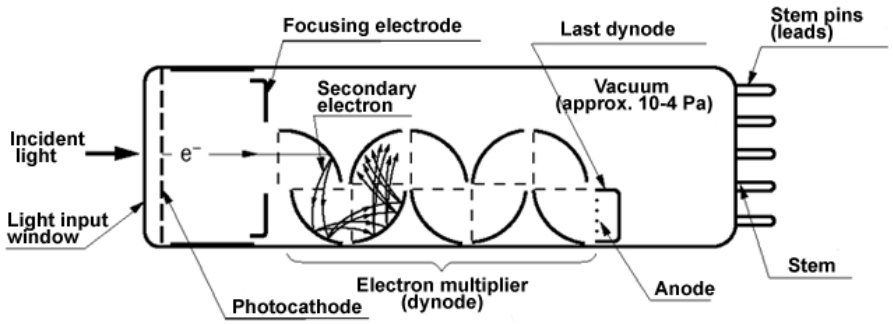

Figure 3.1: Schematic diagram of a photomultiplier tube.

3.1.1 Photomultiplier Tube Basic Structure

A photomultiplier tube can be divided in four stages [13], [14]:

- **Photo-conversion stage:** A semi-transparent photocathode converts the incident photons in electrons. The effeciency of the photoelectron conversion, called quantum efficiency (QE), is strongly dependent on the photocathode's material and the doping. Moreover, the QE is a function of incident photo wavelength (λ) and can be expressed with the formula:

$$QE(\lambda) = \frac{\text{number of photoelectrons released}}{\text{number of incident photons on cathode } (\lambda)} \tag{3.1}$$

  Due to the greater quantum efficiency of semiconductor, most of the photocathodes is made of this material; in fact the typically quantum efficiency of metals is not greater than 0.1 %, while semiconductors have QE of the order of 10 to 40 %.

- **Electron focusing stage:** An electron optical input system focuses and collects the electrons emitted by photocathode onto the electron multiplication stage. The two important requirements of this component are the collection efficiency, which must be maximized, and the travel

time from the cathode to the next stage, which must be as independent as possible of the point of emission.

- **Electron multiplication stage:** An electron-multiplier amplifies the weak incoming photocurrent with a series of secondary emission electrodes or dynodes to produce a measurable outgoing current. A dynode produces δ electrons for each incident photoelectron, therefore for N dynodes in a PMT the gain of the device is:

$$\text{overall gain} = \alpha\delta^N \tag{3.2}$$

where α is the fraction of all photoelectrons collected by the multiplier structure, while δ is known as the secondary emission factor. Conventional dynode has a typical value of $\delta = 5$ and α is near unity for well designed tubes. Therefore, common PMTs with 10 dynodes can obtain an overall gain of 5^{10}, or about 10^7.

Dynodes can be made in many ways, figure 3.2 shows some common dynode's configurations.

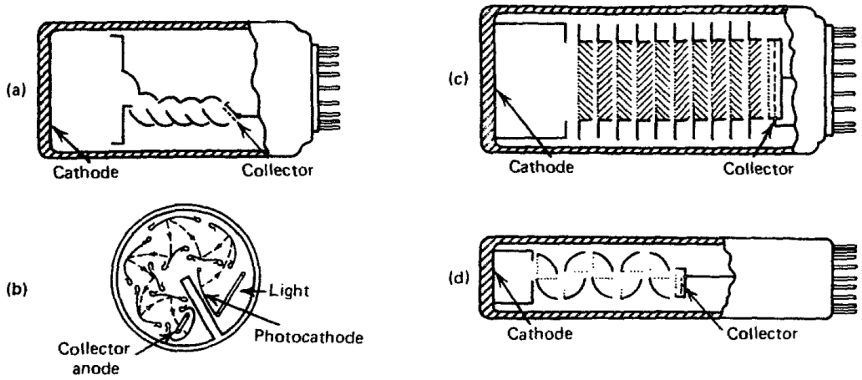

Figure 3.2: Dynode configuration of some common type of PMTs: (a) linear focused, (b) circular grid, (c) venetian blind, (d) box-and-grid [14].

- **Pulse formation:** Finally the electron cascade generated by the electron multiplication stage is collected by an anode, which carries this current outside of PMT to operational amplifiers and electronic analysers.

3.1.2 Operational Parameters and Performances

Photo Detection Efficiency

In a photomultiplier tube the photon detection efficiency (PDE) can be defined as the probability for an incoming photon to produce a detectable output signal from photomultiplier tube. Main contribution to PDE comes by the photo-conversion stage and electron focusing stage.

As mentioned previously, in the first stage of a photomultiplier tube an incident photon is converted in an electron which escapes from photocathode into the PMT. Since a photocathode with a thick layer increases the chance of photon absorption while a thin layer enhances the chance for the photoelectron to escape into the PMT, this process require a compromise which intrinsically limits the highest PDE values that can be achieved with the PMT technology.

In the electron focusing stage the electron emitted by photocathode is accelerated by electric fields and focused onto the first dynode. The stronger the amplitude of the electric field between photocathode and first dinode, the greater the efficiency of the process will be. Therefore, it is a desirable feature to set the voltage between the photocathode and the first dynode as high as practically feasible to avoid losses of efficiency, however, an upper limit for the voltage is generally imposed to prevent electron arcs inside the tube.

Voltage Supply and Gain

An external voltage source of the order of thousands of volts must be connected to PMT tube to achieve gain at the level of 10^7. The overall gain of a PMT depends on the number of dynodes in the multiplier section and the secondary

emission factor δ, which is a function of the energy of the incident electron on each dynode. Since this energy is clearly a function of the potential difference, V_d, between dynodes the δ can be write:

$$\delta = KV_d \tag{3.3}$$

where K is a proportionality constant. From 3.2 and assuming the applied voltage is equally divided among the N dynodes of the multiplication stage and $\alpha \sim 1$, the overall gain G of the PMT is then

$$G = \delta^N = (KV_d)^N \tag{3.4}$$

and the supply voltage V_b is:

$$V_b = NV_d = \frac{N}{K} G^{1/N} \tag{3.5}$$

From 3.4 it is interesting to calculate the derivate of G respect to V_d:

$$\frac{dG}{dV_d} = NK^N V_d^{N-1} \tag{3.6}$$

then

$$\frac{dG}{G} = N\frac{dV_d}{V_d} = N\frac{dV_b}{V_b}. \tag{3.7}$$

Equation 3.7 implies that for $N = 10$ to maintain a gain stability of 1%, the voltage supply must not change more than 0.1%.

Electron Current and Linearity

Although the linearity of a PMT depends on the type of dynode configuration and the current in the tube, in general the outgoing current is proportional to the energy and intensity of incident light, as long as the current at each stage is entirely collected by the previous stage.

Figure 3.3 shows the dependence of the cathode and anode currents on the applied voltages for incident light on photocathode at different light intensity. The initial dependence on voltage is due to the formation of a space charge around the emitting electrode which tends to prevents the acceleration of subsequently emitted electrons towards the receiving electrode. However, increasing the voltage this space charge is swept away and all current is collected. As a general rule, therefore, the cathode, dynodes and anode currents should always be in the flat, saturated portion of the characteristic curve.

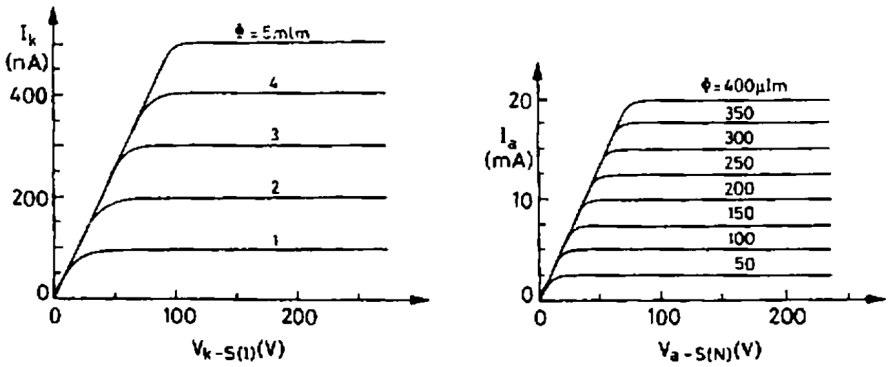

Figure 3.3: Current-voltage characteristics of PMT cathode and anode under different illuminating light intensities [13].

Maintaining these voltages during operation it is difficult because the emission of small current from dynodes or photocathode can cause large change in their potential and therefore alter the collection efficiency. For this reason it is important to work at sufficiently high voltage so as to ensure staying on the flat part of the characteristic curve.

Pulse Shape

The output signal of photomultiplier tube is a charge pulse whose total charge is proportional to the initial number of electrons emitted by the photocathode. The equivalent circuit of PMT is a current generator in parallel with a

resistance R and a capacitance C, which represent the intrinsic resistance and capacitance of the anode and some other elements in the output circuit.

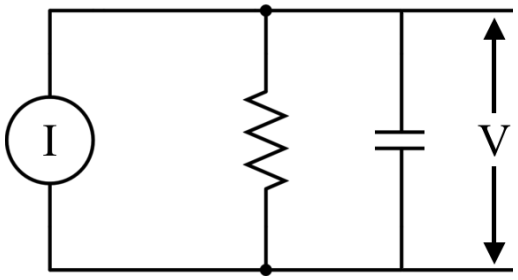

Figure 3.4: Equivalent circuit for a photomultiplier tube [13].

The behaviour of the signal at the circuit output is described by formula 3.9, which gives the output current at the anode, assuming that the input of PMT is scintillator's light, described by an exponential decay:

$$I(t) = \frac{GNe}{\tau_s} \exp(\frac{-t}{\tau_s}). \tag{3.8}$$

where G is the gain of PMT, N is the number of photoelectrons emitted by photocathode, e is the charge of the electron and τ_s is the decay constant of scintillator. Then the equation of RC circuit is:

$$I(t) = \frac{V}{R} + C\frac{dV}{dt} \tag{3.9}$$

which has the solution

$$V(t) = \begin{cases} -\frac{GNeR}{\tau - \tau_s}\left[\exp\left(-\frac{t}{\tau_s}\right) - \exp\left(-\frac{t}{\tau}\right)\right] & \tau \neq \tau_s \\ \left(\frac{GNeR}{\tau_s^2}\right) t \exp\left(-\frac{t}{\tau_s}\right) & \tau = \tau_s, \end{cases} \tag{3.10}$$

where $\tau = RC$. Figure 3.5 shows output signal for different values of τ with some typical value of G, N, C and τ_s.

For $\tau \ll \tau_s$ the signal is small, but reproduces the decay time of the initial signal and the rise time is essentially given by the τ output circuit. Otherwise

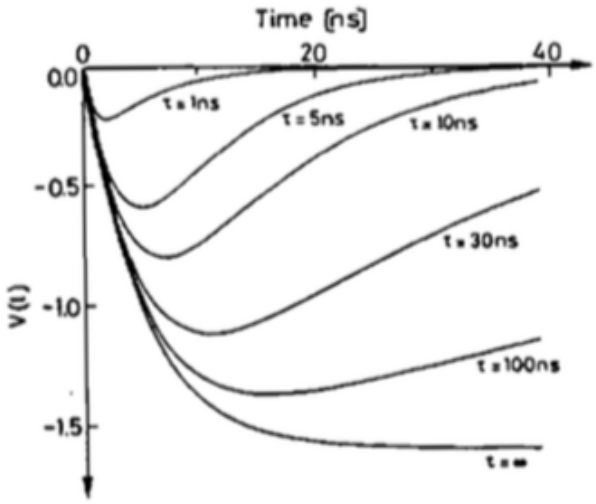

Figure 3.5: Output signals for various time constants τ with some typical values: $G = 10^6$, $N = 100$, $C = 10$ pF and $\tau_s = 5$ ns [13].

for $\tau \gg \tau_s$ the signal amplitude becomes larger but so does the decay time which is now basically defined by τ. For optimal performance, the PMT output circuits must be tailored to the specifications of the detector. This usually involves altering the resistance R so as to obtain a suitable τ, while the capacitance C is usually kept as small as possible in order to maximize the amplitude.

Time Response and Time Resolution

Since the time required for photoemission in the photocathode or secondary emission from dynodes is very short (0.1 ns or less), the time response of the PMT are determined exclusively by the time needed by electrons to transit through the PMT. The *transit time* (a.k.a. *electron transit time*) of a PMT is defined as the average time difference between the arrival of a photon at the photocathode and the collection of the subsequent electron burst at the anode. In a PMT, the electron transit time (and the time response) ranges

from 20 to 80 ns, depending on the design of the device.

Since the time resolution of a photomultiplier tube depends on the response of the device to incident photons, it is affected by two main factors:

1. Variation in the transit time,

2. Fluctuations due to statistical noise.

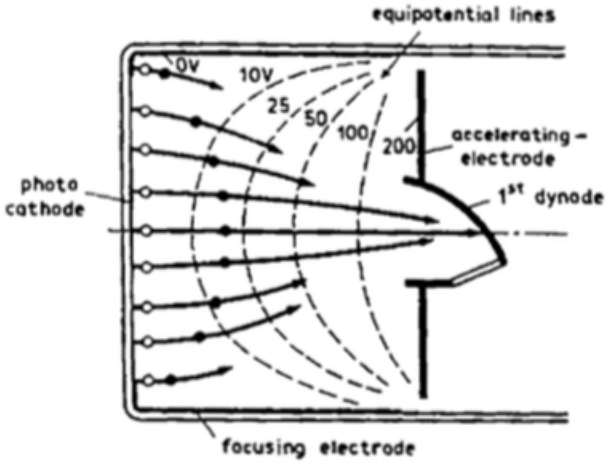

Figure 3.6: Transit time difference [13].

Transit time variation may arise from differences in the path length of electrons and from dissimilarity in the energy of electrons emitted by photocathode. Figure 3.6 shows the first effect, which is called *transit time difference*. It is due to the variation of distance from photocathode to first dynode between the center and the edge of the cathode. A simple solution is to grade the electric field in such a way that the electrons at the edge are accelerated more than those on the PMT axis.

Apart from geometrical effects, there will also be variations which depend on the energy and direction of the emitted electrons. Electrons emitted with a higher energy or in a direction closer to the normal of the cathode will reach the first dynode before those emitted at lower energy or in a direction

more parallel to the surface. This effect is called *transit time spread* and it is independent from the point where the electrons leave the cathode. In this case the transit time spread can be approximated by the formula

$$\Delta t = -\sqrt{\frac{2m_e W}{e^2 E^2}} \tag{3.11}$$

where m_e is the electron mass (9.1×10^{-28} g), e is the charge of electron ($1,6 \times 10^{-19}$ C), E is the electric field strength [V/m] and W is the energy component normal to the cathode ($v_\perp^2/2m_e$ with $v_\perp = v - v_{||}$ the perpendicular component of velocity). In modern PMT, typical values of the transit time are of the order of 0.2 to 0.5 ns.

The second source of time response fluctuations is due to the statistical nature of the photoelectric effect and secondary emission process, which cause variations in the PMT current. This is known as *statistical noise* and it constitutes a fundamental limitation to the time resolution of the PMT.

Noise: Dark current and Afterpulsing

Even when a photomultiplier is not illuminated, a small current still flows. This current is called the *dark current* and arises from several sources:

1. thermionic emission from the cathode and dynodes
2. leakage currents
3. radioactive contamination
4. ionization phenomena
5. light phenomena.

Thermal noise is the main component and its contribution is described by Richardson's equation:

$$I = AT^2 exp(\frac{-e\phi}{kT}) \tag{3.12}$$

where A is a constant, ϕ is the work function, T is the temperature (in kelvin degree) and k is the Boltzmann's constant. A lower temperature clearly reduces this component of noise.

Other important sources of noise are the ionization phenomena and light phenomena. Residual gases left or formed in the PMT can be ionized by the electrons and since they are of opposite charge, will accelerate back towards the cathode or dynode where they can release further electrons. This often outcomes in afterpulse, occurring in a time equal to the time needed for ions to transit the tube (from a few hundred nanoseconds to microseconds). Under high current, afterpulses may also be caused by *electron glow*, i.e., light emitted by the last few dynodes which travels to the photocathode. In this case, afterpulses occur between 30 to 60 ns after the true pulse.

Environmental Factors: Ambient Light and Magnetic Fields

Since the photomultiplier tubes are extremely photosensitive, the ambient light (e.g. moon light) is harmful to PMTs, while they are under voltage. In such case, the resulting high currents in the tube can give rise to instability (*fatigue*) effects or event destroy the PMT entirely.

Magnetic fields do not damage the PMT, but they have important influences on the operation of devices. A small magnetic field is enough to deviate the electron cascade in a PMT and, therefore, to affect its efficiency. Ways to make PMT less sensitive to magnetic fields are reducing the distance between the photocathode and the first dynode or shielding the device with a mu-metal screen, however, they will be always affected by magnetic fields.

3.1.3 Multi-Anode Photomultiplier Tube

The multi-anode photomultiplier tube (MAPMT) is a position sensitive photodetector which is an evolution of PMT technology. This device is composed by a single photocathode layer, an electron focusing system and a matrix of pixels. The photocathode converts the incident photons in electrons, while the focusing system direct the emitted charges to a pixel of the matrix. Each pixel contains a dynode chain and an anode, which amplifies the weak incoming photocurrent and carries the outcome intensified current outside the MAPMT to the read-out system. A MAPMT device can be seen as an array of small PMTs all contained within a single module and supplied by a single voltage line.

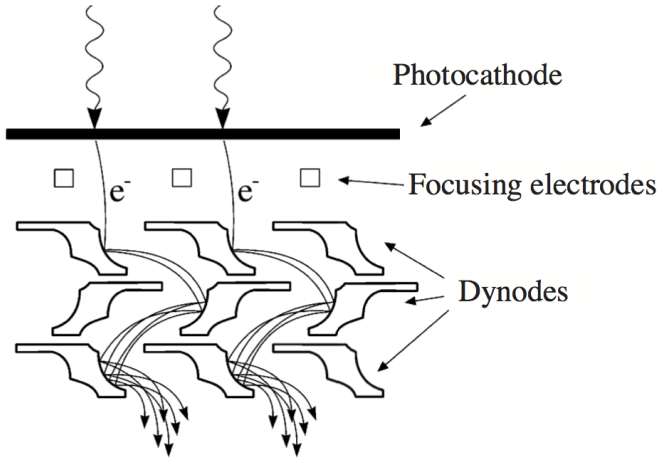

Figure 3.7: Schematic view of the multiplication process inside a MAPMT.

Figure (3.8) shows a MAPMT of H10966 series from Hamamatsu Photonics, it is an 8x8 matrix of pixels with physical dimension of 52x52 mm^2 and 49x49 mm^2 of effective area. Each pixel is composed of 8 dynodes, which are supplied by a single high voltage line. The devices of H10966 series use a photocathode made of biakali or super-biakali, which achieves a spectral response with a range from 300 nm to 650 nm and a peak at 400 nm.

Figure 3.8: Hamamatsu MAPMT H10966: 8x8 pixel array, 52x52 mm^2 of physical dimension.

Due to years of experience with PMTs in Cherenkov telescopes, MAPMTs are a fairly familiar option and a natural continuation for the next generation of telescopes. However, PMT technology comes with non-negligible drawbacks:

- Fragility (sealed vacuum tube)
- Operation under high voltage (typically $\sim$ 1000 - 1500 Volts)
- Aging (due to heavy bombardment of the last dynode)
- Limited photon detection efficiency
- Sensitivity to Earth magnetic fields
- Large afterpulses

3.2 Silicon Photomultiplier

Silicon Photomultipliers (SiPMs) are one of the more promising devices in the field of semiconductors sensors. Due to their performances (single photon sensibility, fast response, good Photon Detection Efficiency (PDE)), these sensors have the potential to replace the conventional detectors, such as the PMTs, in a large number of applications, included gamma ray detection. Moreover, silicon photomultipliers have advantages over photomultiplier tubes, such as immunity to magnetic fields, better ruggedness and compactness.

3.2.1 Silicon Photomultiplier Working Principles

A SiPM is essentially a high-density matrix of avalanche photodiodes operating in Geiger mode (GM-APDs) connected in parallel on a common silicon substrate. Each GM-APD cell is a reverse-biased pn-junction and is connected in series with a quenching resistance (fig.3.9).

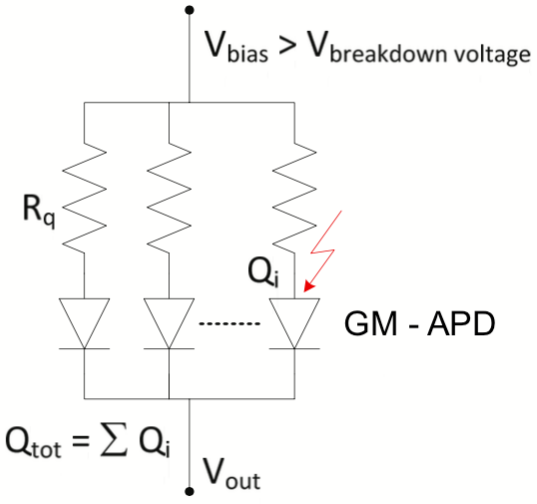

Figure 3.9: GM-APD cells connected in series with quenching resistances.

A pn-junction is the juxtaposition of a p-type semiconductor with a n-type material which creates a special zone on the interface between the two mate-

rials, called *depletion* zone or *space charge region*. Because of the difference in the concentration of electrons and holes[1] between the two material, there is an exchange of electrons and holes which causes a charge build-up to occur on either side of the junction. The p-region is injected with extra electrons and it becomes negative while the n-region becomes positive (fig 3.10). This creates an electric field gradient V_0 across the junction leaving a region, the depletion zone, with the special property of being devoid of all mobile charge carriers. In fact, any electron or hole created or entering into this zone will be swept out by the electric field.

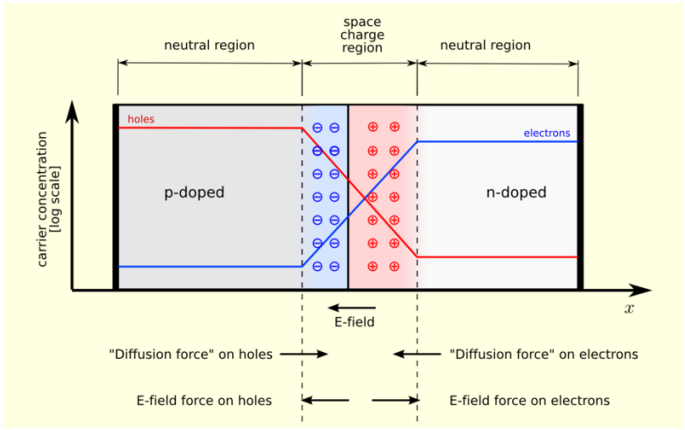

Figure 3.10: Schematic diagram of a pn-junction.

Ionizing radiation entering this zone will liberate electron-hole pairs which are then swept out by electric field. If electrical contacts are placed on either end of the junction device, a current signal proportional to the ionization will then be detected.

Since the intrinsic field of a pn-junction is not sufficiently intense to provide efficient charge collection, an unbiased pn-junction does not present the best operating characteristics. Better results can be obtained by applying a reverse-

[1] An electron hole, or hole, is the lack of an electron at a position where one could exist in an atom or atomic lattice.

bias voltage to the junction, i.e. a negative voltage to the p-side (fig.3.11). Under reverse voltage the total potential of electric field is:

$$V_{tot} = V_0 + V_B \tag{3.13}$$

where V_B is the magnitude of the applied reverse-bias voltage. Moreover, V_B attracts the holes in the p-region away from the junction and towards the p contact and similarly for the electrons in the n-region, enlarging the depletion zone (fig. 3.11).

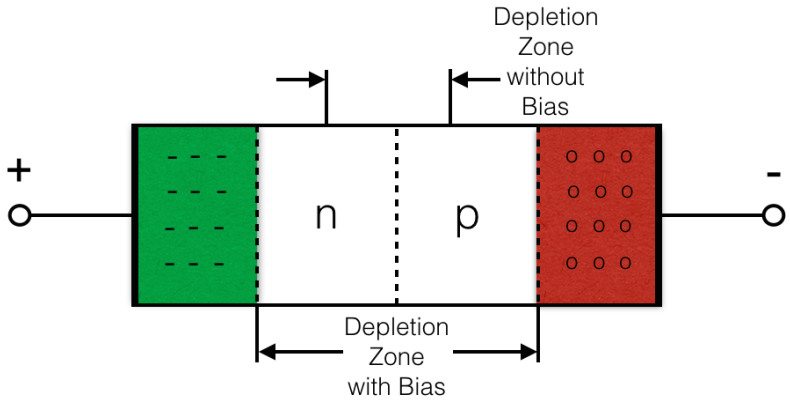

Figure 3.11: Reversed-bias junction.

Over a specific voltage, called breakdown voltage (V_{bd}), the reverse-biased current increases rapidly and the pn-junction conducts also in reverse bias. This change in the behaviour of pn-junction is mainly due to the avalanche effect. This process occurs when electrons and holes, moving across the space charge region, acquire sufficient energy from the electric field to create electron-hole pairs colliding with atomic electrons within the depletion region.

Since each GM-APD is a reverse-biased pn-junction which operates above V_{bd}, photons or thermal excitations in the depleted zone will produce a pair of charge carriers (electron-hole), which can trigger an electron-hole avalanche,

generating a current pulse. The quenching resistance, in series with the GM-APD, stops the avalanche and resets the cell to the initial state so that it becomes photosensitive again.

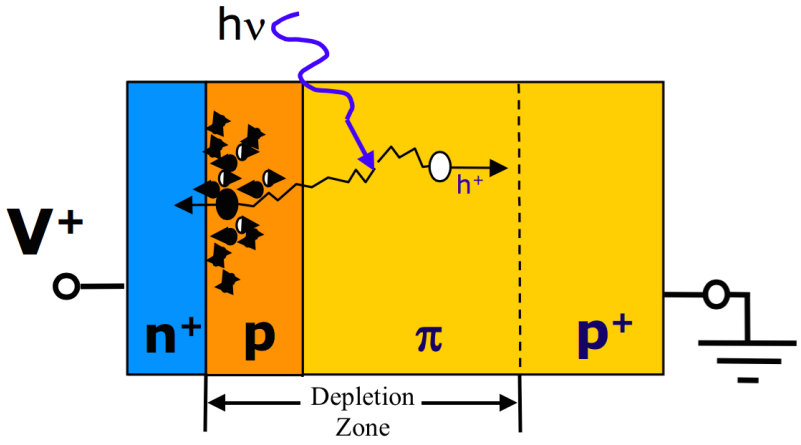

Figure 3.12: Electron-hole avalanche in a SiPM cell triggered by a photon. To prevent the creation of a depletion zone between metal and semiconductor a heavy doped layer of n^+ and p^+ material is used between the semiconductor and the metal leads. The π region is the epitaxial layer, which forms the drift region with low built-in electric field.

Figure 3.13 shows the voltage and current behaviour in a GM-APD cell when it is triggered. When the avalanche multiplication starts, the cell discharges a certain amount of charge, generating a current. At the same time the quenching resistor drops the operation voltage until it falls below the breakdown voltage and the avalanche multiplication is stopped. The current is then fallen to zero and the voltage rises again to its initial value V_B

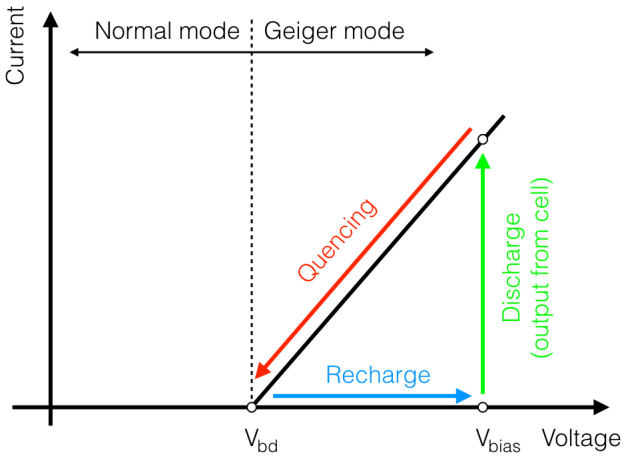

Figure 3.13: Behaviour of current and voltage in a GM-APD cell, during an avalanche multiplication.

3.2.2 Operating Parameters and Performances

Photo Detection Efficiency

As for the PMT the photon detection efficiency (PDE) in silicon photomultiplier is the probability for an incoming photon to produce a detectable output signal. In a SiPM many factors contribute to PDE which can be summarized by the formula:

$$PDE = P_{transmission} \times QE(\lambda) \times P_{avalanche} \times \epsilon_{fillfactor} \tag{3.14}$$

Each element of equation 3.14 expresses a factor which influences the PDE: $P_{transmission}$ is the transmission probability for an incident photon to enter the depleted region, $QE(\lambda)$, called quantum efficiency, is the probability for a photon to excite an electron from the valence to the conduction band inside the depleted region, thus creating a pair of charge carriers (electron-hole), $P_{avalanche}$ is the probability for an electron-hole pair to initiate an avalanche

in a GM-APD cell and $\epsilon_{fillfactor}$ is the ratio between the active area of the GM-APD cells and the total area (active area plus dead area).

Voltage Supply and Gain

Due to their nature, a matrix of GM-APD connected in parallel, SiPMs need a low voltage source (typically $\sim$ 20 - 100 Volts) with a low power consumption ($\leq$ 50 μ W/mm^2).

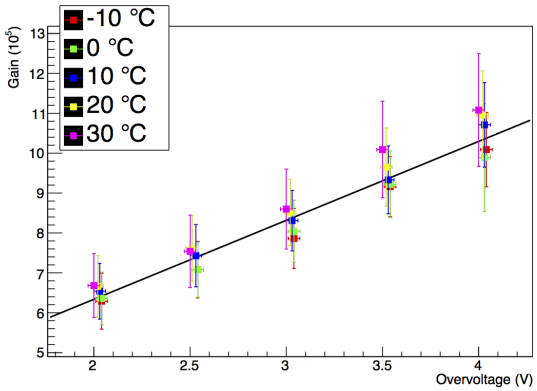

Figure 3.14: Gain measurements on FBK Near Ultra Violet SiPM with a square cell pitch of 50 μm, at different temperatures (-10 °C to 30 °C).

The gain achieved by silicon photomultipliers is at the level of 10^5 - 10^6 and it is strongly correlated with SiPM bias voltage V_{bias}. Figure 3.14 shows the linear dependence between SiPM gain and its overvoltage V_{over}, which is the difference between the bias voltage and the breakdown voltage ($V_{over} = V_{bias} - V_{bd}$). This correlation can be simply understood by modelling each GM-APD depleted region with a capacitor of capacitance C_{cell}. The charge flowing during capacitor discharge is then:

$$Q = Gain \times e = C_{cell}(V_{bias} - V_{bd}) = C_{cell}V_{over} \tag{3.15}$$

where e is the charge of electron ($1.6 \cdot 10^{-19}$ C). Therefore, the gain is:

$$Gain = \frac{C_{cell} \times V_{over}}{e} \tag{3.16}$$

The pulse-to-pulse SiPM gain fluctuations can be quantified by the width of 1 photoelectron peak (fig.3.15) and they are extremely small. These performances are due to the excellent cell-to-cell uniformity achieved during manufacturing of SiPM.

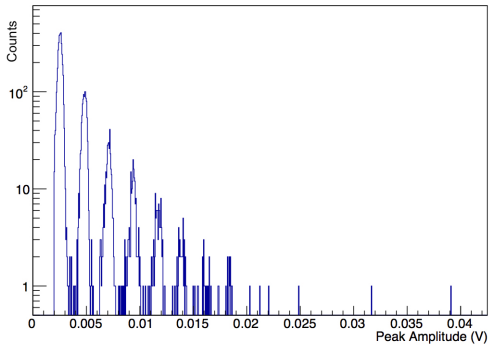

Figure 3.15: Pulse amplitude distribution of FBK Near Ultra Violet SiPM with a square cell pitch of 50 μm.

Pulse Shape and Photon Linearity

A GM-APD generates a pulse when one or more photons hit its sensitive area. Figure 3.16a shows a typical GM-APD pulse, its rise and fall are proportional respectively to $(1 - e^{\frac{-t}{\tau_d}})$ and $e^{\frac{-t}{\tau_q}}$. The variable τ_d is the rise time, while τ_q is the fall time and they are equal to:

$$\tau_d = R_d C_d \qquad \text{and} \qquad \tau_q = R_q C_d \tag{3.17}$$

where R_d and C_d are the equivalent resistance and capacitance of photodiode, while R_q is the quenching resistance (see fig.3.16b). The single GM-APD does not give information on light intensity, but only if a photon hits the sensitive area.

As mentioned previously a SiPM is a high-density matrix of GM-APD cells connected in parallel. Since each cell is independent and gives the same

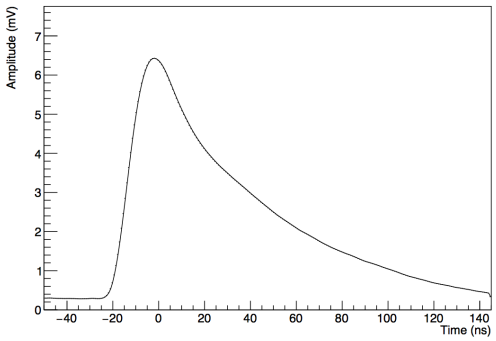

(a)

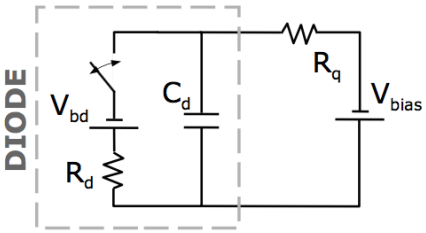

(b)

Figure 3.16: (a) Typical GM-APD pulse of FBK Near Ultra Violet SiPM with a square cell pitch of 50 μm. (b) Equivalent circuit of a GM-APD cell with a quenching resistance in series.

signal when it is hit by a photon, the output signal is the sum of pulses from GM-APD fired by a photon and its height is proportional to the number of incident photon (fig. 3.17).

Time Response and Time Resolution

In a silicon photomultiplier, the very high fields ensures that the transit time through the avalanche region is very short and the time response of the device very fast, typical rise time is of the order of few ns. Typical time resolution is less than a nanosecond and can be less than 0.1 ns under favourable circumstances. Three main factors affect the time resolution:

1. Variations of pulse rise time between cells

2. Pulse width

3. Fluctuations due to statistical noise.

A typical GM-APD pulse has a rise time proportional to its equivalent resistance and capacitance (eqn. 3.17). A disuniformity of these two parameters

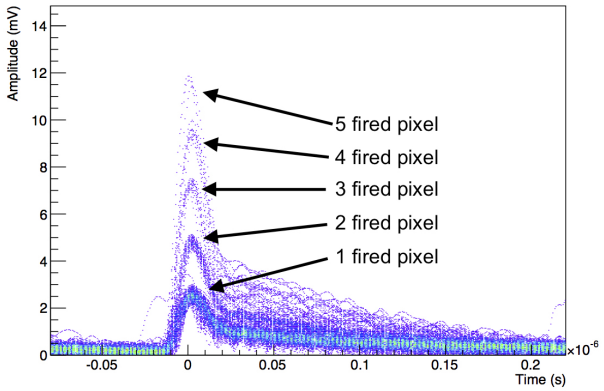

Figure 3.17: Typical output signals of FBK Near Ultra Violet SiPM with a square cell pitch of 50 μm.

between cells produces fluctuations in the time response. However, the excellent cell-to-cell uniformity, achieved during manufacturing of SiPM, strongly decreases this effect (fig. 3.17).

Due to its fall time the width of a GM-APD pulse can be of the order of 150 ns affecting the time response of the device. The rise time, however, remains short enough that a high pass filter can be used to significantly reduce the pulse width (fig. 3.18).

The third source of time response fluctuations is due to the statistical nature of the photoelectric effect and avalanche process and it constitutes a fundamental limitation to the time resolution of the SiPM.

Noise: Dark noise, Cross-talk and Afterpulsing

Even when a silicon photomultiplier is not illuminated, thermal excitation can generate a free electron inside the SiPM depletion region leading to a pulse. This so called dark pulse is a spurious avalanche that occurs randomly and independently from the illumination field and is indistinguishable from a photoelectron pulse. This *dark noise* depends from several factors, such as the

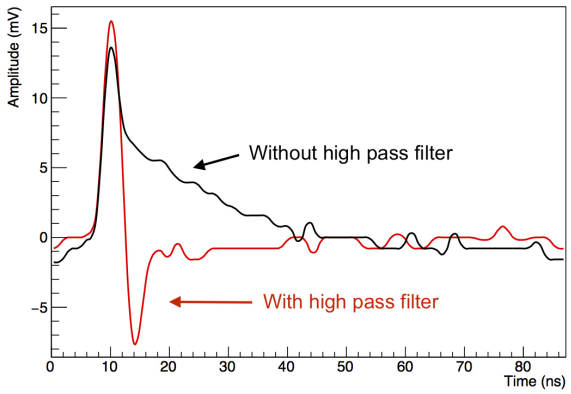

Figure 3.18: Same GM-APD pulse, with and without a high pass filter.

sensor design and the operational temperature. The triggering probability is the probability that a charge carrier, generated by a thermal photon, develops an avalanche. Given that both the junction thickness and the triggering probability are proportional to the overvoltage, also the dark noise is influenced by it. The dark noise frequency is usually referred to the number of spurious avalanche per unit of time. Figure 3.19 shows some of these frequencies as a function of temperature and overvoltage.

Although dark noise is an ineradicable source of noise in our device, due to its nature, it is not a significant source of noise in detectors which operate in a naturally noisy environment (*e.g.* Imaging Air Cherenkov Telescope).

An other important source of noise is the *cross-talk*, in which photons developed during an avalanche trigger secondary avalanches in surrounding cells. The light propagation inside the silicon substrate is essentially instantaneous, therefore the output pulse will be a superposition of the signal from the original photo-triggered cell and the cross-talk cells.

The cross-talk probability ($P_{crosstalk}$) is the probability that a cross-talk event happens and it can be easily obtained from SiPM pulse amplitude distribution (fig. 3.15) as:

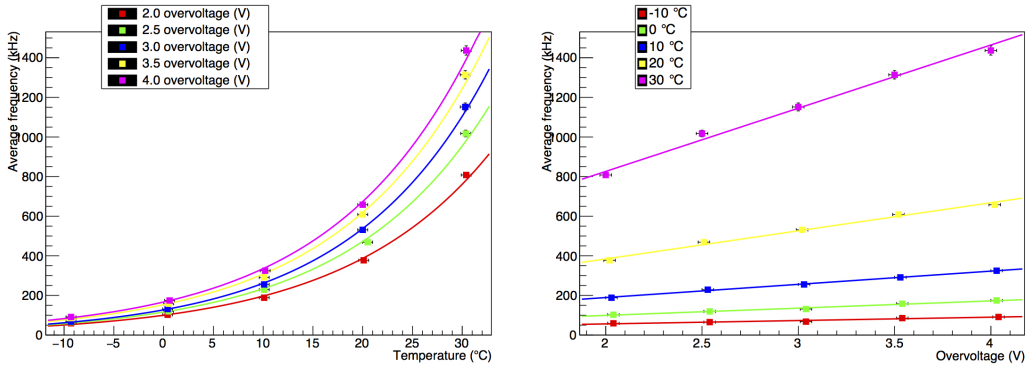

(a) (b)

Figure 3.19: Some typical frequencies of dark noise for a FBK Near Ultra Violet SiPM with a square cell pitch of 50 μm and 3x3 mm^2 area as a function of temperature (a) and overvoltage (b).

$$P_{crosstalk} = \frac{N_{>1.5pe}}{N_{>0.5pe}} \tag{3.18}$$

where $N_{>0.5pe}$ and $N_{>1.5pe}$ are the number of pulse exceeding the 0.5 and 1.5 levels of the single cell amplitude. Higher overvoltage increases the number of photons emitted by an avalanche, and the probability of a secondary avalanche triggered by one of these photons. The $P_{crosstalk}$ is therefore connected with overvoltage.

Esplecially for IACT cross-talk is an important source of noise because it can amplify the effects of the naturally noisy environment (*i.e.* night sky background), however, it can be suppress using trenches around each cell for optical isolation from surrounding cells at the price of lower fill factor.

The last important source of noise in silicon photomultiplier is the *afterpulse* (a.k.a. *afterpulsing*). This form of noise is due to charge carries from an initial avalanche trapped by impurities of silicon substrate which trigger delayed avalanche when they are released. Since the second avalanche is triggered in the same cell when it is recharging, the output pulse will be the sum

of the original photo-triggered cell pulse and a second pulse, lower and later than original one (fig. 3.20).

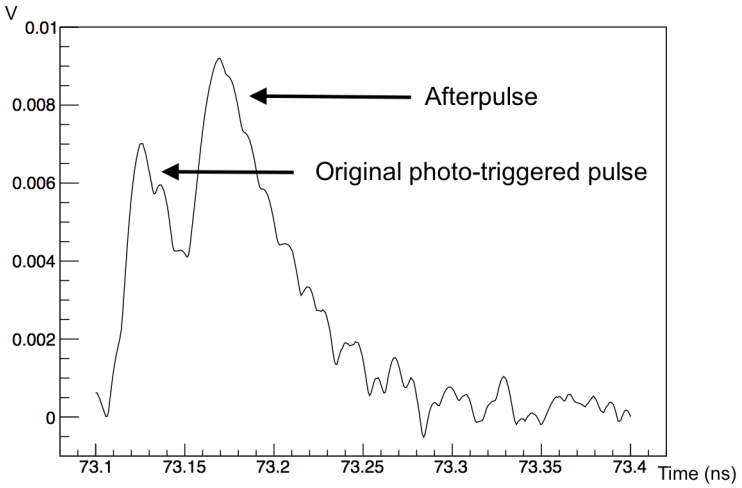

Figure 3.20: Typical afterpulse noise.

The afterpulse probability ($P_{afterpulse}(\Delta t)$) is the probability that an afterpulse event occurs after a time interval Δt from the original avalanche and can be describe as:

$$P_{afterpulse}(\Delta t) = P_t \frac{e^{\frac{-t}{\tau}}}{\tau} P_a \tag{3.19}$$

where P_t is the probability that a charge is trapped in an avalanche (which is proportional to the overvoltage), τ is the trap lifetime and P_a is the probability that an avalanche is triggered (which is proportional to the overvoltage). Although $P_{afterpulse}(\Delta t)$ has a quadratic dependence on overvoltage, a way to allow higher operation overvoltage is to produce SiPM with a high purity silicon substrate, which significantly reduces the afterpulse noise.

Environmental factors: Ambient Light, Magnetic Fields and Temperature Effects

One of the key advantage of the silicon photomultipliers over the PMT is their insensitivity to magnetic fields. Since the electric field of the SiPM is very high and the thickness is very small, magnetic fields have a negligible effect on the device.

The ambient light (*e.g.* moon light) has a different effect on SiPM, compared to PMT. Feeble light saturates the silicon photomultipliers, but does not damage it, while it can degrade or destroy a PMT.

A major source of worry with SiPMs is their high temperature sensitivity, which is connected to two important parameters:

1. Breakdown voltage

2. Dark noise

In a pn-junction the breakdown voltage (V_{bd}) is proportional to the temperature T, with the formula:

$$\frac{\Delta V_{bd}}{\Delta T} = \eta \tag{3.20}$$

with η strongly related to material and doping of device. Therefore, in SiPMs at constant bias voltage a variation of temperature changes the overvoltage with effects on gain and efficiency of the device (eqn. 3.16). The dark noise is the other important parameter with a dependence on temperature. This sort of noise is due to thermal excitation which generates a free electron inside the SiPM depletion region; therefore an increase of temperature causes an exponential growth of dark noise (fig. 3.19a). There are essentially two ways to mitigate or eliminate the temperature sensitivity of SiPMs:

1. Bias voltage regulation

2. Temperature control

The bias voltage regulation (based on variations of breakdown voltage depending on temperature) is the simplest way to correct the effects of temperature on gain and overvoltage; however, it has no effect on dark noise. The other solution, temperature control, can eliminate the variation of breakdown voltage and mitigate the dark noise, however, it is the most expensive solution and not always feasible.

4

Silicon Photomultipler Characterization

4.1 Introduction to SiPM Characterization

The characterization of the detection components is an essential process in the design and production of a detector to achieve the desired performances, especially in those detectors or telescopes which plan to use silicon photomultipliers.

In last years many manufactures (e.g. Excelitas, FBK AdvanSiD, Hamamatsu Photonics, Ketek, SensL, ...) have developed silicon photomultipliers with different technologies and designs to optimize the performances of the devices in the different applications. A comparative characterization of silicon photomultipliers is an important step in the selection of perfect component for the desired detector.

Some operational performances and parameters of SiPMs show a sensitivity to external factors (*e.g.* voltage breakdown with temperature). The characterization of these devices and their performances in different circumstances is a crucial task for the design process of a detector.

Silicon photomultipliers with the same design and made from the same sili-

con slice have operational parameters slightly different or sometime anomalous behaviour. An automatic characterization permits to identify the operational parameters of each device and to reject the defective ones.

Silicon photomultipliers stand as a very promising technology, however, a characterization of the devices is an important step for their application. For this reason, the next paragraphs describe the five most used methods to characterize a silicon photomultiplier.

4.2 Single Photon Response Measurements

Silicon photomultipliers are high amplification devices which are capable of detecting single photons (fig.3.17). This paragraph describes the typical single photon response from silicon photomultipliers in terms of pulse shape and internal gain.

4.2.1 Pulse Shape

As highlighted in paragraph 3.2.2, a silicon photomultiplier is a high density matrix of GM-APD cells connected in parallel and the output signal is the sum of pulses from cells fired by photons. Therefore, the single photon response of a SiPM is the pulse of a GM-APD cell which depends on the design of the cell. Figure 4.1 shows the average pulse shape of different models of SiPMs. The pulse shape of a SiPM can influence its use, *i.e.* the rise time greatly affects the non-overlapping time of two different events (the tail of the pulse can be significantly reduced with a high pass filter and, for this reason, it has not a special role in the non-overlapping time of two different events).

4.2.2 Gain

The gain of a silicon photomultiplier is the internal amplification of the device expressed as the average number of charge carriers produced from a single

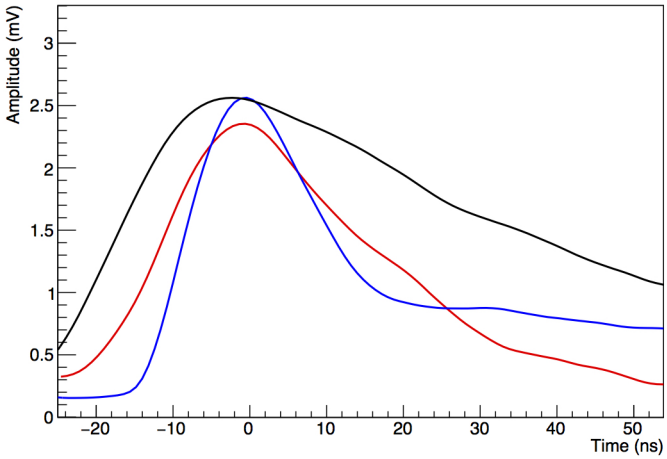

Figure 4.1: Average pulse shape from FBK Near Ultra Violet SiPM with a square cell pitch of 50 μm and 3x3 mm^2 area (blue line), Hamamatsu MPPC S13360-6050CS (black line) and S12572-015C (red line).

photoelectron (or thermal electron). The measure of the charge released by the SiPM could be used to obtain the gain through the formula:

$$Gain = \frac{Q}{G_{OpAmp} \times e} \tag{4.1}$$

where Q is the output charge from an operational amplifier connected in series with the SiPM, G_{OpAmp} is the internal gain of the amplifier and "e" is the electron charge.

As mentioned previously modelling each cell depleted region as a capacitor, the capacitance of the cell (C_{cell}) is linearly correlated with the bias voltage (V_{bias}) and the overvoltage (V_{over}) by:

$$C_{cell} = \frac{Gain \times e}{V_{bias} - V_{breakdown}} = \frac{Gain \times e}{V_{over}} = \frac{Q}{G_{OpAmp} \times V_{over}} \tag{4.2}$$

where $V_{breakdown}$ is the breakdown voltage of the device.

The gain of each cell defines the charge released when it is hit by a photon and the SiPM output is the sum of the charge emitted by the cells. The gain is an important parameter of SiPM because if it is well-known and the output charge is precisely measured, it is possible to calculate the number of incident photons. Many detectors can use this measure (number of incident photons) to estimate important information, for example Cherenkov telescopes can determinate the energy of the primary cosmic ray from the number of Cherenkov photons incident on telescope camera.

4.3 Temperature Dependence Measurements

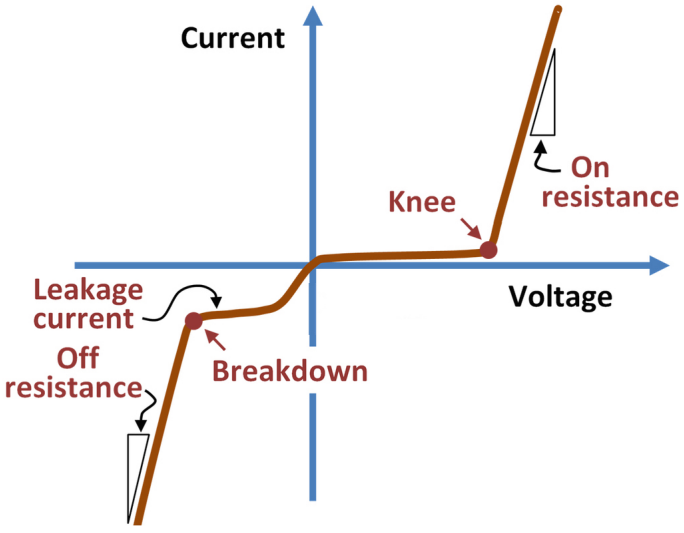

Figure 4.2: Current-voltage characteristic graph of a non-ideal p-n diode.

Silicon photomultipliers are electronic components with a significant sensitivity to temperature, which affects mainly the breakdown voltage and the resistance of the devices. Variations of these two parameters influence the SiPMs in many operational aspects (overvoltage, gain, pulse shape, ...) and for this reason they must be characterized at different temperatures to estimate their dependences on temperature.

Since a silicon photomultiplier works like a non-ideal p-n diode (fig.4.2), its breakdown voltage and resistance can be obtained with an accurate voltage current characterization, using the graph of the VI measurements.

4.3.1 Direct VI

In forward bias above the knee, a silicon photomultiplier operates like an electrical conductor with resistance R (fig.4.2) and the relationship between bias voltage (V), current (I) and resistance is expressed by the Ohm law:

$$V = R \times I \qquad \text{and} \qquad I = \frac{V}{R} \tag{4.3}$$

Therefore the slope of the current versus bias voltage curve can be used to derive the equivalent resistance of the silicon photomultiplier.

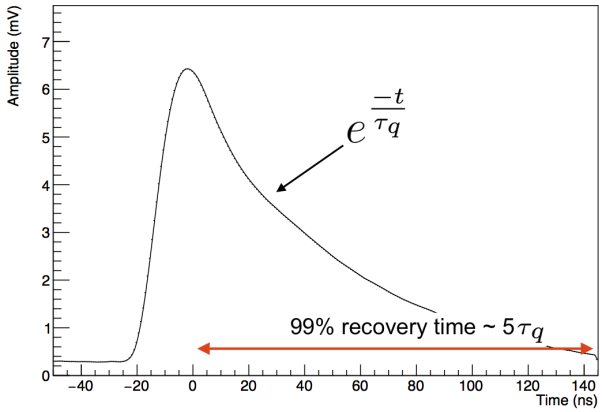

Figure 4.3: Typical GM-APD pulse from FBK Near Ultra Violet SiPM with a square cell pitch of 50 μm ($\tau_q = R_q C_d$).

In a silicon photomultiplier the resistance (R_q) quenches the avalanche of the device and influences the recharge of the SiPM's equivalent capacitance, therefore temperature variations of the resistance have effects on recovery

time and pulse shape. Figure 4.3 shows the influence of R_q in both these parameters, since $\tau_q = R_q C_d$ with C_q the equivalent capacitance of SiPM.

4.3.2 Reverse VI

At constant bias voltage, variations of breakdown voltage influence the overvoltage with effects on gain and pulse shape. Therefore, the dependece of $V_{breakdown}$ on temperature is an important parameter which can be estimated using VI measure in reverse bias.

Since a silicon photomultiplier works like a non-ideal p-n diode (fig.4.2), the breakdown voltage is usually obtained with an accurate reverse bias characterization using a fitting parametrization of the VI measurements. This study proposes an alternative way to evaluate the breakdown voltage using the graph curvature of VI measurements. Given any curve C and a point P on it, there is an unique circle which most closely approximates the curve near P, the "osculating" circle at P. The curvature of C at P is then defined to be the reciprocal of the osculating circle radius ($k = 1/R$), moreover, for the case of a plain curve, given explicitly as $y = f(x)$, it can be obtained the graph curvature (eqn.4.4). The current flowing into a SiPM is function of voltage $I = f(V)$, and using discrete derivates (eqn.4.5, 4.6, 4.7) one can obtain the graph curvature of reverse current characterization (eqn.4.8).

$$k = \frac{|y''|}{(1 + (y')^2)^{\frac{3}{2}}} \tag{4.4}$$

$$I'_i = \frac{I_{i-1} - I_i}{V_{i-1} - V_i} \tag{4.5}$$

$$I''_i = \frac{I'_{i-1} - I'_i}{V_{i-1} - V_i} \tag{4.6}$$

$$\overline{I'_i} = \frac{I'_{i-1} + I'_i}{2} \tag{4.7}$$

$$k_i = \frac{|I_i''|}{(1 + \overline{I_i'}^2)^{\frac{3}{2}}} \tag{4.8}$$

Figure 4.4a shows the reverse current as a function of voltage, while figure 4.4b shows the curvature as a function of voltage. The plots shows how the curvature can be used to obtain the breakdown voltage.

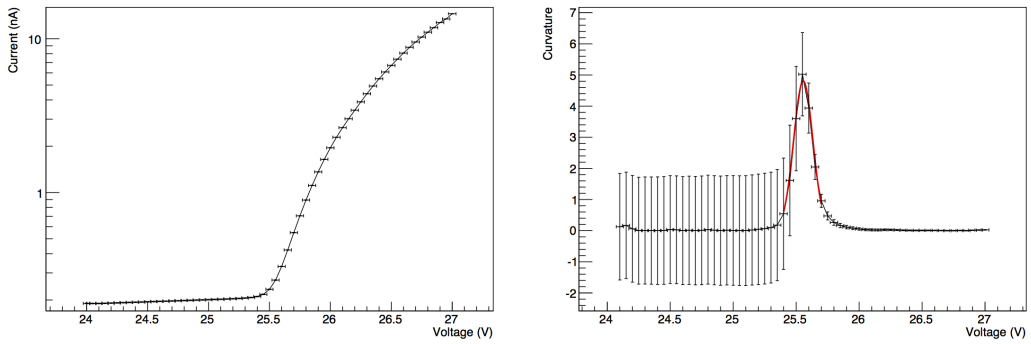

(a) (b)

Figure 4.4: Typical SiPM reverse bias VI graph (a) and its curvature with a Gaussian fit (b).

4.4 Light Efficiency Measurements

The photo detection efficiency (PDE) expresses the ability of a detector to convert an incident photon into a detectable output signal, which is the main function of a SiPM.

The standard method used to measure the PDE of a SiPM consists in a flashing light source with a narrow band filter (to set the wavelength), which illuminates both a calibrated reverse-biased PIN photodiode and a SiPM under test. In this setup, light uniformity is guaranteed by using an integrated sphere (fig.4.5). The mean digital counts obtained by the PIN diode $< DC_{PIN} >$ can be converted into the mean number of photon incident the SiPM with the formula:

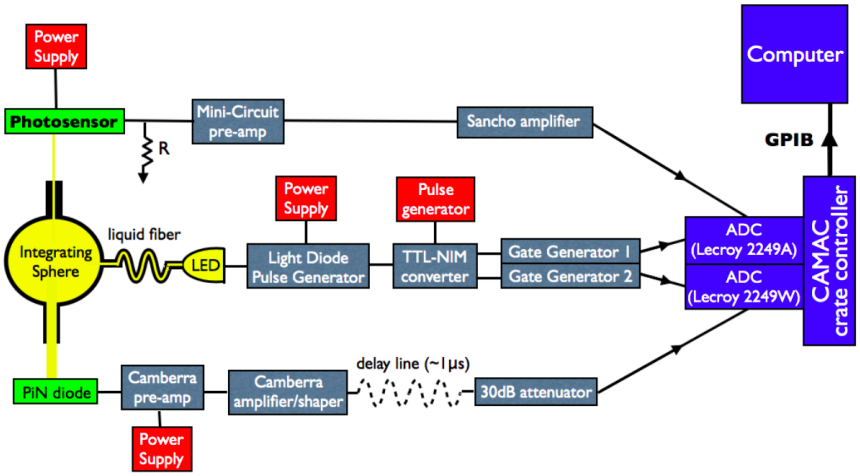

Figure 4.5: Setup used in [15] to measure the PDE of some photodetectors.

$$< N_{ph,incident} >= \frac{< DC_{PIN} > \times C_{DC=>PE}}{QE_{PIN}} \times R \tag{4.9}$$

where QE_{PIN} is the calibrated quantum efficiency of PIN diode, $C_{DC=>PE}$ is the conversion factor from PIN diode counts to photoelectrons and R is the ratio between the integrated sphere port point to SiPM and the port point to PIN diode. The average number of photons detected by SiPM can be obtained by an event distribution of the device under test, fixing a threshold at ~ 0.5 photoelectron level and defining some parameters:

- f_{dark}: dark noise frequency
- $< \Delta t >$: average time interval between two adjacent pulses
- $N_{tot,light}$: total number of events during a light run (with flashing light source on)
- $N_{0,true}$: true number of events with no photons detected during a light run
- $N_{0,light}$: number of events with no photons detectable during a light run.

The number of photons in a light pulse is expected to be Poisson distributed, therefore there are event in which exactly zero photons can been measured. The true number of events with no photons detectable is equal to:

$$N_{0,true} = N_{0,light} + (N_{0,true} \times f_{dark} \times < \Delta t >) \tag{4.10}$$

where $(N_{0,true} \times f_{dark} \times < \Delta t >)$ is the number of event generated by dark noise in a no detectable light pulse. Isolating $N_{0,true}$ the equation becomes:

$$N_{0,true} = \frac{N_{0,light}}{1 - (f_{dark} \times < \Delta t >)} \tag{4.11}$$

The probability to detect zero light photons (no dark noise) is:

$$P_0 = \frac{N_{0,true}}{N_{tot,light}} \tag{4.12}$$

but for a Poisson distribution with mean $< N_{ph,detected} >$, P_0 is also:

$$P_0 = e^{-<N_{ph,detected}>} \tag{4.13}$$

Combining equations 4.12 and 4.13, the average number of photon detected from the light source is:

$$< N_{ph,detected} >= -\ln\left(\frac{N_{0,true}}{N_{tot,light}}\right) \tag{4.14}$$

Finally the photo detection efficiency for a silicon photomultiplier is:

$$\text{PDE} = \frac{< N_{ph,detected} >}{< N_{ph,incident} >} \tag{4.15}$$

4.5 Noise Measurements

In silicon photomultipliers the noise is one of the major source of concern; it influences many aspects of a device and its use. Moreover, since the dark noise

increase exponentially with the temperature, it can influence the operational temperature of the device.

4.5.1 Dark Noise

As mentioned previously the dark noise is caused by thermal-generated electrons inside the depletion zone which produce avalanches and pulses (dark pulses) indistinguishable from photon-generated pulses. It is exponentially proportional to temperature and an ineradicable source of noise in silicon photomultiplier.

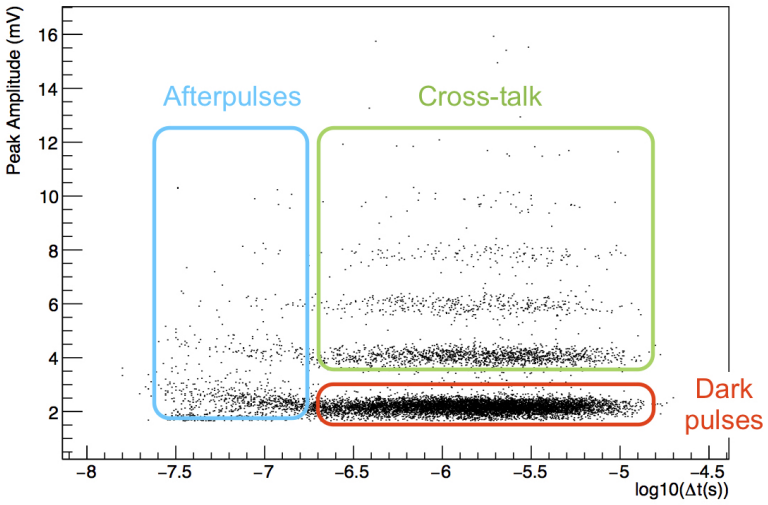

Figure 4.6: Typical scatter plot of noise events for a SiPM. Each point in the plot is the amplitude of an event as a function of its distance from the preceding one.

The standard setup used for dark noise characterization consists in a dark box containing the silicon photomultiplier and connected to an amplification stage, both inserted in a climate chamber. The amplifier output signal is acquired by a digital oscilloscope which sends the data to an acquisition computer for analysis. The oscilloscope is usually set to acquire long waveforms,

so the time interval between two noise event and their amplitude can be estimated with a pulse identification program. These two data include all of the relevant information regarding the noise of the device. Figure 4.6 shows a typical scatter plot of noise pulses for a silicon photomultiplier, each point in the plot is the amplitude of a pulse as a function of its time distance (Δt) from the preceding event. The dots in the red frame are dark pulses.

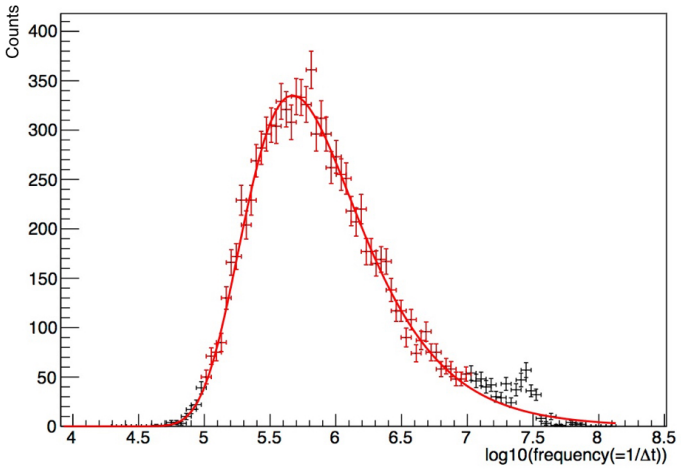

Figure 4.7: Typical inverse time distance distribution of noise events ($1/\Delta t$) for a silicon photomultiplier in a dark box. The red line is the Poissonian fit of distribution.

In the characterization of dark noise, the main parameter to identify is the frequency of thermal photons (a.k.a. *dark noise frequency*), which generate the dark pulses in the silicon photomultiplier. In this work the dark noise frequency has been estimated by the distribution of inverse time distance between two adjacent dark pulses ($1/\Delta t$). Figure 4.7 shows a typical inverse time distance distribution of noise events ($1/\Delta t$) for a silicon photomultiplier in a dark box, the red line is the Poissonian fit of distribution.

4.5.2 Cross-talk

The Cross-talk noise is generated by photons produced by cell avalanches which trigger secondary avalanches in the surrounding cells, therefore the output pulse will be the sum of the avalanches. Figure 4.8 shows a cross-talk pulse compared with a regular pulse without noise, while the cross-talk events in figure 4.6 are the clouds of dots in green frame. The cross-talk can be an important source of noise because it can amplify the effects of the naturally noisy environment (e.g. night sky background for IACT) hence it is a parameter to be characterized.

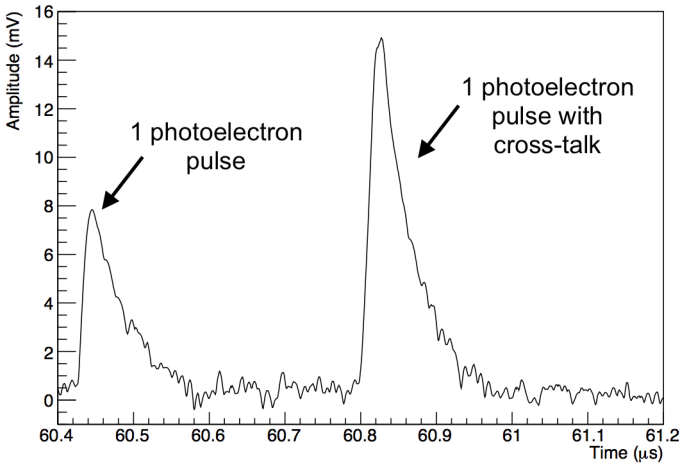

Figure 4.8: Cross-talk noise.

In the characterization of cross-talk, the main parameter to identify is the cross-talk probability ($P_{crosstalk}$) which is the probability that a cross-talk event happens. As mention previously the $P_{crosstalk}$ can be easily obtained from SiPM pulse amplitude distribution or noise events graph as a function of the discriminator threshold (fig. 4.9):

$$P_{crosstalk} = \frac{N_{>1.5pe}}{N_{>0.5pe}} \tag{4.16}$$

where $N_{>0.5pe}$ and $N_{>1.5pe}$ are the number of pulse exceeding the 0.5 and 1.5 levels of the single cell amplitude.

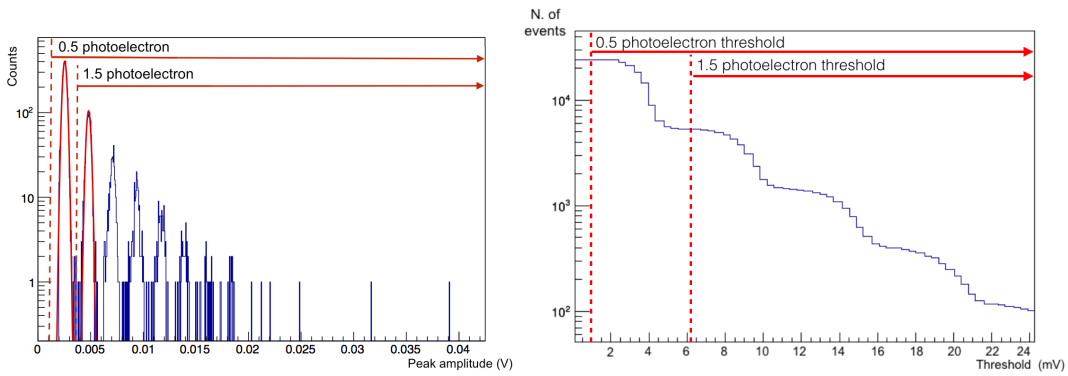

(a) (b)

Figure 4.9: Typical pulse amplitude distribution of silicon photomultipliers (a) and number of noise events as a function of the discriminator threshold (b).

An alternative way to estimate the cross-talk is to fit the first and the second peak of the pulse amplitude distribution with two fit functions $f_1(V)$ and $f_2(V)$ respectively. The ratio between noise events with single cross-talk and events without cross-talk is therefore:

$$R_{\frac{crosstalk}{noise\ event}} = \frac{\int_0^\infty f_2(V)dV}{\int_0^\infty f_1(V)dV} \tag{4.17}$$

4.5.3 Afterpulse

The afterpulse noise is due to avalanche-generated carriers which have been trapped by silicon impurities and later released. When a carrier is released, it triggers a new avalanche which changes the charge and the shape of the output pulse (fig.3.20) making afterpulse an important parameter to characterize. This type of noise is usually estimated by the afterpulse probability which can be characterized by noise frequency ($1/\Delta t$) distribution (fig.4.10). The

afterpulse probability ($P_{afterpulse}$) is therefore calculated as the ratio between the counts in excess of dark noise fit, in the afterpulse bump, and the total events.

$$P_{afterpulse} = \frac{Afterpulse\ events}{Total\ events} \tag{4.18}$$

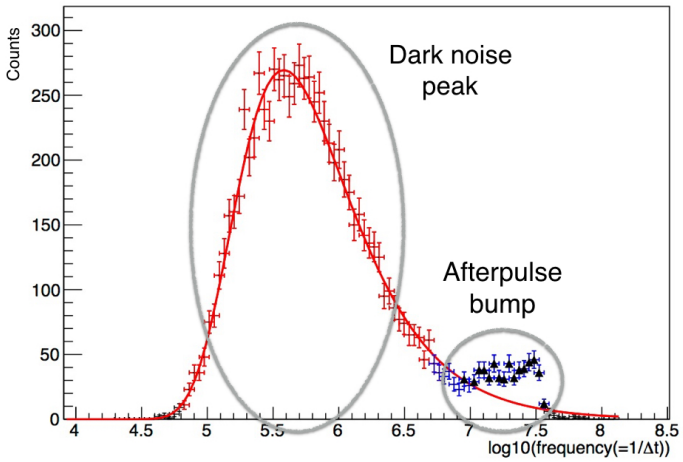

Figure 4.10: Noise frequency ($1/\Delta t$) distribution with afterpulse bump.

4.6 Aging

In silicon photomultipliers the performance degradation is still not a well-evaluated parameter. The resistance to intense luminosity is particularly important for Cherenkov telescopes which can be subject to bright moonlight periods. In aging characterization a silicon photomultiplier is usually illuminated for a periond of time equivalent to 35 years of telescope's operation to estimate the degradation of its performances. The process is regularly interrupted to measure the features of the device as well as two reference SiPMs that are not being aged.

5

Comparative Investigation

5.1 Experimental Set-up and Acquisition

Silicon photomultiplier characterization is a fundamental task for these devices that has a strong impact on many aspects: design, manufacturing technology definition, selection, use and so on. Moreover, the silicon photomultiplier technology is a promising candidate for replacing the current photomultipliers in a large number of applications and there are several companies that produce SiPMs with different characteristics. Therefore a semi-automatic test rig has been designed and assembled to support a comparative investigation of these devices at different temperature conditions.

5.1.1 Experimental Set-up

The hardware set-up used for characterization is shown in figure 5.1 and it consists of several elements:

- **Climate chamber:** It is an Angelantoni climate chamber model EOS 100 T, with an adjustable temperature between -40 °C and 180 °C. It contains the silicon photomultipliers under test and some other components of the setup.

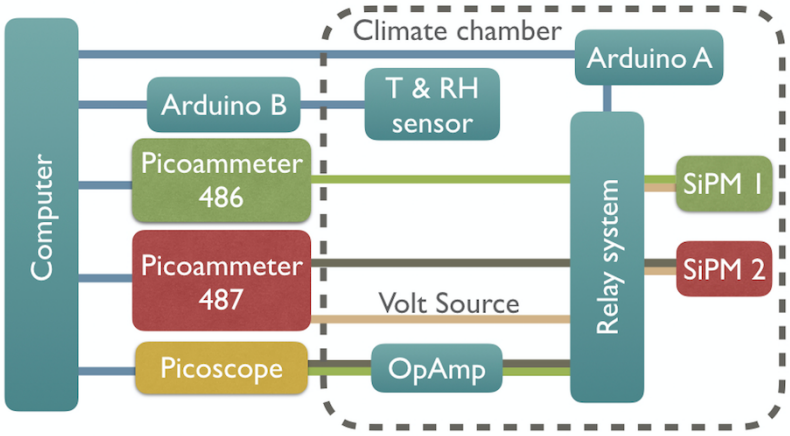

Figure 5.1: The hardware setup used in the comparative investigation of silicon photomultipliers.

- **Operational amplifier:** It is a wide-band amplifier HFAH-20, with a gain of 20 dB and a cut-off frequency of 2.9 GHz. It is placed inside the climate chamber and it amplifies the noise signal from SiPM under test.

- **Temperature and relative humidity sensor:** it is a Sensirion SHT15 temperature and relative humidity sensor mounted on a Sparkfun PCB and controlled by an arduino UNO board (Arduino B). It is placed inside the climate chamber very close to the detector under test (DUT).

- **Relay system:** It is a relay matrix, especially designed for the test rig and controlled by the computer through an arduino UNO board (Arduino A). Figure 5.2 shows the schematic of the relay system, the A-part controls the bias of the two SiPMs, while the B-part redirects their output of the two SiPMs.

- **Arduino A:** It is an arduino UNO board controlled by the computer through a labview program and a software loaded on the board. The arduino

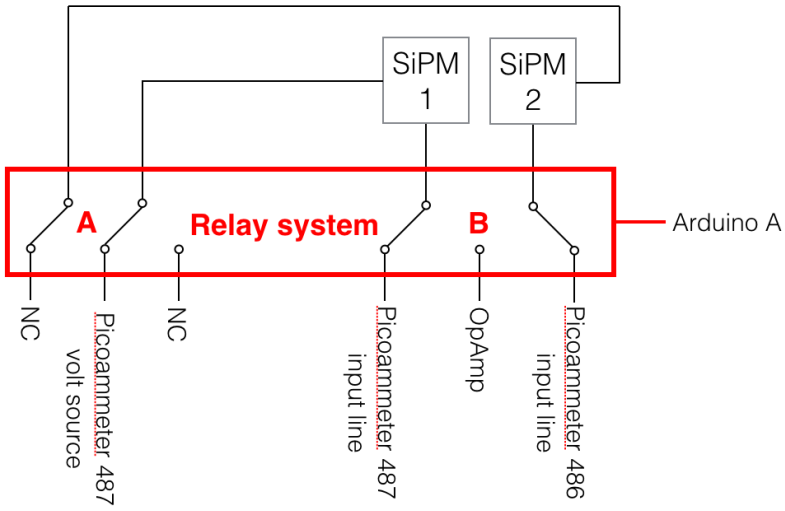

Figure 5.2: Relay system.

uses its digital pins to control the relays and therefore the bias and the output of silicon photomultiplier.

- **Arduino B:** It is an arduino UNO board connected with the computer via USB cable. A Wiring program inside the board controls the sensor and sends the temperature measurement to the computer via serial port. In this case the computer does not control the board, it just receives the data from the arduino.

- **Picoammeter 486:** It is a Keithley picoammeter model 486 with an input current range from -2 mA to 2 mA. It is controlled by computer through a labview program designed for the test rig and via GPIB bus.

- **Picoammeter 487:** It is a Keithley picoammeter model 487 with an input current range from -2 mA to 2 mA and a volt source selectable from -500 V to 500 V. It is controlled by computer through a labview program designed for the test rig and via GPIB bus.

- **Picoscope:** It is a Pico Technology PicoScope model 6403C controlled by the computer via USB connection and through a labview program modified for the test rig.
- **Labview VIs:** Six Labview programs are in charge of the acquisition process, expressly designed for the test rig. Two VIs have been created for the voltage-current characterization, two for controlling the relay system, one for the temperature and relative humidity sensor while the last one is designed for signal acquisition.

5.1.2 The Acquisition Process

The acquisition process is a sequence of cycles at different temperatures, each one divided in three stage: temperature setting, voltage-current acquisition and oscilloscope acquisition. Figure 5.3 shows a schematic cycle: when a cycle ends, a new cycle starts with a different temperature. In this work the whole acquisition process is made by five cycles at the temperature: -10 °C, 0 °C, 10 °C, 20 °C and 30 °C.

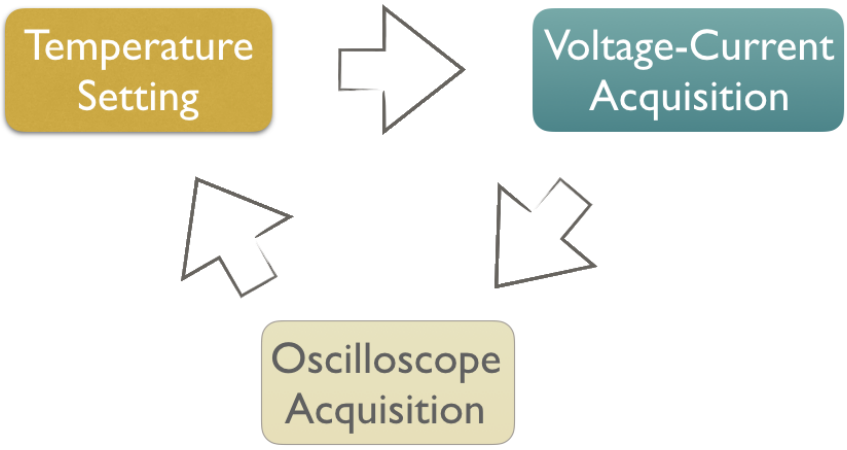

Figure 5.3: An acquisition cycle.

Temperature Setting

Once the silicon photomultipliers under test have been placed in the test rig, the first step is setting the climate chamber temperature and waiting for its stabilization; this phase usually requires about one hour. The VI of temperature sensors displays the temperature near the SiPM (fig.5.4).

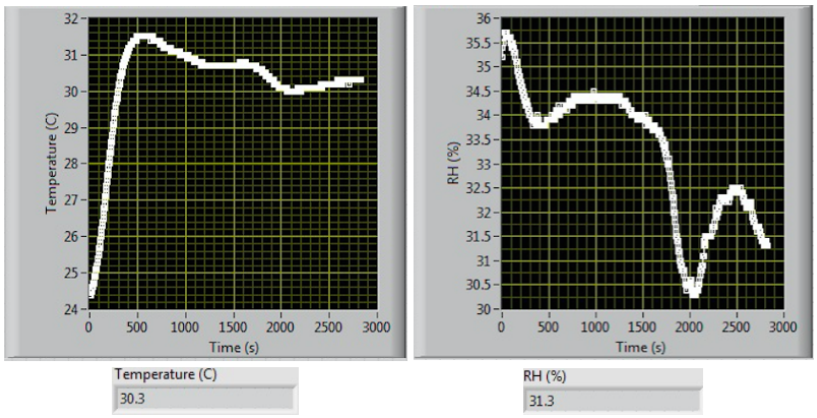

Figure 5.4: Labview VI of temperature sensor.

Voltage-Current Acquisition

When the temperature inside the climatic chamber is stable, the next step is the voltage-current acquisition. Using the VI designed for the relay system it is possible to evaluate the SiPMs in both sequence or parallel mode; the latter case is time saving, however it could be selected only when the voltage sweep of two devices has the same range since the voltage source supplies both SiPMs simultaneously. Once the mode is set, a sequence of two VIs , one in direct bias and one in reverse bias, measures the current flowing through the silicon photomultipliers in a voltages sweep using the two picoammeters (fig.5.5).

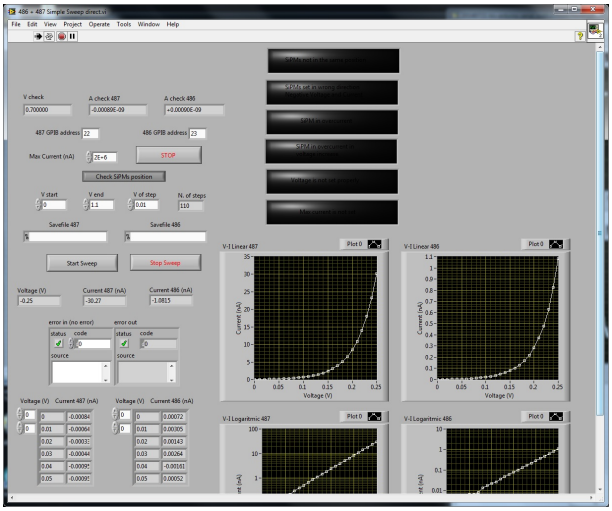

Figure 5.5: Labview VI for reverse current characterization.

Oscilloscope Acquisition

Once the voltage-current acquisition is completed, the oscilloscope acquisition, which is the last cycle step, is performed. After the relay system is set, a large amount of long waveforms are acquired in sequence from the two device under test. Figure 5.6 shows the labview VI for the oscilloscope acquisition. When acquisition ends, a new cycle start from the temperature setting stage with a different temperature.

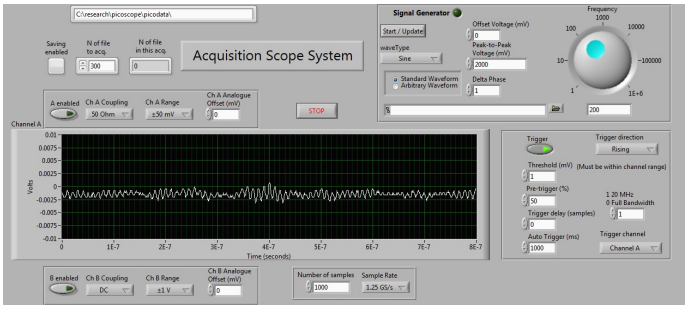

Figure 5.6: Labview VI for oscilloscope acquisition.

5.2 Temperature Dependence Measurements

The data obtained from voltage-current acquisition are subsequently analysed off-line by programs, which have been expressly designed for VI characterization.

5.2.1 Direct VI Measurements and Data Analysis

As mentioned previously in forward bias and after the knee, a silicon photomultiplier operates like an electrical conductor with resistance R, therefore, the slope of the voltage current graph can be used to derive the equivalent resistance of the silicon photomultiplier.

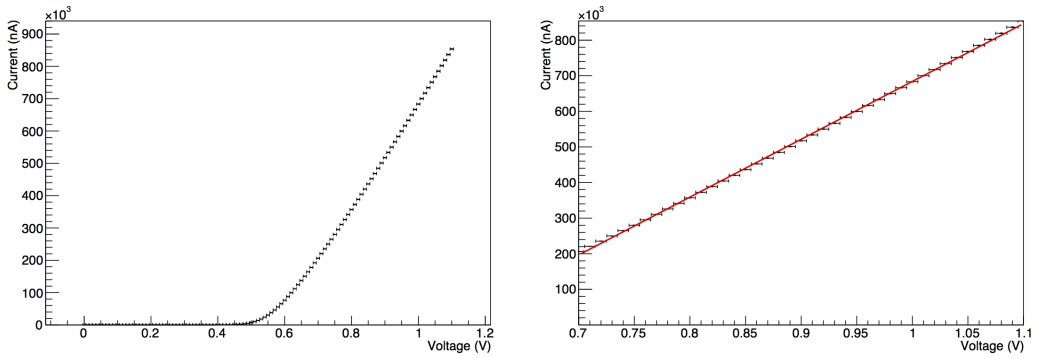

(a) (b)

Figure 5.7: Direct voltage-current characterization (a) with linear fit after the knee (b).

Figures 5.7 shows a VI graph of a silicon photomultiplier in forward bias at constant temperature with linear fit after the knee. With the resistances obtained at the five temperature, one can plot the variation of resistance of SiPM as a function of temperature (fig.5.8).

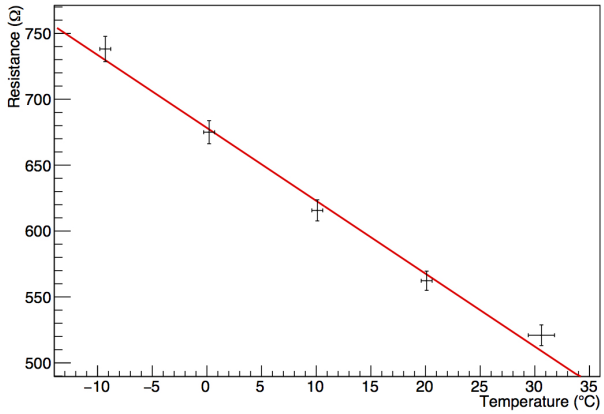

Figure 5.8: Typical variation of silicon photomultiplier's resistance as a function of temperature.

5.2.2 Reverse VI Measurements and Data analysis

From VI characterization of a silicon photomultiplier in reverse bias, it is possible to define the voltage breakdown of the device at the set temperature. However, the data obtained from acquisition are too noisy, therefore data processing is necessary to proceed with the analysis. Figure 5.9 shows the results of a SNIP algorithm ([17] and [18]), which is an unusual procedure for this type of data but it gives excellent results.

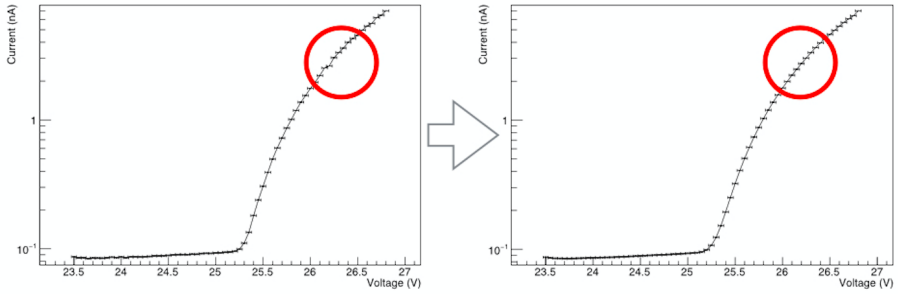

Figure 5.9: A SNIP algorithm applied to voltage current data of a silicon photomultiplier in reverse bias.

From the processed data, one can obtain the breakdown voltage of the silicon photomultiplier at the set temperature. Figure 5.10 shows the results of ROOT program, which has been designed to find the breakdown voltage.

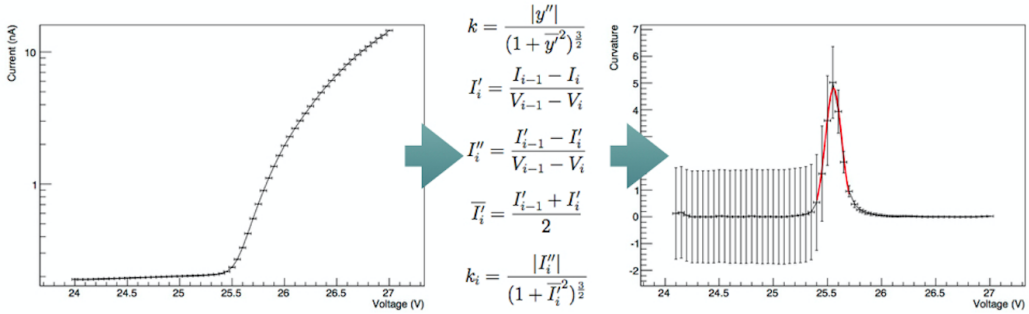

Figure 5.10: The curvature (right graph) obtained from reverse current characterization (left graph). The red line is the fit curve of the curvature.

.

The breakdown voltages of SiPM at the different temperatures can be used to derive its variation as a function of the temperature (fig.5.11).

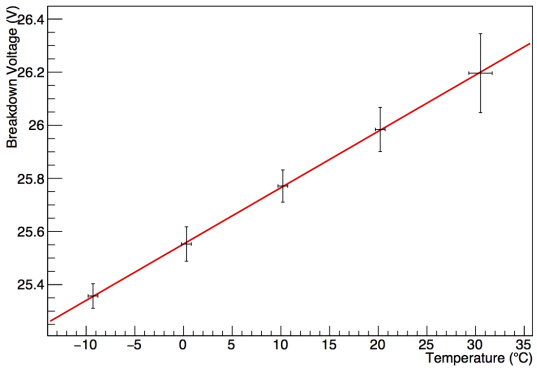

Figure 5.11: Variation of the breakdown voltage as a function of temperature.

5.3 Noise Measurements

In the last phase of the acquisition cycle, the oscilloscope collects waveforms, which usually show undershooting and offsets, therefore the data must be processed to eliminate these irregularities before they can be used for a noise characterization. Figure 5.12 shows a waveform before and after the action of ROOT program designed to find and eliminate the background from a waveform with a SNIP algorithm ([17] and [18]).

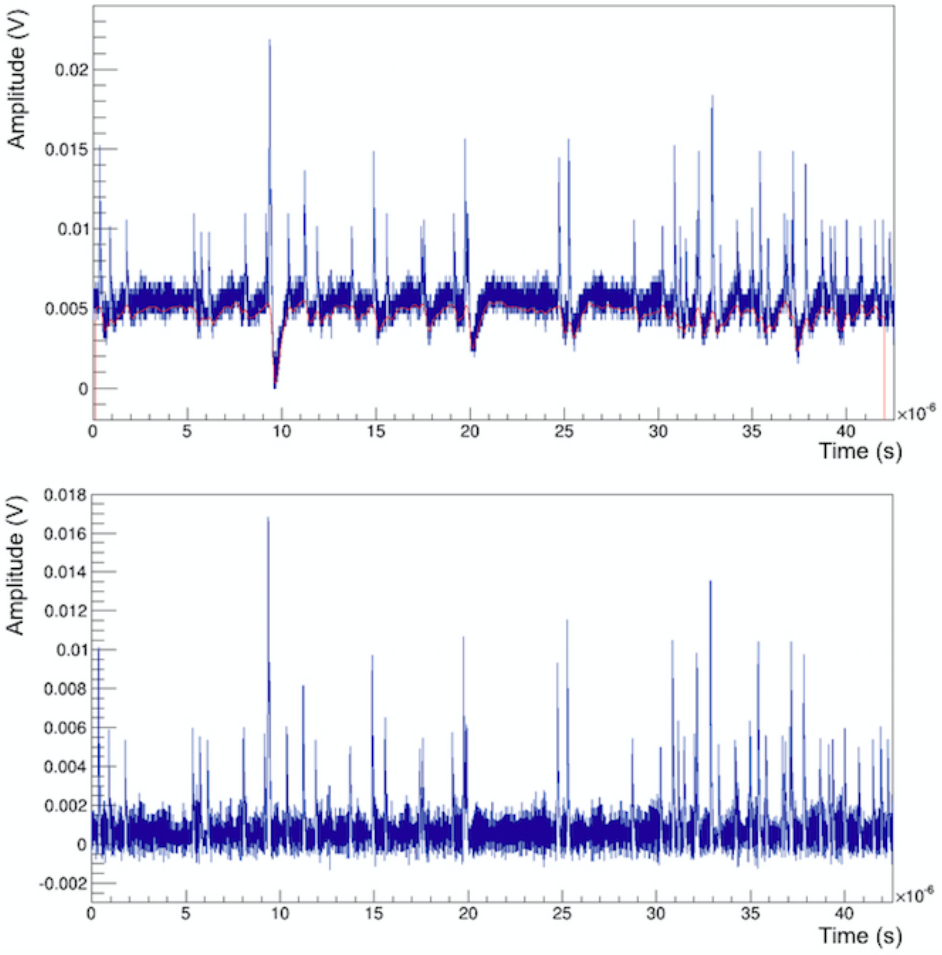

Figure 5.12: The same waveform before and after a ROOT program designed to find and eliminate the background with a SNIP algorithm.

From the processed waveforms, the time stamps of the noise events and their amplitude can be estimated with a program which has been designed to identify peaks in the waveforms. This algorithm uses two thresholds to open and close a gate and inside this zone the program searches for peaks. In this way it is possible define the first peak (probably dark pulses) and the secondary ones (probably afterpulses) and assign a flag to each peak. Figure 5.13 shows a couple of peaks identified with this technique.

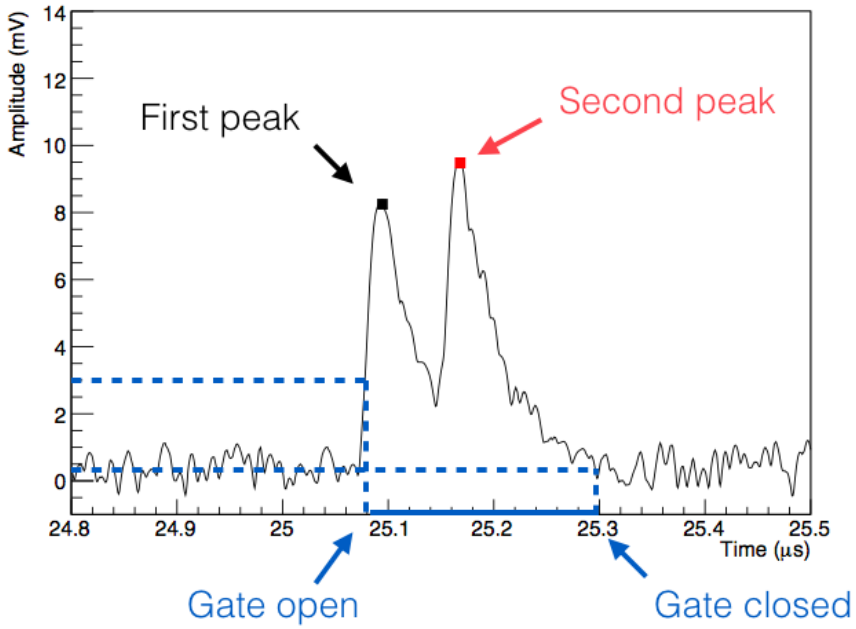

Figure 5.13: Peaks identified with a two-threshold technique.

From the output of the pulse identification algorithm, one can obtain the scatter plot shown in figure 5.14, where each point is the amplitude of a pulse as a function of its time distance (Δt) from the preceding event. Each type of noise is well-identifiable in the plot, dark noise in the red frame, cross-talk in the green frame and afterpulses in the blue frame.

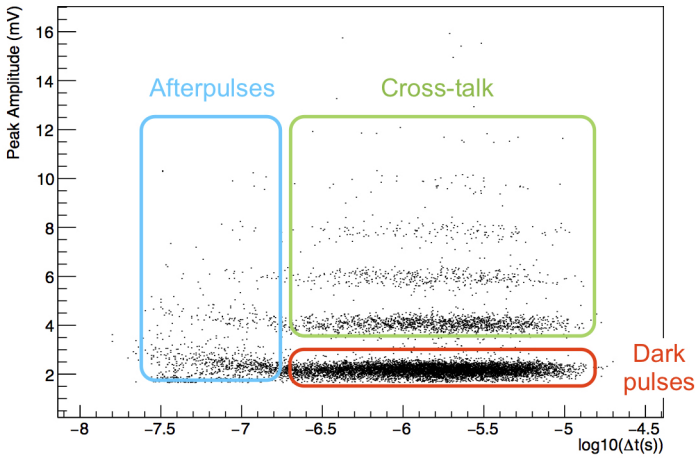

Figure 5.14: Typical scatter plot of noise events for a SiPM. Each point in the plot is the amplitude of an event as a function of its distance from the preceding one.

5.3.1 Dark Noise Measurements and Data Analysis

In the dark noise characterization the main purpose of data analysis is to discover the dark noise rate (a.k.a. dark noise frequency) of the silicon photomultiplier, which is the mean number of dark pulses per time. This important parameter can be estimated from the time stamps of the noise events with the inverse time distance ($1/\Delta t$). From the output of the pulse identification algorithm, a program can associate each event with its time distance (Δt) from the previous pulse (fig.5.15a). With the time distances (Δt) of all dark pulses, one can fill a histogram of inverse time distances ($1/\Delta t$). Figure 5.15b shows the inverse time distance histogram fitted with the function:

$$f(x) = P_0(e^{-10^{((x-\frac{P_2}{2})-Mean)}} - e^{-10^{((x+\frac{P_2}{2})-Mean)}}). \tag{5.1}$$

where P_2 is the size of histogram bins and mean is the mean value of the dark noise frequency.

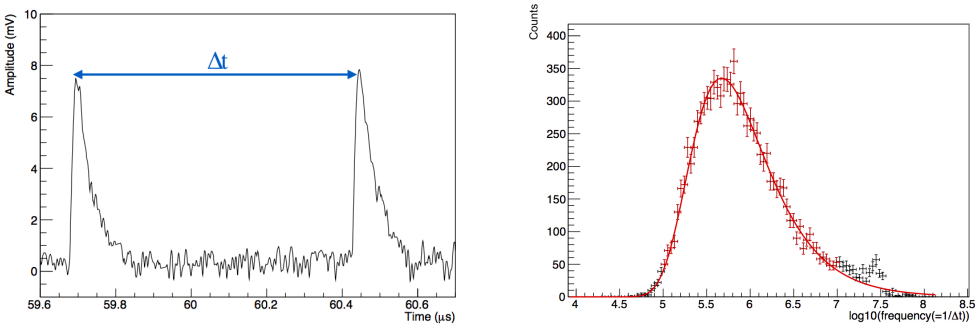

(a) (b)

Figure 5.15: Left frame is the time distance Δt between two dark pulses, while the right frame is the histogram of time inverse distances $(1/\Delta t)$ fitted with function 5.1

Figure 5.16a shows the dark noise frequencies as a function of temperature at different overvoltages, with exponential fit functions, while figure 5.16b shows the dark noise frequencies as a function of overvoltage at different temperatures, with linear fit functions. The data of both plots are obtained by the fits of time inverse distance distribution.

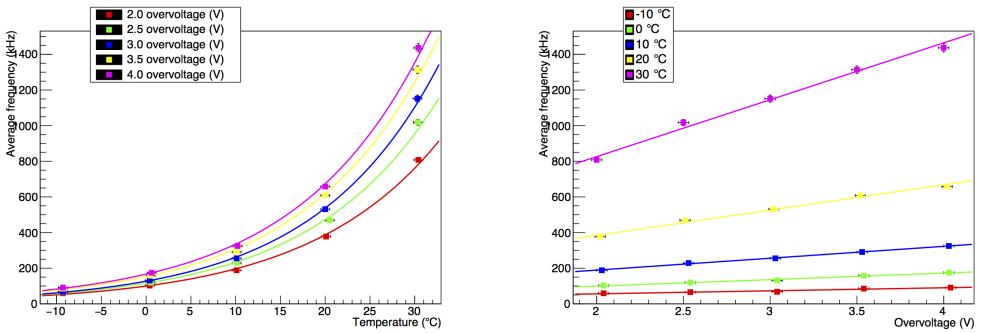

(a) (b)

Figure 5.16: The left plot is the dark noise frequencies as a function of temperature, while the right plot is the dark noise frequencies as a function of overvoltage

5.3.2 Cross-talk Measurements and Data Analysis

In silicon photomultiplier the cross-talk noise is caused by infrared photons from an original avalanche which trigger a secondary avalanche in a different cell. The probability for this to happen is an important parameter for silicon photomultipliers which can be estimated from the amplitudes of the noise events. From the output of the pulse identification algorithm one can fill a histogram with the amplitude of the noise events obtaining the amplitude distribution shown in figure 5.17

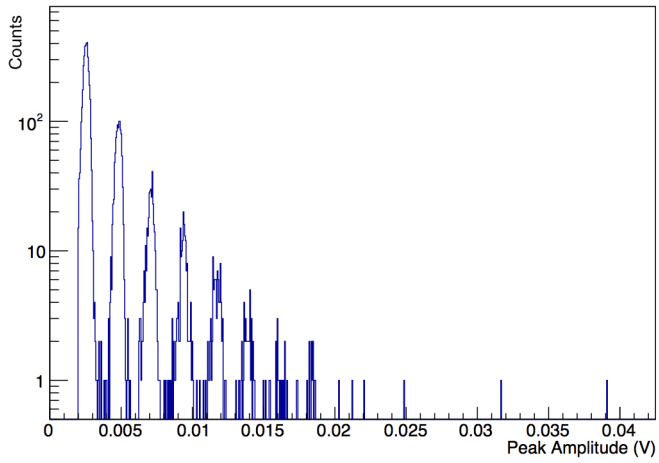

Figure 5.17: Amplitude distribution of noise events.

From the amplitude distribution one way to estimate the cross-talk noise is to use some thresholds to define the noise events with zero, one or more secondary avalanches which correspond to events with no cross-talk, single cross-talk or more cross-talk, respectively (fig.5.18). Combining these values with the total number of pulse exceeding the 0.5 level of the single cell amplitude one can obtain:

$$P_{no\ cross-talk} = \frac{N_{no\ cross-talk}}{N_{>0.5pe}} \tag{5.2}$$

$$P_{single\ cross-talk} = \frac{N_{single\ cross-talk}}{N_{>0.5pe}} \tag{5.3}$$

$$P_{multi\ cross-talk} = \frac{N_{multi\ cross-talk}}{N_{>0.5pe}} \tag{5.4}$$

where $P_{no\ cross-talk}$ is the probability of noise events without cross-talk, $P_{single\ cross-talk}$ is the probability of noise events with only one secondary avalanche, $P_{multi\ cross-talk}$ is the probability of noise events with more than one secondary avalanche and $N_{>0.5pe}$ is the total number of pulse exceeding the 0.5 level of the single cell amplitude.

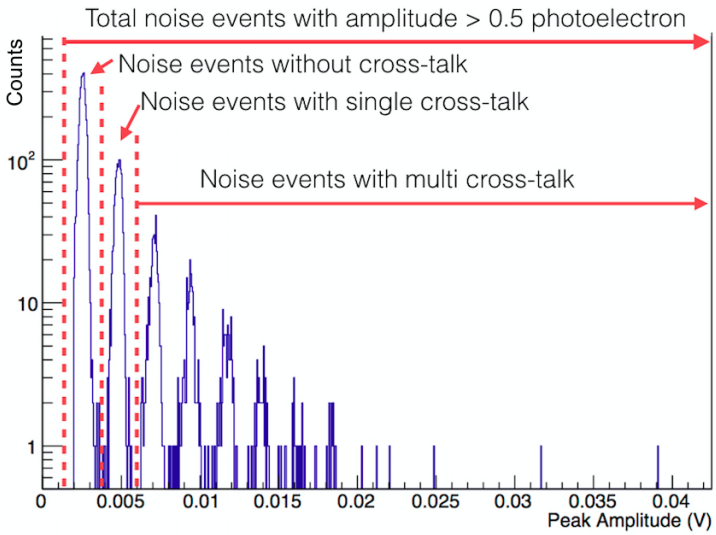

Figure 5.18: Some typical thresholds used for cross-talk characterization.

Figures 5.19, 5.20 and 5.21 show some typical $P_{no\ cross-talk}$, $P_{single\ cross-talk}$ and $P_{multi\ cross-talk}$, respectively as a function of temperature at different overvoltages, while figures 5.22, 5.23 and 5.24 show $P_{no\ cross-talk}$, $P_{single\ cross-talk}$ and $P_{multi\ cross-talk}$, respectively as a function of overvoltage at different temperatures.

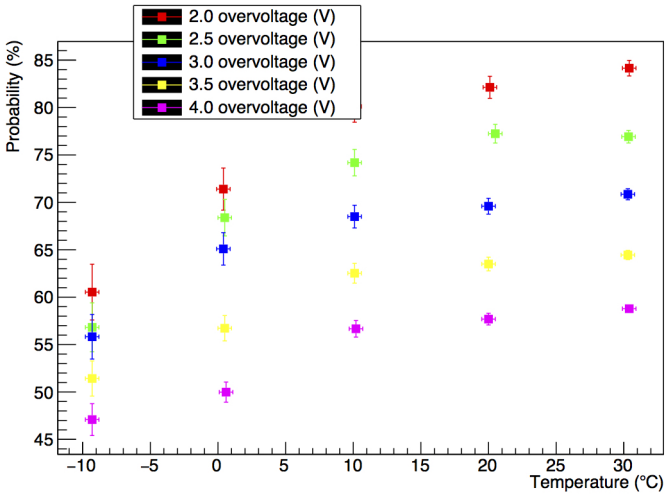

Figure 5.19: Probabilities to have noise events without cross-talk as a function of temperature at different overvoltages.

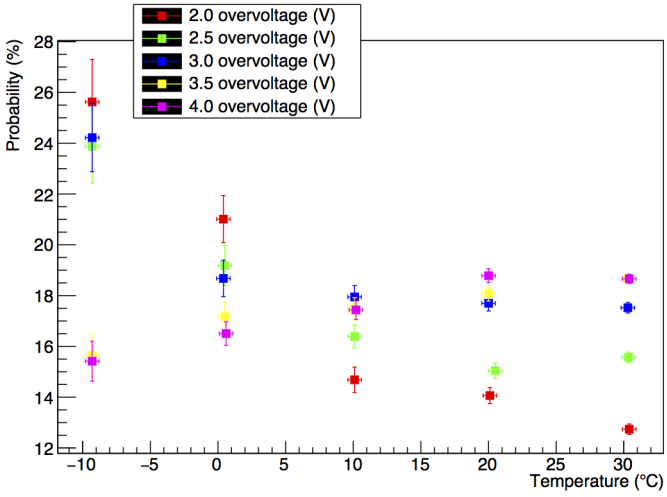

Figure 5.20: Probabilities to have noise events with only one secondary avalanche as a function of overvoltage at different overvoltages.

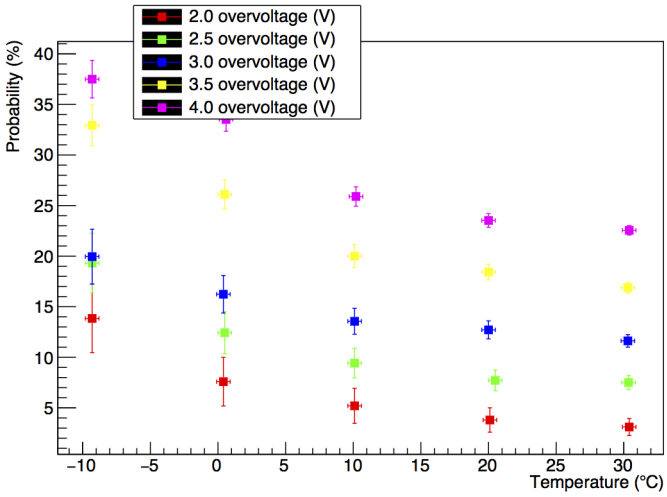

Figure 5.21: Probabilities to have noise events with more than one secondary avalanche as a function of overvoltage at different overvoltages.

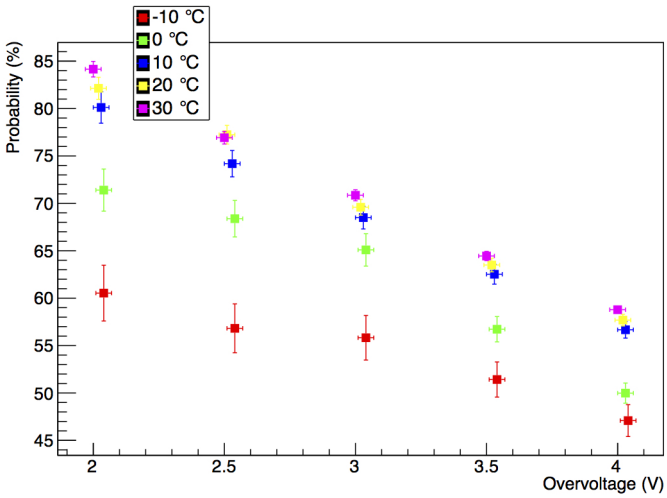

Figure 5.22: Probabilities to have noise events without cross-talk as a function of overvoltage at different temperatures.

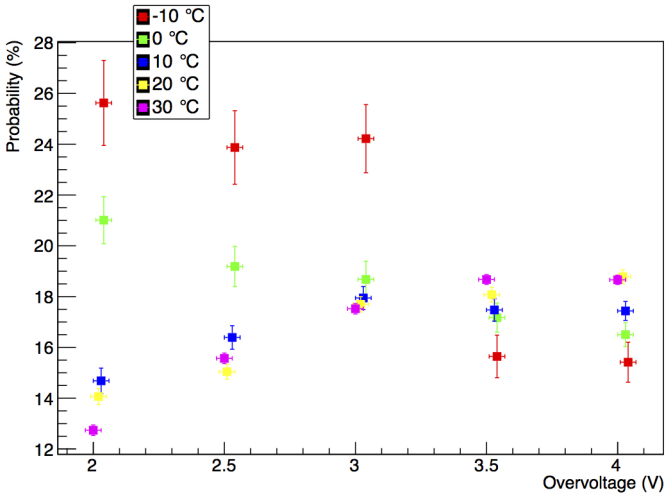

Figure 5.23: Probabilities to have noise events with only one secondary avalanche as a function of temperature at different temperatures.

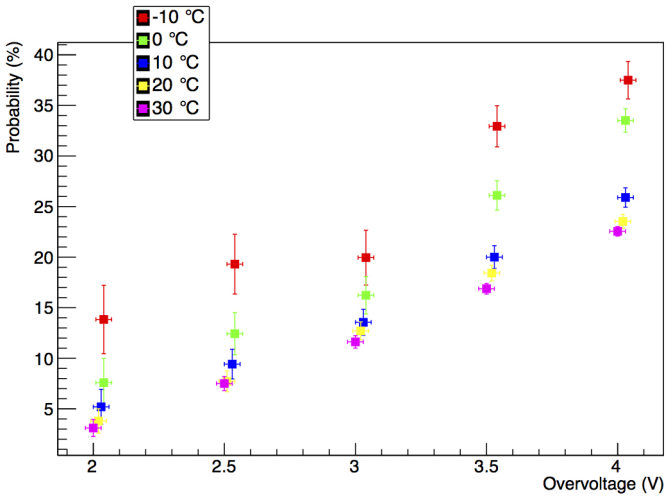

Figure 5.24: Probabilities to have noise events with more than one secondary avalanche as a function of temperature at different temperatures.

As mentioned previously, an alternative way to estimate the cross-talk is to fit the first and the second peak of the pulse amplitude distribution with two Gaussian functions $f_1(V)$ and $f_2(V)$, respectively (fig.5.25a). The ratio between noise events with single cross-talk and events without cross-talk is therefore:

$$R_{\frac{crosstalk}{noise\ event}} = \frac{\int_0^\infty f_2(V)dV}{\int_0^\infty f_1(V)dV} \tag{5.5}$$

Figure 5.25b shows some typical ratios between noise events with single cross-talk (DiCT(2pe)) and events without cross-talk (DP(1pe)) as a function of temperature.

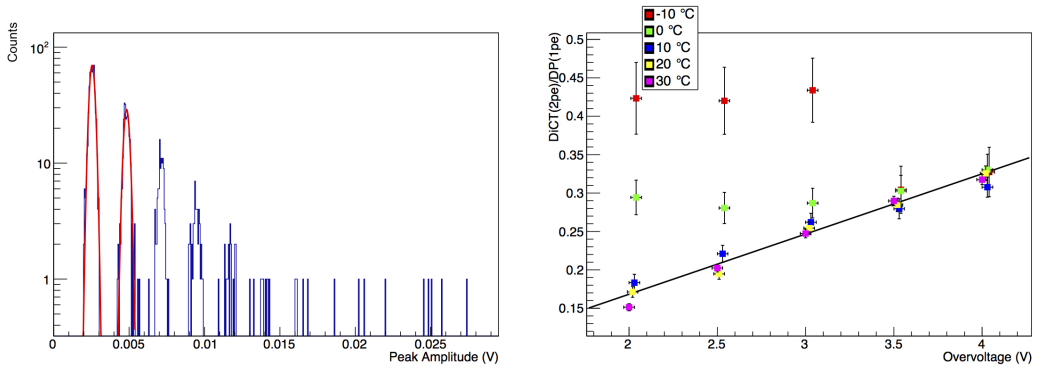

(a) (b)

Figure 5.25: The left plot is the amplitude distribution of noise events fitted with two Gaussian functions, while some typical ratio between noise events with single cross-talk (DiCT(2pe)) and events without cross-talk (DP(1pe)) are plotted as a function of overvoltage in the right frame, the black line is a possible linear fit function of the ratios.

5.3.3 Afterpulse Measurements and Data Analysis

The afterpulse is a type of noise due to avalanche-generated carriers which have been trapped by silicon impurities and later released. The characterization of

this noise starts from the same inverse time distribution used to derive the *dark noise frequency*. Figure 5.26 shows a typical inverse time distribution, the red line in the figure is the fit function of dark noise, while the bump in the ring can be ascribed to afterpulse noise. The probability of afterpulse noise occuring (a.k.a. afterpulse probability or afterpulse ratio) is, therefore, the ratio between the counts in excess of Poissonian fit in the bump (afterpulse events) and the integral of fit function $f(\psi = 1/\Delta t)$:

$$P_{afterpulse} = \frac{(\Sigma\, ap)}{\int_0^\infty f(\psi) d\psi} \tag{5.6}$$

where $P_{afterpulse}$ is the afterpulse probability and $(\Sigma\, ap)$ is the sum of all afterpulse events.

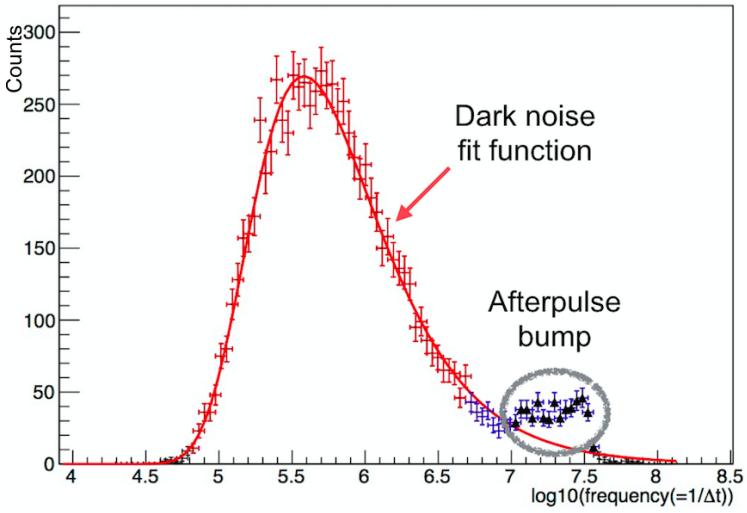

Figure 5.26: A typical inverse time distribution with afterpulse bump.

Figure 5.27a shows the afterpulse probability of a silicon photomultiplier as a function of temperature at different overvoltages while figure 5.27b shows the afterpulse probability as a function of overvoltage at different temperatures. The data of both plots are obtained from the afterpulse bumps of the inverse time distributions.

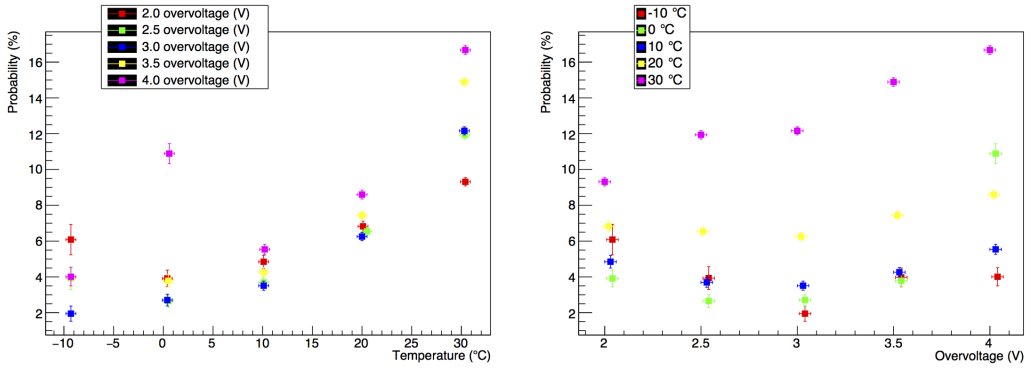

(a) (b)

Figure 5.27: The left plot shows the afterpulse probability of a silicon photomultiplier as a function of temperature at different overvoltages while the right plot shows the afterpulse probability as a function of overvoltage at different temperatures.

An alternative way to determinate the afterpulse events is to use the flags set by pulse identification algorithm. As previously stated, this algorithm set a flag for each peak identified, if the peak is a first peak then the flag is 0, otherwise it is 1. Since the pulses with flag 1 are probably afterpulse, the alternative afterpulse probability ($P_{alternative\ AP}$) is the ratio between these events and the pulse with flag 0:

$$P_{alternative\ AP} = \frac{\Sigma\, Peak_1}{\Sigma\, Peak_0} \tag{5.7}$$

where $\Sigma\, Peak_0$ and $\Sigma\, Peak_1$ are the sums of peaks with flag 0 and 1, respectively.

Figure 5.28 shows this alternative afterpulse probability of a silicon photomultiplier as a function of overvoltage at different temperatures.

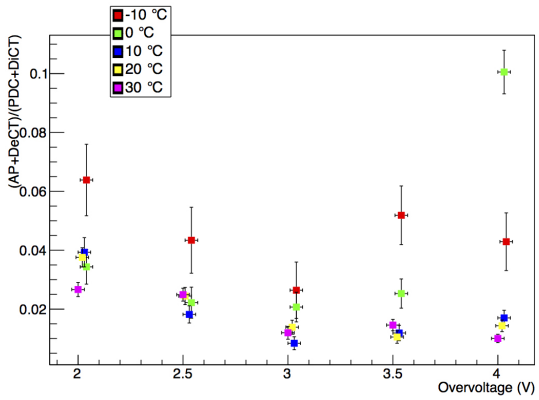

Figure 5.28: Some typical ratio between noise events with flag 1 (AP+DeCT) and with flag 0 (PDC+DiCT).

5.4 Single Photon Response Measurements

In the characterization of a silicon photomultiplier there are many possible ways to estimate its single photo response. In this work the pulse shape and the gain of a SiPM have been evaluated from the same waveforms used for noise characterization, and applying the same pulse identification algorithm.

5.4.1 Pulse Shape Results and Data Analysis

A silicon photomultiplier avalanche triggered by a single photon (or thermal excitation) will produce a fast, high amplitude voltage pulse. Figure 5.29 shows a superposition of some typical output signals from a silicon photomultiplier, which has been obtained with the same dark pulses used for noise characterization. The clear distinction between the separate photo electron (PE) levels (1, 2, 3, 4, 5 PEs) illustrates the excellent pulse height resolution of the device.

The average pulse shapes of a very stable silicon photomultiplier are shown in figure 5.30a at different temperatures and in figure 5.30b at different

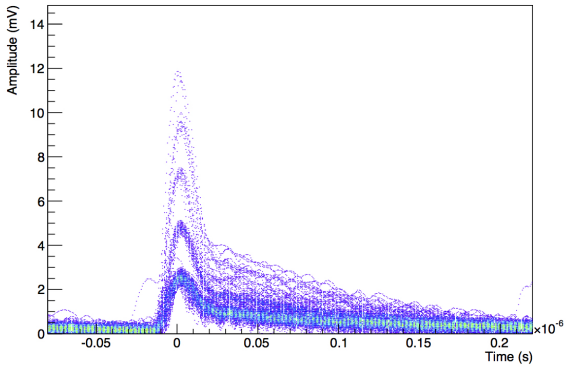

Figure 5.29: Superposition of signals with a different number of thermal electrons from a silicon photomultiplier.

overvoltages. Each one is the average of many dark pulses obtained by the oscilloscope waveforms.

The superposition of SiPM pulse shapes at different temperatures displays the thermal stability of the device under test, while the superposition of pulse shapes at different overvoltage shows the proportionality between overvoltage and device amplification. In both cases the average pulses provide important informations about rise and fall times of silicon photomultiplier pulses.

5.4.2 Gain Results and Data Analysis

As mentioned previously, the gain of a silicon photomultiplier and the equivalent capacitance of each its cells can be obtained from the charge released with the formulas:

$$Gain = \frac{Q_{PS}}{G_{OpAmp} \times e} \tag{5.8}$$

$$C_{cell} = \frac{Q_{PS}}{G_{OpAmp} \times V_{over}} \tag{5.9}$$

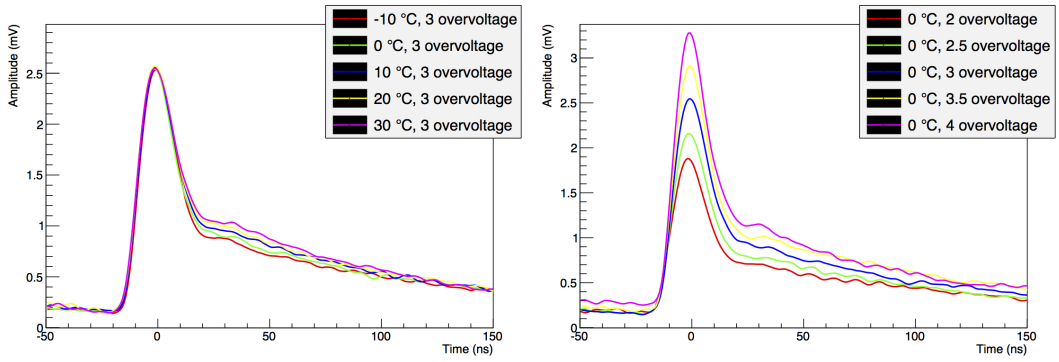

(a) (b)

Figure 5.30: Average pulse shape of 1 photoelectron from a very stable silicon photomultiplier at different temperatures (a) and overvoltage (b).

where Q_{PS} is the output charge of 1 photoelectron pulse from an operational amplifier connected in series with the SiPM, G_{OpAmp} is the internal gain of the amplifier, "e" is the electron charge and V_{over} is the set overvoltage of the device.

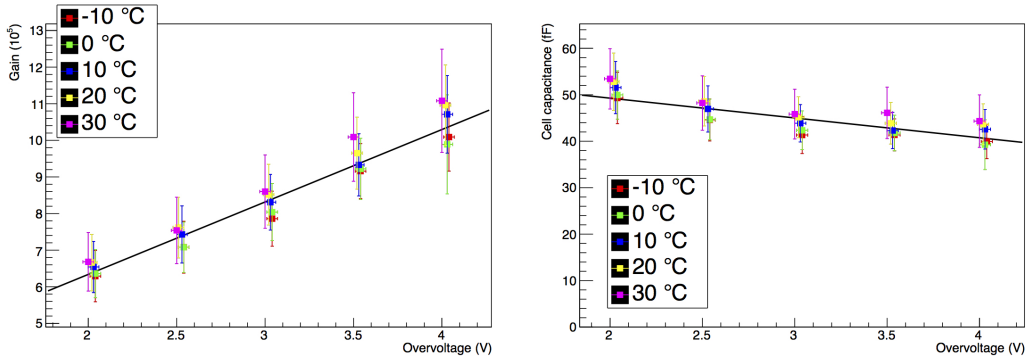

(a) (b)

Figure 5.31: Gain (a) and the cell capacitance (b) of a silicon photomultiplier as a function of overvoltage at different temperatures

From the single photon response measurements Q_{PS} can be estimated with

the Riemann sum of average pulse shape of 1 photoelectron:

$$Q_{PS} \times R_{in} = \sum V_i \times \Delta t_i \tag{5.10}$$

where R_{in} is the 50 Ω input impedance of oscilloscope and V_i is the average voltage measure in the time interval Δt_i.

Figures 5.31a and 5.31b show the gain and the cell capacitance of a silicon photomultiplier as a function of overvoltage at different temperatures with fit function.

6

Comparative Discussion of the Experimental Results

Silicon photomultipliers stand as a very promising technology to replace current photomultiplier tube (PMT) based cameras, however, the short experience of SiPMs with IACT-cameras and the large number of models offered by many companies make the selection arduous. Since the aim of this dissertation is to investigate what is being offered by different manufacturers and to perform a comparative investigation of their characteristics, the next paragraphs present the experimental results obtained with the analyses of some silicon photomultipliers and highlight the differences in the behaviour of SiPMs produced by different companies.

6.1 Experimental Results

The next subparagraphs present the most relevant results of each SiPM tested, while a complete description of all results can be found in the digital support enclosed to this dissertation.

6.1.1 FBK NUV 3x3

Device Description

The FBK NUV 3x3 device is a silicon photomultiplier based on the Near Ultra-Violet (a.k.a. NUV) detection technology developed by Fondazione Bruno Kessler (FBK), with a sensitive area of 3x3 mm^2 and a square cell pitch of 50 μm. Figure 6.1 shows the photo detection efficiency for NUV SiPMs as a function of light wavelength provided by the manufacturer.

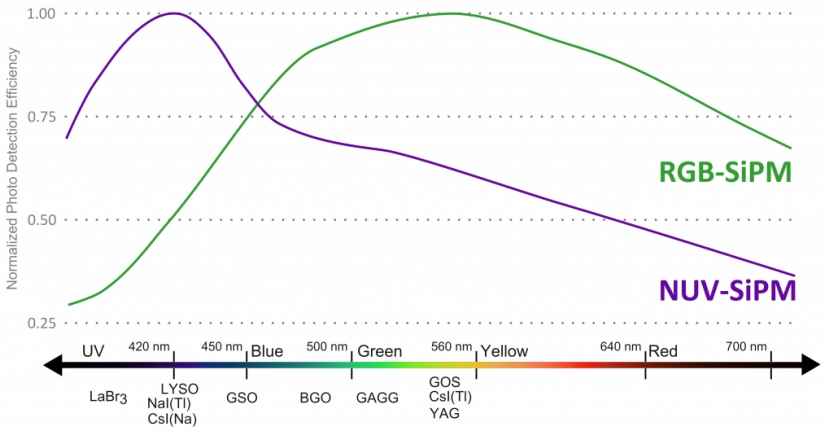

Figure 6.1: Normalized photo detection efficiency for NUV SiPMs as a function of light wavelength.

Current-Voltage Results

The analysis of voltage-current data has identified the parameters of two functions which describe the relationship between breakdown voltage and temperature (eqn.6.1) and between SiPM resistance and temperature (eqn.6.2):

$$V_{breakdown} = m_V T + q_V \tag{6.1}$$

$$R_{SiPM} = m_R T + q_R \tag{6.2}$$

where $V_{breakdown}$ is the breakdown voltage, m_V is equal to 0.021 ± 0.002 V/°C, T is the temperature, q_V is equal to 25.553 ± 0.030 V, R_{SiPM} is the SiPM's resistance, m_R is equal to -5.53 ± 0.32 Ω/°C and q_R is equal to 678.24 ± 5.25 Ω.

Figure 6.2a shows the SiPM breakdown voltage as a function of temperature, while figure 6.2b shows the SiPM resistance as a function of temperature. Both figures show also a linear fit to the data.

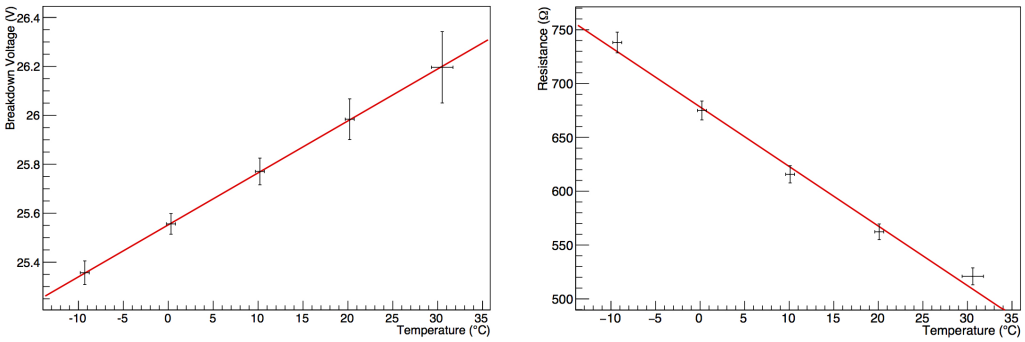

(a) (b)

Figure 6.2: SiPM's breakdown voltage (a) and resistance (b) as a function of temperature with a linear fit function.

Single Pulse Results

The typical output signals of FBK NUV 3x3 are shown in figure 6.3 which has been obtained superposing pulses acquired with the oscilloscope.

The average pulse shapes for 1 photo electron (PE) at different temperatures and bias voltage are compared in figures 6.4a and 6.4b. The superposition of SiPM pulses (fig.6.4a) clearly demonstrates the device stability at different temperatures, while the distance between peaks at different bias voltage (fig.6.4b) shows the proportionality between overvoltage and device amplification (fig.6.5a).

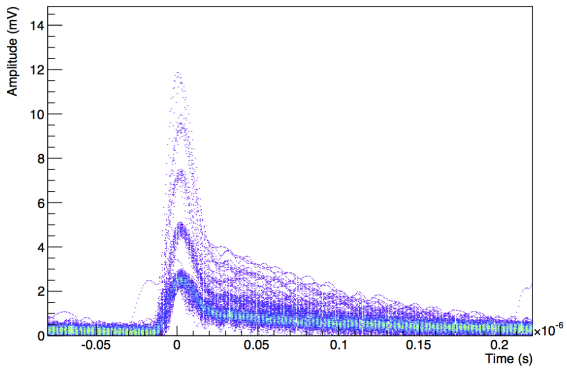

Figure 6.3: The typical output signals of FBK NUV 3x3 at 0°C and 3 V overvoltage.

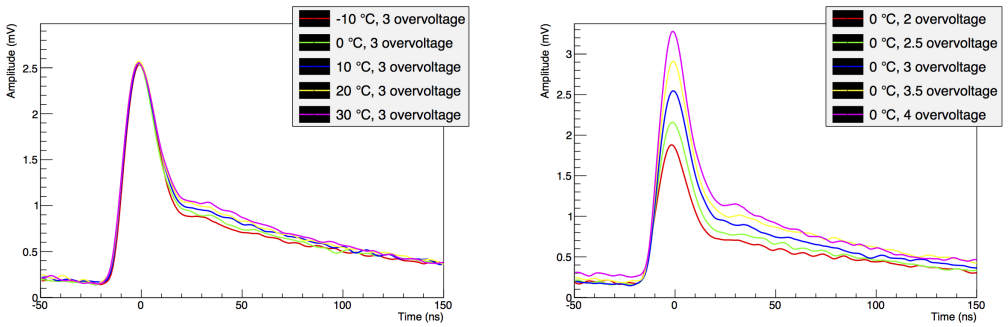

(a) (b)

Figure 6.4: The left plot shows average pulse shapes for 1 PE at different temperatures, while the right plot shows average pulse shapes for 1 PE at different overvoltages.

The gain and the cell capacitance of the silicon photomultiplier can be obtained by the analysis of average pulse shapes. Figure 6.5a shows the gain of the device as a function of overvoltage while figure 6.5b shows its cell capacitance as a function of overvoltage. The excellent thermal stability of the device allows to fit the data with the two function:

$$G = m_G \cdot V_{over} + q_G \tag{6.3}$$

$$C_{cell} = \frac{k_C}{\sqrt{V_{over} - V_C}} \tag{6.4}$$

where V_{over} is the overvoltage, G is the gain, m_G is equal to $(1.98 \pm 0.25) \cdot 10^5$ V^{-1}, q_G is equal to $(2.38 \pm 0.73) \cdot 10^5$, k_C is equal to $(99.57 \pm 15.65) \cdot 10^{-15}$ $\mathrm{F}\sqrt{\mathrm{V}}$ and V_C is equal to -1.95 ± 1.53 V.

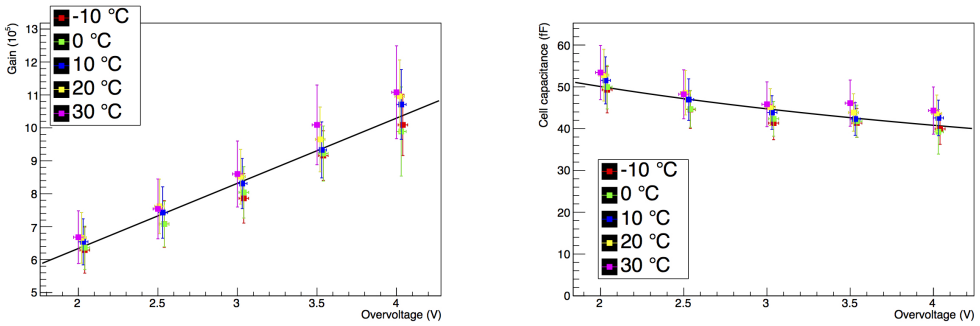

(a) (b)

Figure 6.5: Internal gain of SiPM as a function of overvoltage at different temperatures with a linear fit function (a) and cell capacitance of the device as a function of overvoltage at different temperatures with fit function 6.4.

Noise Results

The noise analysis of pulses acquired in the climate chamber allows to define some important parameters of the device. Figures 6.6a and 6.6b show the dark noise frequencies as a function of temperature and overvoltage, respectively.

In the first plot data are fitted with an exponential function, while in the second with a linear function.

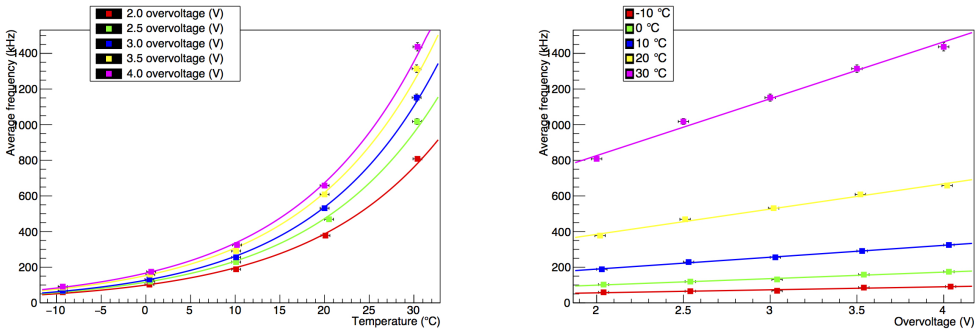

(a) (b)

Figure 6.6: The left plot shows the dark noise frequency as a function of temperature at different overvoltages, while the right plot shows the same data, but as a function of overvoltage at different temperatures.

Figure 6.7a shows the ratio between events with single cross-talk (DiCT(2pe)) and events without cross-talk (DP(1pe)) as a function of temperature, while figure 6.7b shows the ratio between event in excess of Poissonian fit in the afterpulse bump (AP+DeCT) and the integral of Poissonian fit of frequency data (PDC+DiCT).

Figures 6.8 show the probabilities to have noise events without cross-talk (a), with only one secondary avalanche (b), with more than one secondary avalanche (c) or to have afterpulses (d).

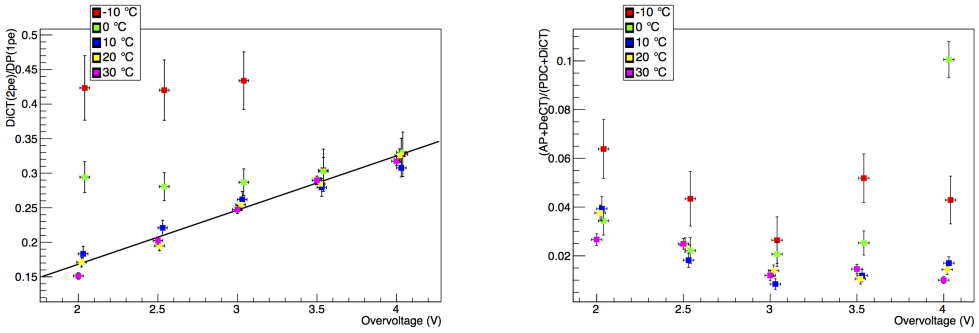

(a) (b)

Figure 6.7: Ratios between events with single cross-talk (DiCT(2pe)) and events without cross-talk (DP(1pe)) (a) and ratio between afterpulse's pulses (AP+DeCT) and the integral of frequency fit function (PDC+DiCT) (b).

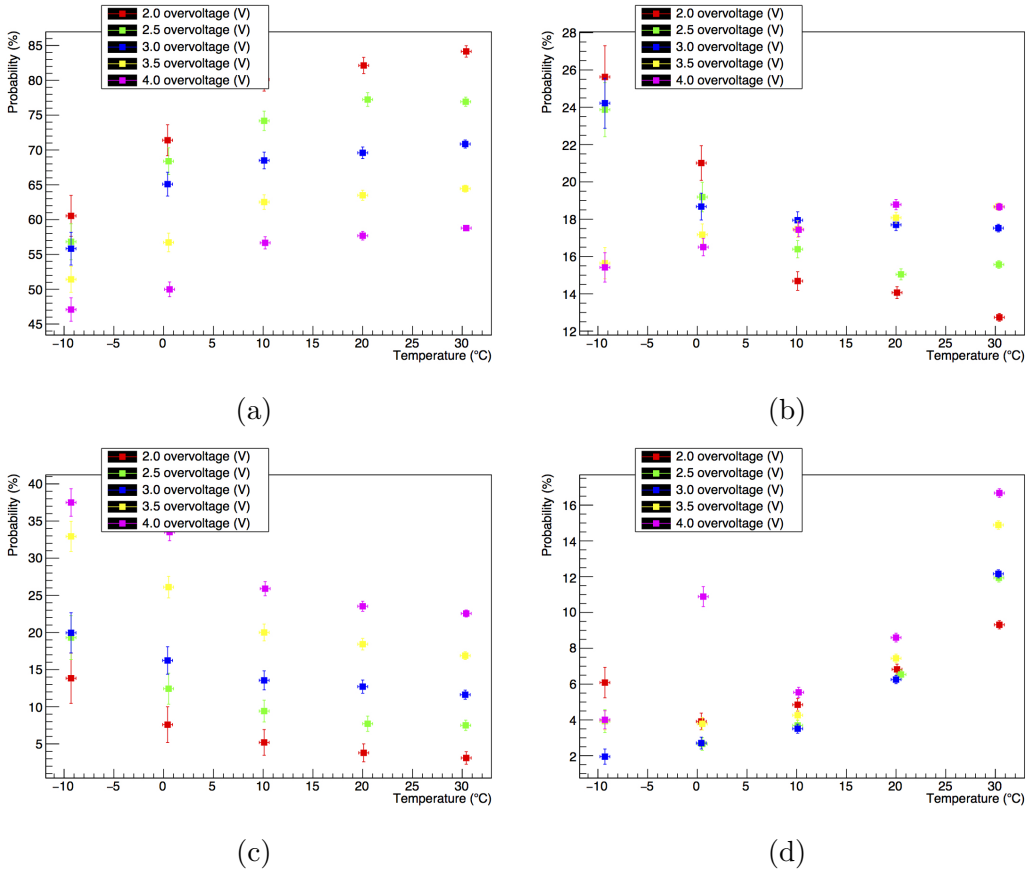

Figure 6.8: The plots show the probabilities to have noise events without cross-talk (a), with only one secondary avalanche (b), with more than one secondary avalanche (c) or to have afterpulses (d).

6.1.2 Hamamatsu S13360-3050CS

Device Description

The Hamamatsu S13360-3050CS is a silicon photomultiplier (a.k.a. multi-pixel photo counter) developed by Hamamatsu Photonics, with a sensitive area of 3x3 mm^2, a square cell pitch of 50 μm and a ceramic package. Figure 6.9 shows the photo detection efficiency of these devices as a function of light wavelength provided by the manufacturer.

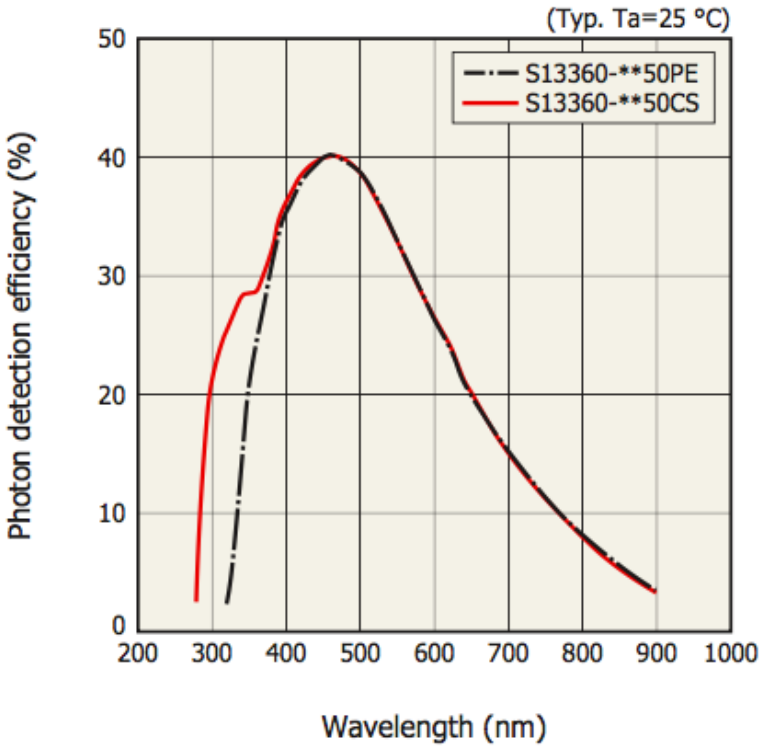

Figure 6.9: Photo detection efficiency for Hamamatsu S13360-3050CS SiPMs as a function of light wavelength (red line).

Current-Voltage Results

The analysis of voltage-current data has identified the parameters of two functions which describe the relationship between breakdown voltage and tempe-

rature (eqn.6.5) and between SiPM resistance and temperature (eqn.6.2):

$$V_{breakdown} = m_V T + q_V \tag{6.5}$$

$$R_{SiPM} = m_R T + q_R \tag{6.6}$$

where $V_{breakdown}$ is the breakdown voltage, m_V is equal to 0.048 ± 0.007 V/°C, T is the temperature, q_V is equal to 50.752 ± 0.147 V, R_{SiPM} is the SiPM's resistance, m_R is equal to -0.566 ± 0.246 Ω/°C and q_R is equal to 132.035 ± 4.277 Ω.

Figure 6.10a shows the SiPM breakdown voltage as a function of temperature, while figure 6.10b shows the SiPM resistance as a function of temperature. Both figures show also a linear fit to the data.

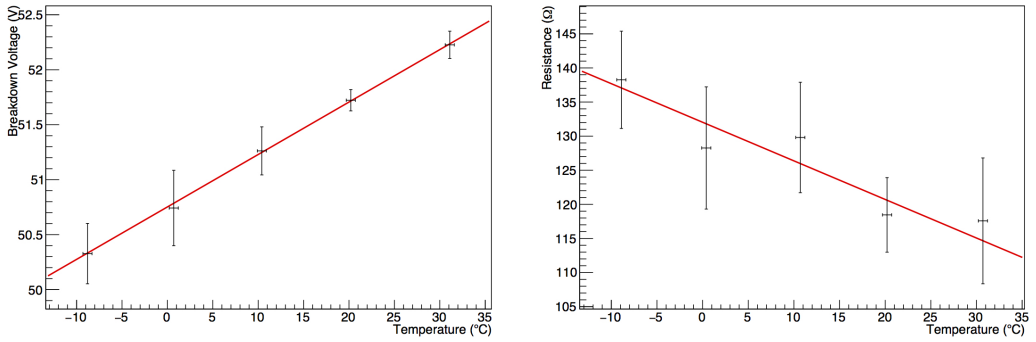

(a) (b)

Figure 6.10: SiPM's breakdown voltage (a) and resistance (b) as a function of temperature with a linear fit function.

Single Pulse Results

The typical output signals of Hamamatsu S13360-3050CS are shown in figure 6.11 which has been obtained superposing pulses acquired with the oscilloscope.

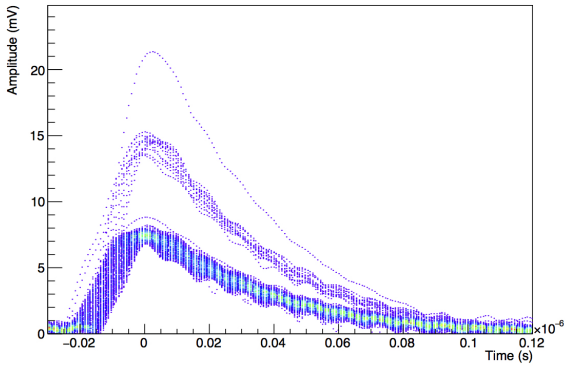

Figure 6.11: The typical output signals of Hamamatsu S13360-3050CS at 0°C and 3 V overvoltage.

The average pulse shapes for 1 photo electron (PE) at different temperatures and bias voltage are compared in figures 6.12a and 6.12b. The superposition of SiPM pulses (fig.6.12a) demonstrates the good stability of the device at different temperatures, while the distance between peaks at different bias voltage (fig.6.12b) shows the proportionality between overvoltage and device amplification (fig.6.13a).

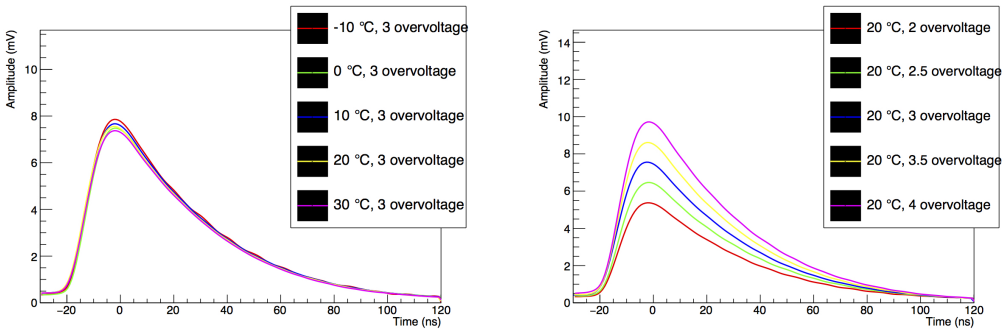

(a) (b)

Figure 6.12: The left plot shows average pulse shapes for 1 PE at different temperatures, while the right plot shows average pulse shapes for 1 PE at different overvoltages.

The gain and the cell capacitance of the silicon photomultiplier can be obtained by the analysis of average pulse shapes. Figure 6.13a shows the gain of the device as a function of overvoltage while figure 6.13b shows its cell capacitance as a function of overvoltage. The good thermal stability of the device allows to fit the data with the two function:

$$G = m_G \cdot V_{over} + q_G \tag{6.7}$$

$$C_{cell} = \frac{k_C}{\sqrt{V_{over} - V_C}} \tag{6.8}$$

where V_{over} is the overvoltage, G is the gain, m_G is equal to $(5.59 \pm 0.49) \cdot 10^5$ V^{-1}, q_G is equal to $(4.54 \pm 1.36) \cdot 10^5$, k_C is equal to $(291.01 \pm 454.54) \cdot 10^{-15}$ $\mathrm{F}\sqrt{\mathrm{V}}$ and V_C is equal to -3.45 ± 1.97 V.

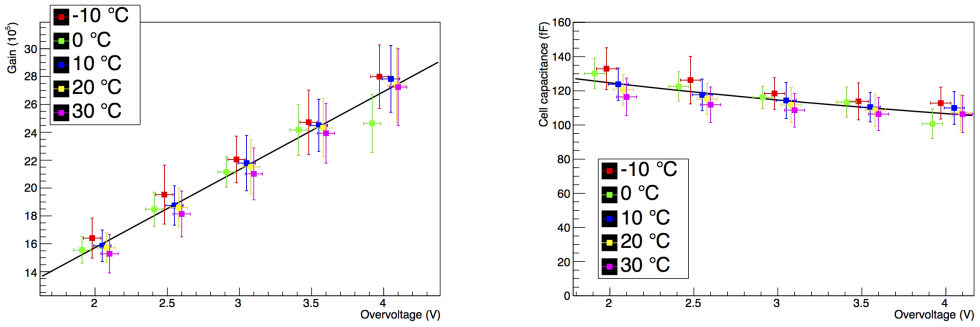

(a) (b)

Figure 6.13: Internal gain of SiPM as a function of overvoltage at different temperatures with a linear fit function (a) and cell capacitance of the device as a function of overvoltage at different temperatures with fit function 6.8.

Figure 6.14 shows a typical amplitude distribution of Hamamatsu S13360-3050CS. There is an unknown peak between 1 PE peak and 2 PE peak, which could be caused by a not-perfect uniformity of SiPM's pixels and could be a source of concern about the use of these devices.

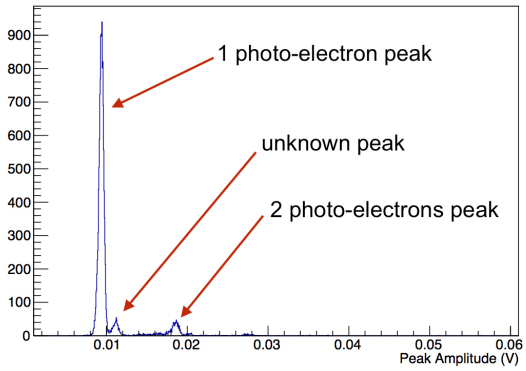

Figure 6.14: Amplitude distribution of Hamamatsu S13360-3050CS at 30°C and 4 V overvoltage.

Noise Results

The noise analysis of pulses acquired in the climate chamber allows to define some important parameters of the device. Figures 6.15a and 6.15b show the dark noise frequencies as a function of temperature and overvoltage, respectively. In the first plot data are fitted with an exponential function, while in the second with a linear function.

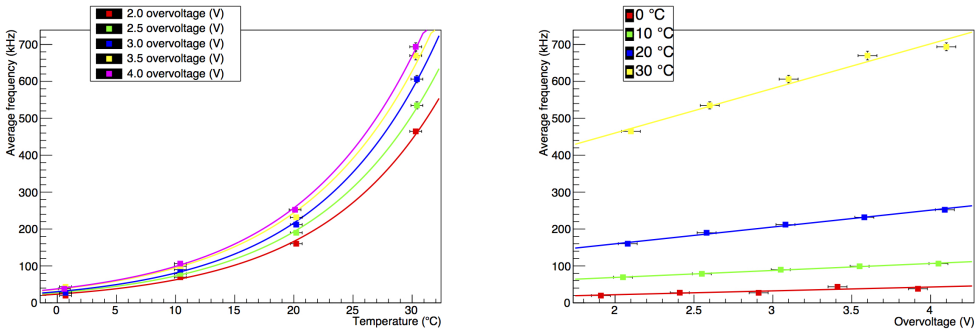

(a) (b)

Figure 6.15: The left plot shows the dark noise frequency as a function of temperature at different overvoltages, while the right plot shows the same data, but as a function of overvoltage at different temperatures.

Figure 6.16a shows the ratio between events with single cross-talk (DiCT(2pe)) and events without cross-talk (DP(1pe)) as a function of temperature, while figure 6.16b shows the ratio between event in excess of Poissonian fit in the afterpulse bump (AP+DeCT) and the integral of Poissonian fit of frequency data (PDC+DiCT).

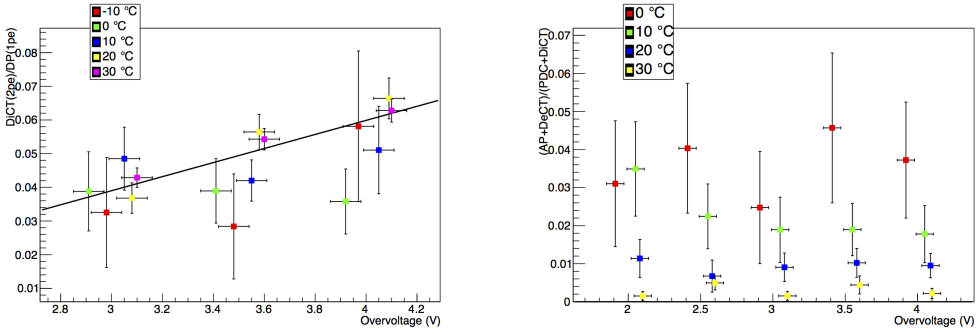

(a) (b)

Figure 6.16: Ratios between events with single cross-talk (DiCT(2pe)) and events without cross-talk (DP(1pe)) (a) and ratio between afterpulse's pulses (AP+DeCT) and the integral of frequency fit function (PDC+DiCT) (b).

6.1.3 Hamamatsu S13360-6050CS

Device Description

The Hamamatsu S13360-6050CS is a silicon photomultiplier (a.k.a. multi-pixel photo counter) developed by Hamamatsu Photonics, with a sensitive area of 6x6 mm^2 and a square cell pitch of 50 μm. Figure 6.17 shows the photo detection efficiency of these devices as a function of light wavelength provided by the manufacturer.

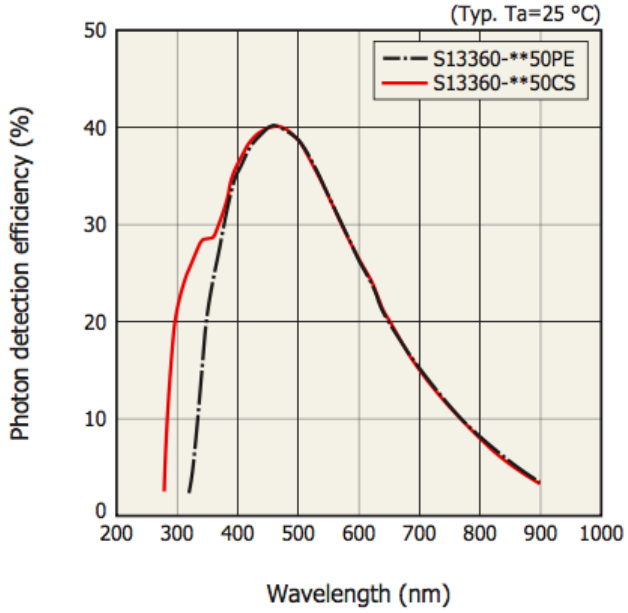

Figure 6.17: Photo detection efficiency for Hamamatsu S13360-6050CS SiPMs as a function of light wavelength (red line).

Current-Voltage Results

The analysis of voltage-current data has identified the parameters of two functions which describe the relationship between breakdown voltage and temperature (eqn.6.9) and between SiPM resistance and temperature (eqn.6.10):

$$V_{breakdown} = m_V T + q_V \tag{6.9}$$

$$R_{SiPM} = m_R T + q_R \tag{6.10}$$

where $V_{breakdown}$ is the breakdown voltage, m_V is equal to 0.048 ± 0.005 V/°C, T is the temperature, q_V is equal to 51.160 ± 0.053 V, R_{SiPM} is the SiPM's resistance, m_R is equal to -0.420 ± 0.320 Ω/°C and q_R is equal to 72.491 ± 5.219 Ω.

Figure 6.18a shows the SiPM breakdown voltage as a function of temperature, while figure 6.18b shows the SiPM resistance as a function of temperature. Both figures show also a linear fit to the data.

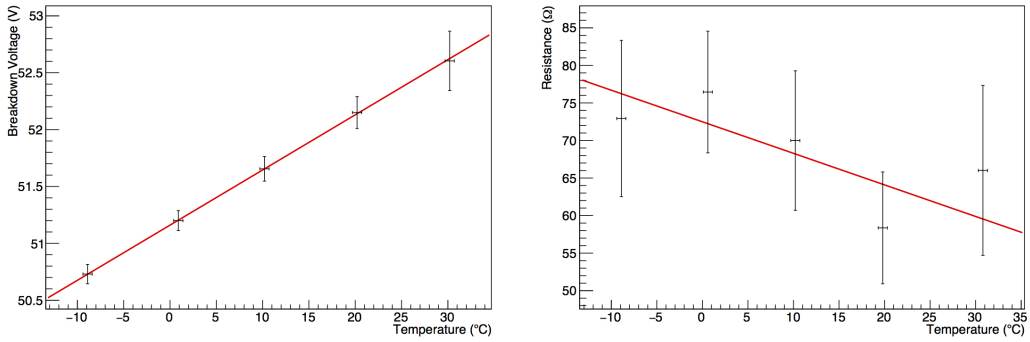

(a) (b)

Figure 6.18: SiPM's breakdown voltage (a) and resistance (b) as a function of temperature with a linear fit function.

Single Pulse Results

The typical output signals of Hamamatsu S13360-6050CS are shown in figure 6.19 which has been obtained superposing pulses acquired with the oscilloscope.

The average pulse shapes for 1 photo electron (PE) at different temperatures and bias voltage are compared in figures 6.20a and 6.20b. The

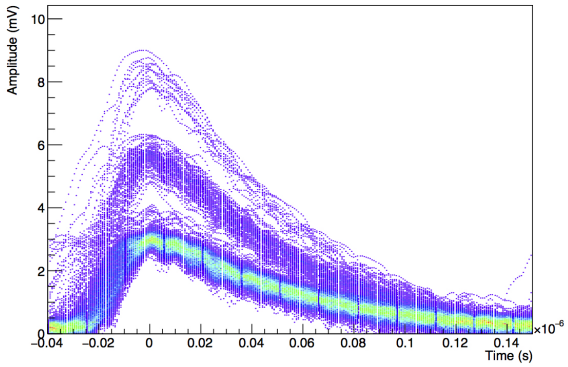

Figure 6.19: The typical output signals of Hamamatsu S13360-6050CS at 0°C and 2.5 V overvoltage.

superposition of SiPM pulses (fig.6.20a) shows the variability of the device at different temperatures, while the distance between peaks at different bias voltage (fig.6.20b) shows the proportionality between overvoltage and device amplification (fig.6.21a).

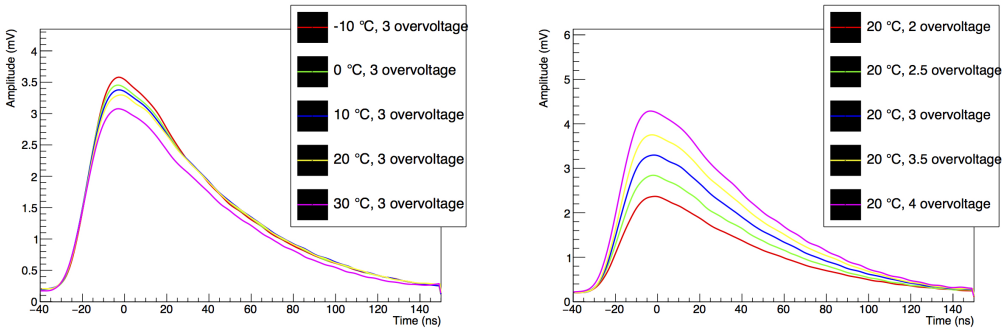

(a) (b)

Figure 6.20: The left plot shows average pulse shapes for 1 PE at different temperatures, while the right plot shows average pulse shapes for 1 PE at different overvoltages.

The gain and the cell capacitance of the silicon photomultiplier can be obtained by the analysis of average pulse shapes. Figure 6.21a shows the gain

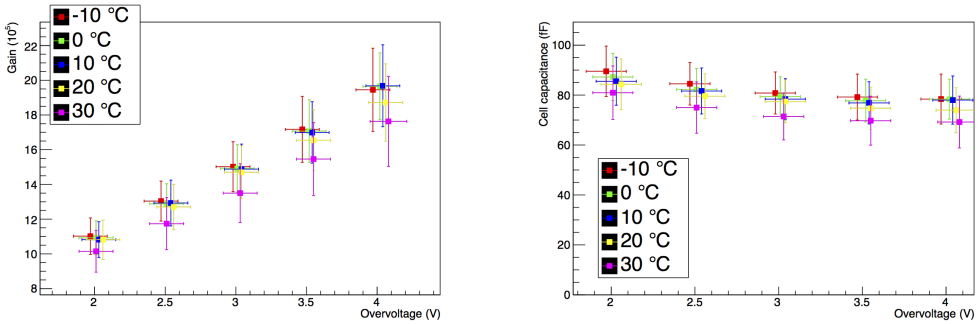

(a) (b)

Figure 6.21: Internal gain of SiPM (a) and cell capacitance of the device (b) as a function of overvoltage at different temperatures.

of the device as a function of overvoltage while figure 6.21b shows its cell capacitance as a function of overvoltage.

Figure 6.22 shows a typical amplitude distribution of Hamamatsu S13360-6050CS. There is an unknown peak between 1 PE peak and 2 PE peak, which could be caused by a not-perfect uniformity of SiPM's pixels and could be a source of concern about the use of these devices.

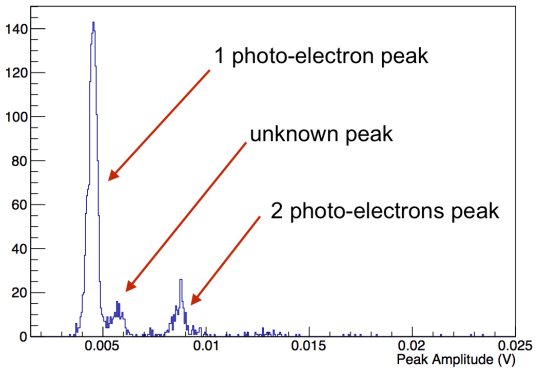

Figure 6.22: Amplitude distribution of Hamamatsu S13360-6050CS at -10°C and 4 V overvoltage.

Noise Results

The noise analysis of pulses acquired in the climate chamber allows to define some important parameters of the device. Figures 6.23a and 6.23b show the dark noise frequencies as a function of temperature and overvoltage, respectively. In the first plot data are fitted with an exponential function, while in the second with a linear function.

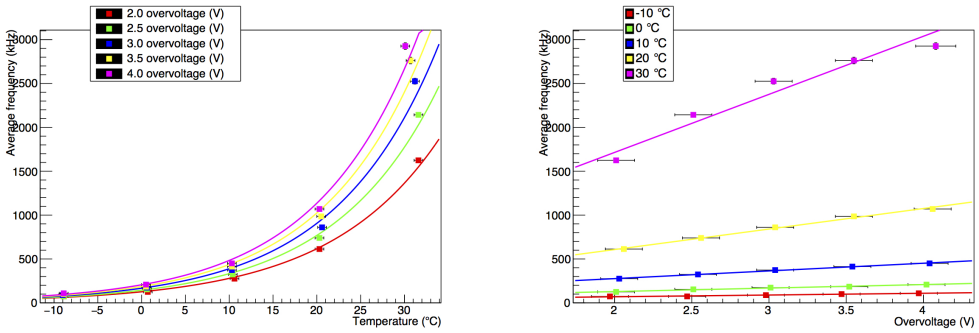

(a) (b)

Figure 6.23: The left plot shows the dark noise frequency as a function of temperature at different overvoltages, while the right plot shows the same data, but as a function of overvoltage at different temperatures.

Figure 6.24a shows the ratio between events with single cross-talk (DiCT(2pe)) and events without cross-talk (DP(1pe)) as a function of temperature, while figure 6.24b shows the ratio between event in excess of Poissonian fit in the afterpulse bump (AP+DeCT) and the integral of Poissonian fit of frequency data (PDC+DiCT).

Figures 6.25 show the probabilities to have noise events without cross-talk (a), with only one secondary avalanche (b), with more than one secondary avalanche (c) or to have afterpulses (d).

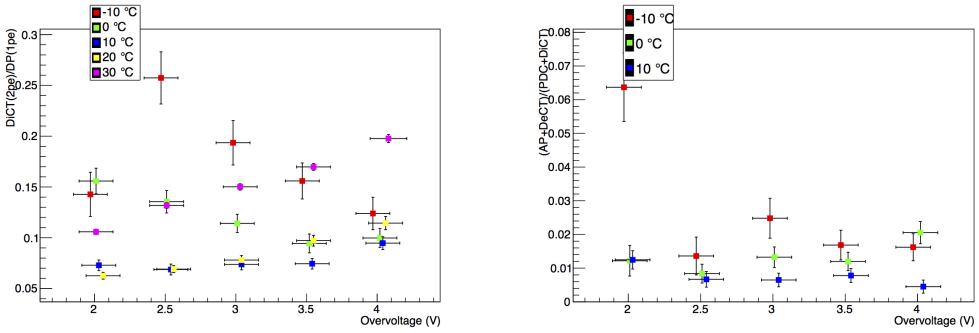

(a) (b)

Figure 6.24: Ratios between events with single cross-talk (DiCT(2pe)) and events without cross-talk (DP(1pe)) (a) and ratio between afterpulse's pulses (AP+DeCT) and the integral of frequency fit function (PDC+DiCT) (b).

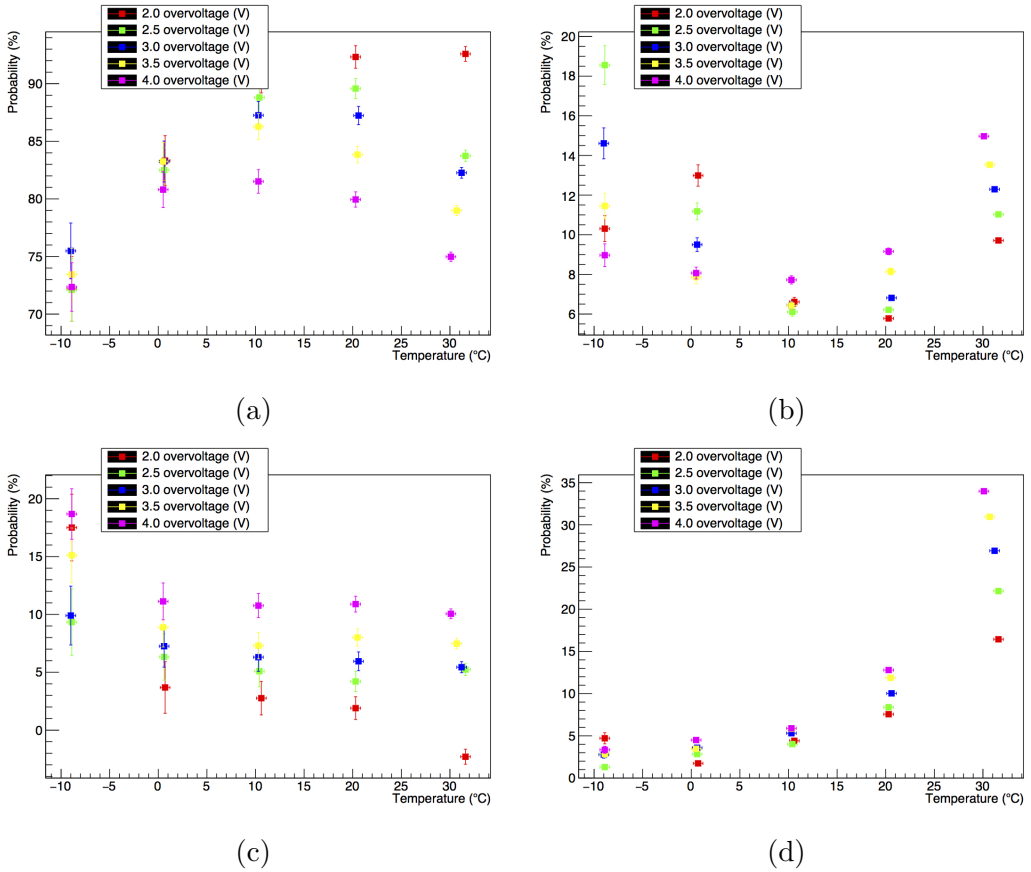

Figure 6.25: The plots show the probabilities to have noise events without cross-talk (a), with only one secondary avalanche (b), with more than one secondary avalanche (c) or to have afterpulses (d).

6.1.4 FBK RGB 3x3

Device Description

The FBK RGB 3x3 device is a silicon photomultiplier based on the Red-Green-Blue (a.k.a. RGB) detection technology developed by Fondazione Bruno Kessler (FBK), with a sensitive area of 3x3 mm^2 and a square cell pitch of 50 μm. Figure 6.26 shows the photo detection efficiency for RGB SiPMs as a function of light wavelength provided by the manufacturer.

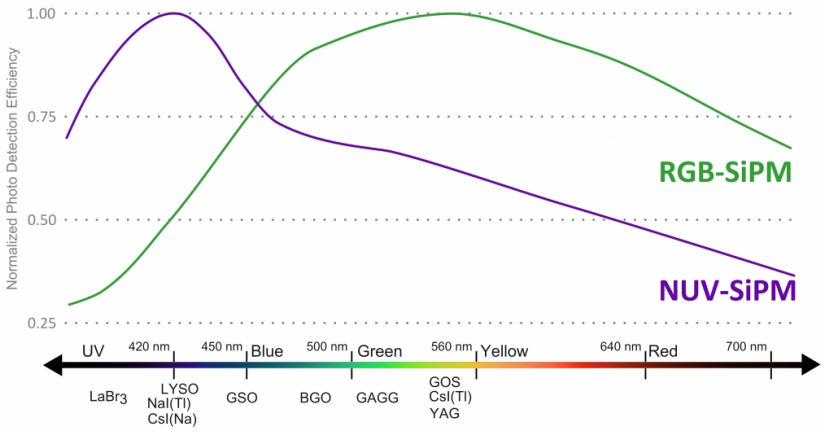

Figure 6.26: Normalized photo detection efficiency for FBK RGB 3x3 SiPMs as a function of light wavelength.

Current-Voltage Results

The analysis of voltage-current data has identified the parameters of two functions which describe the relationship between breakdown voltage and temperature (eqn.6.11) and between SiPM resistance and temperature (eqn.6.12):

$$V_{breakdown} = m_V T + q_V \tag{6.11}$$

$$R_{SiPM} = m_R T + q_R \tag{6.12}$$

where $V_{breakdown}$ is the breakdown voltage, m_V is equal to 0.022 ± 0.002 V/°C, T is the temperature, q_V is equal to 27.495 ± 0.022 V, R_{SiPM} is the SiPM's resistance, m_R is equal to -0.479 ± 0.463 Ω/°C and q_R is equal to 147.663 ± 8.581 Ω.

Figure 6.27a shows the SiPM breakdown voltage as a function of temperature, while figure 6.27b shows the SiPM resistance as a function of temperature. Both figures show also a linear fit to the data.

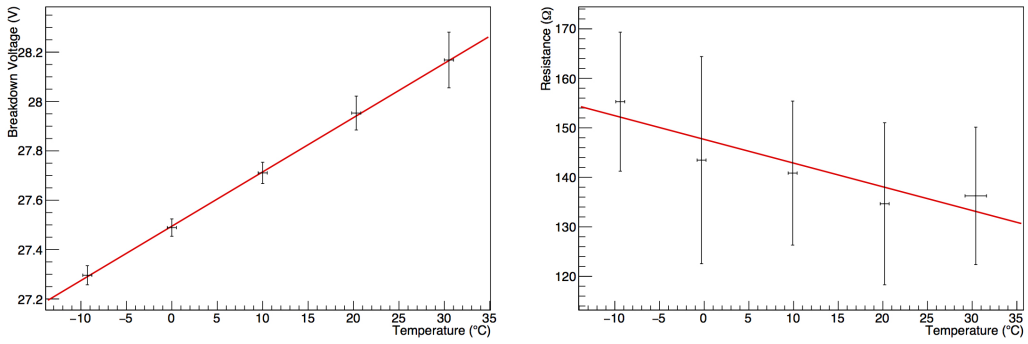

(a) (b)

Figure 6.27: SiPM's breakdown voltage (a) and resistance (b) as a function of temperature with a linear fit function.

Single Pulse Results

The typical output signals of FBK RGB 3x3 are shown in figure 6.28 which has been obtained superposing pulses acquired with the oscilloscope.

The average pulse shapes for 1 photo electron (PE) at different temperatures and bias voltage are compared in figures 6.29a and 6.29b. The superposition of SiPM pulses (fig.6.29a) demonstrates the good stability of device at different temperatures, while the distance between peaks at different bias voltage (fig.6.29b) shows the proportionality between overvoltage and device amplification (fig.6.30a).

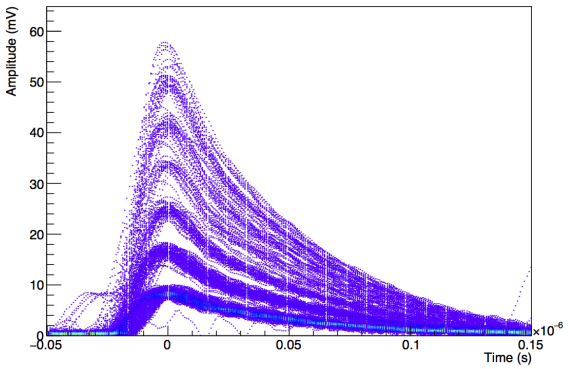

Figure 6.28: The typical output signals of FBK RGB 3x3 at -10°C and 4 V overvoltage.

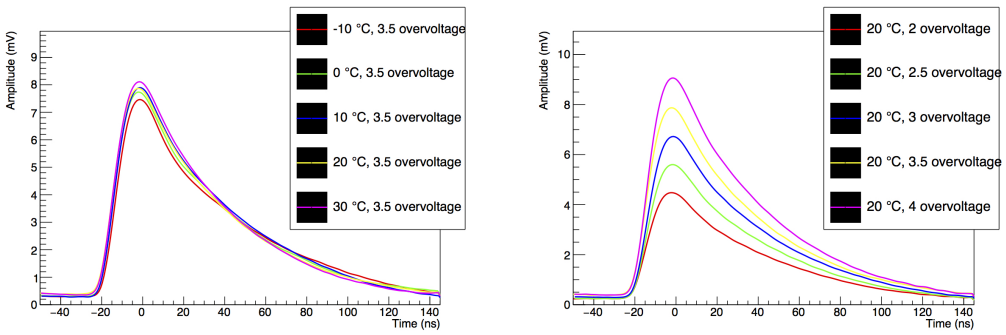

(a) (b)

Figure 6.29: The left plot shows average pulse shapes for 1 PE at different temperatures, while the right plot shows average pulse shapes for 1 PE at different overvoltages.

The gain and the cell capacitance of the silicon photomultiplier can be obtained by the analysis of average pulse shapes. Figure 6.30a shows the gain of the device as a function of overvoltage while figure 6.30b shows its cell capacitance as a function of overvoltage. The excellent thermal stability of the device allows to fit the data with the two function:

$$G = m_G \cdot V_{over} + q_G \tag{6.13}$$

$$C_{cell} = \frac{k_C}{\sqrt{V_{over} - V_C}} \tag{6.14}$$

where V_{over} is the overvoltage, G is the gain, m_G is equal to $(7.23 \pm 5.98) \cdot 10^5$ V^{-1}, q_G is equal to $(1.56 \pm 1.68) \cdot 10^5$, k_C is equal to $(572.83 \pm 328.48) \cdot 10^{-15}$ $\mathrm{F}\sqrt{\mathrm{V}}$ and V_C is equal to -18.13 ± 24.21 V.

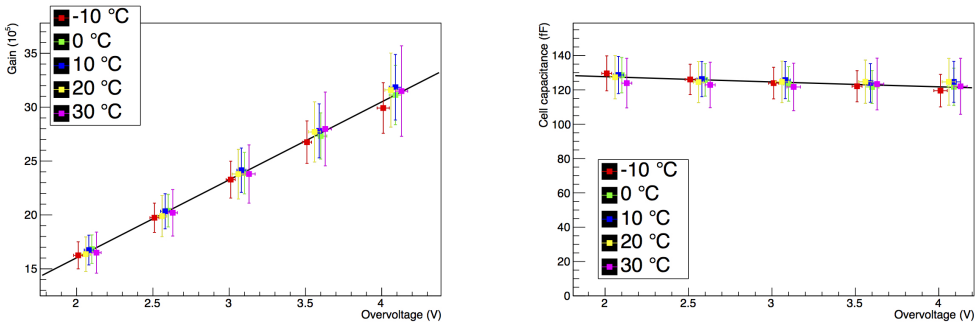

(a) (b)

Figure 6.30: Internal gain of SiPM as a function of overvoltage at different temperatures with a linear fit function (a) and cell capacitance of the device as a function of overvoltage at different temperatures with fit function 6.14.

Noise Results

The noise analysis of pulses acquired in the climate chamber allows to define some important parameters of the device. Figures 6.31a and 6.31b show the dark noise frequencies as a function of temperature and overvoltage, respec-

tively. In the first plot data are fitted with an exponential function, while in the second with a linear function.

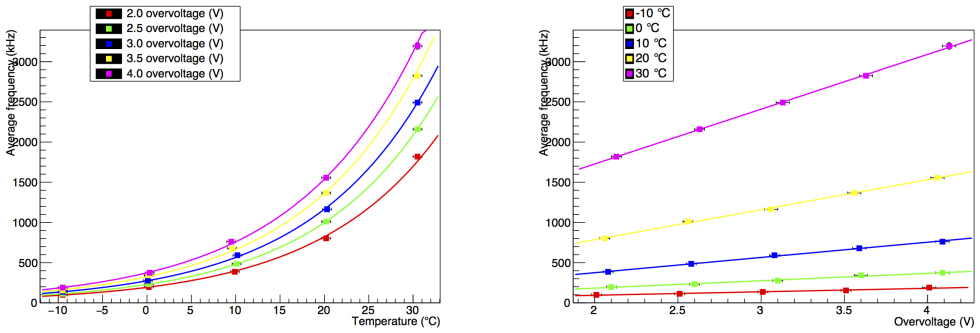

(a) (b)

Figure 6.31: The left plot shows the dark noise frequency as a function of temperature at different overvoltages, while the right plot shows the same data, but as a function of overvoltage at different temperatures.

Figure 6.32a shows the ratio between events with single cross-talk (DiCT(2pe)) and events without cross-talk (DP(1pe)) as a function of temperature, while figure 6.32b shows the ratio between event in excess of Poissonian fit in the afterpulse bump (AP+DeCT) and the integral of Poissonian fit of frequency data (PDC+DiCT).

Figures 6.33 show the probabilities to have noise events without cross-talk (a), with only one secondary avalanche (b), with more than one secondary avalanche (c) or to have afterpulses (d).

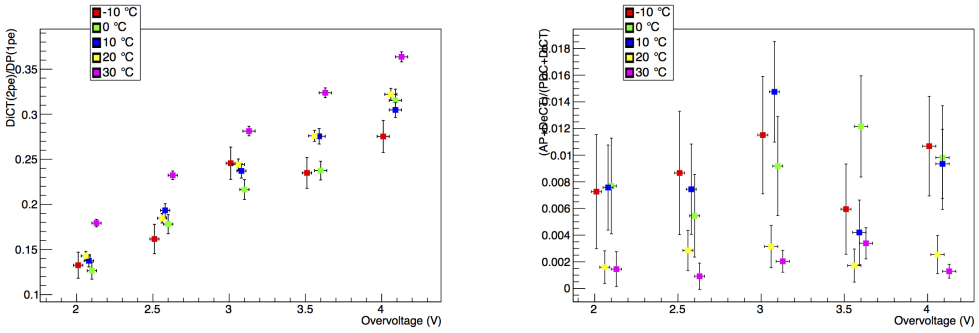

(a) (b)

Figure 6.32: Ratios between events with single cross-talk (DiCT(2pe)) and events without cross-talk (DP(1pe)) (a) and ratio between afterpulse's pulses (AP+DeCT) and the integral of frequency fit function (PDC+DiCT) (b).

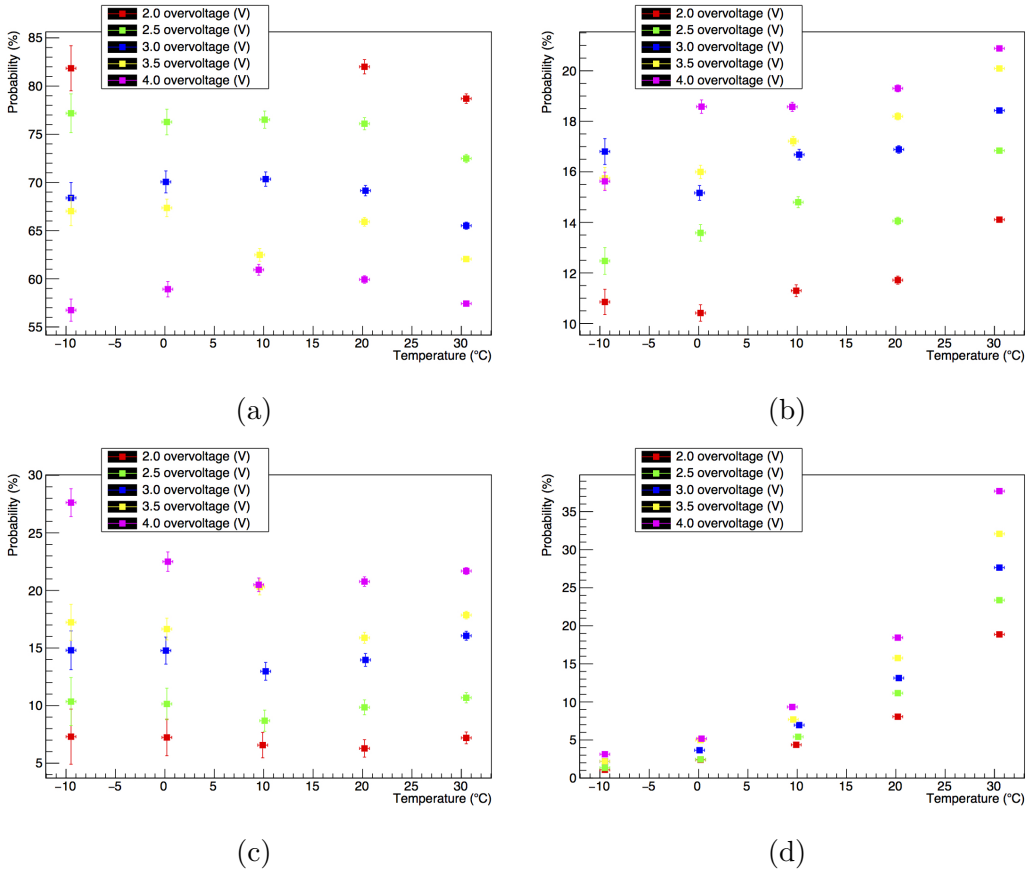

Figure 6.33: The plots show the probabilities to have noise events without cross-talk (a), with only one secondary avalanche (b), with more than one secondary avalanche (c) or to have afterpulses (d).

6.1.5 Hamamatsu S10362-11-050C

Device Description

The Hamamatsu S10362-11-050C is a silicon photomultiplier (a.k.a. multi-pixel photo counter) developed by Hamamatsu Photonics, with a sensitive area of 3x3 mm^2, a square cell pitch of 50 μm and a ceramic package. Figure 6.34 shows the photo detection efficiency of these devices as a function of light wavelength provided by the manufacturer.

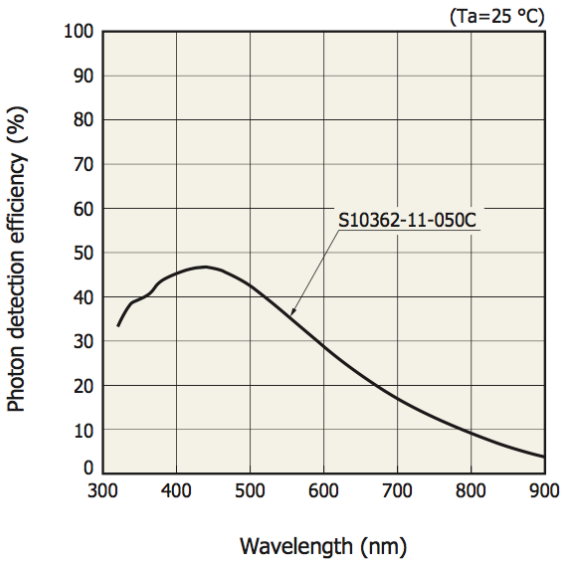

Figure 6.34: Photo detection efficiency for Hamamatsu S10362-11-050C SiPMs as a function of light wavelength.

Current-Voltage Results

The analysis of voltage-current data has identified the parameters of two functions which describe the relationship between breakdown voltage and temperature (eqn.6.15) and between SiPM resistance and temperature (eqn.6.16):

$$V_{breakdown} = m_V T + q_V \tag{6.15}$$

$$R_{SiPM} = m_R T + q_R \tag{6.16}$$

where $V_{breakdown}$ is the breakdown voltage, m_V is equal to 0.046 ± 0.003 V/°C, T is the temperature, q_V is equal to 67.331 ± 0.068 V, R_{SiPM} is the SiPM's resistance, m_R is equal to -1.582 ± 0.513 Ω/°C and q_R is equal to 336.322 ± 4.382 Ω.

Figure 6.35a shows the SiPM breakdown voltage as a function of temperature, while figure 6.35b shows the SiPM resistance as a function of temperature. Both figures show also a linear fit to the data.

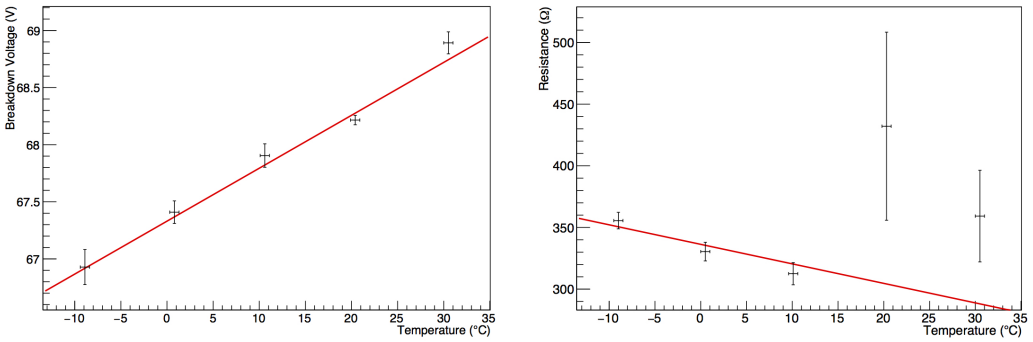

(a) (b)

Figure 6.35: SiPM's breakdown voltage (a) and resistance (b) as a function of temperature with a linear fit function.

Single Pulse Results

The typical output signals of Hamamatsu S10362-11-050C are shown in figure 6.36 which has been obtained superposing pulses acquired with the oscilloscope.

The average pulse shapes for 1 photo electron (PE) at different temperatures and bias voltage are compared in figures 6.37a and 6.37b. The superposition of SiPM pulses (fig.6.37a) shows the variability of the device at different temperatures, while the distance between peaks at different bias

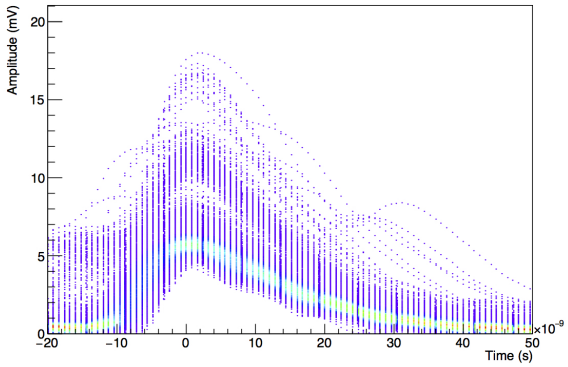

Figure 6.36: The typical output signals of Hamamatsu S10362-11-050C at 20°C and 0.9 V overvoltage.

voltage (fig.6.37b) shows the proportionality between overvoltage and device amplification (fig.6.38a).

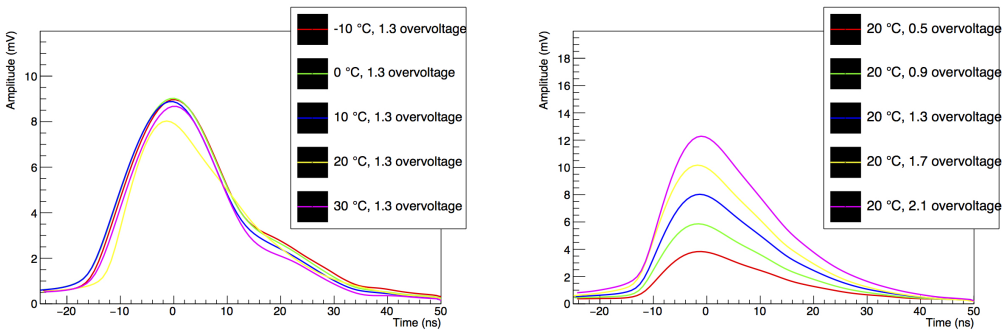

(a) (b)

Figure 6.37: The left plot shows average pulse shapes for 1 PE at different temperatures, while the right plot shows average pulse shapes for 1 PE at different overvoltages.

The gain and the cell capacitance of the silicon photomultiplier can be obtained by the analysis of average pulse shapes. Figure 6.38a shows the gain of the device as a function of overvoltage while figure 6.38b shows its cell capacitance as a function of overvoltage.

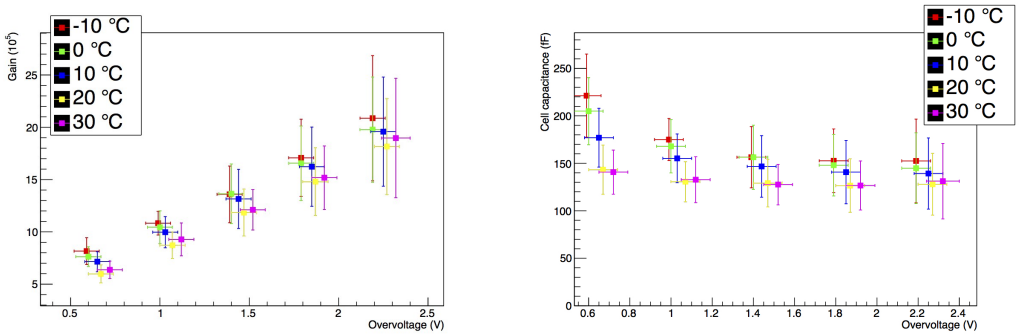

(a) (b)

Figure 6.38: Internal gain of SiPM (a) and cell capacitance of the device (b) as a function of overvoltage at different temperatures.

Figure 6.39 shows a typical amplitude distribution of Hamamatsu S10362-11-050C. There is an unknown peak between 1 PE peak and 2 PE peak, which could be caused by a not-perfect uniformity of SiPM's pixels and could be a source of concern about the use of these devices.

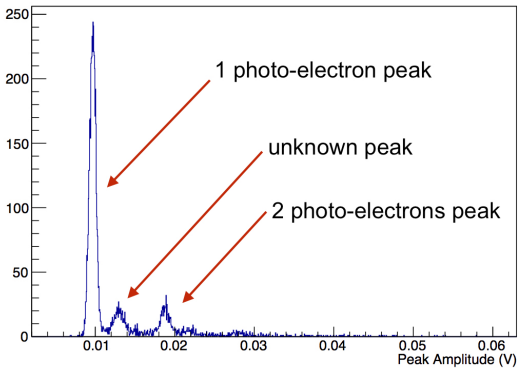

Figure 6.39: Amplitude distribution of Hamamatsu S10362-11-050C at -10°C and 4 V overvoltage.

Noise Results

The noise analysis of pulses acquired in the climate chamber allows to define some important parameters of the device. Figures 6.40a and 6.40b show the dark noise frequencies as a function of temperature and overvoltage, respectively. In the first plot data are fitted with an exponential function, while in the second with a linear function.

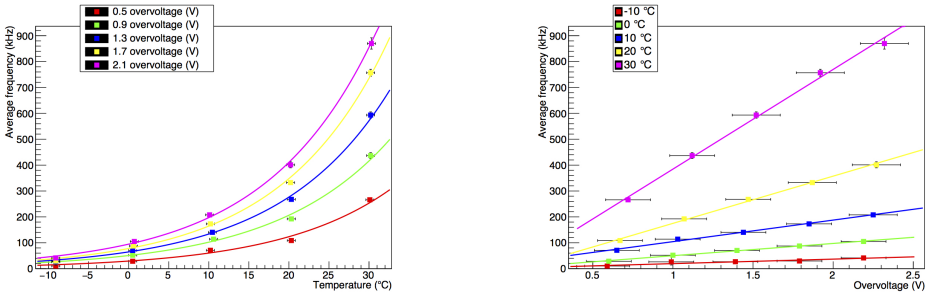

(a) (b)

Figure 6.40: The left plot shows the dark noise frequency as a function of temperature at different overvoltages, while the right plot shows the same data, but as a function of overvoltage at different temperatures.

Figure 6.41a shows the ratio between events with single cross-talk (DiCT(2pe)) and events without cross-talk (DP(1pe)) as a function of temperature, while figure 6.41b shows the ratio between event in excess of Poissonian fit in the afterpulse bump (AP+DeCT) and the integral of Poissonian fit of frequency data (PDC+DiCT).

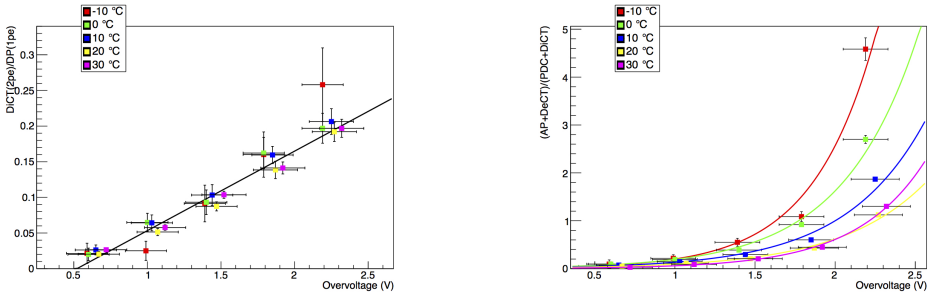

(a) (b)

Figure 6.41: Ratios between events with single cross-talk (DiCT(2pe)) and events without cross-talk (DP(1pe)) (a) and ratio between afterpulse's pulses (AP+DeCT) and the integral of frequency fit function (PDC+DiCT) (b).

6.1.6 Hamamatsu S12572-015C

Device Description

The Hamamatsu S12572-015C is a silicon photomultiplier (a.k.a. multi-pixel photo counter) developed by Hamamatsu Photonics, with a sensitive area of 3x3 mm^2, a square cell pitch of 15 μm and a ceramic package. Figure 6.42 shows the photo detection efficiency of these devices as a function of light wavelength provided by the manufacturer.

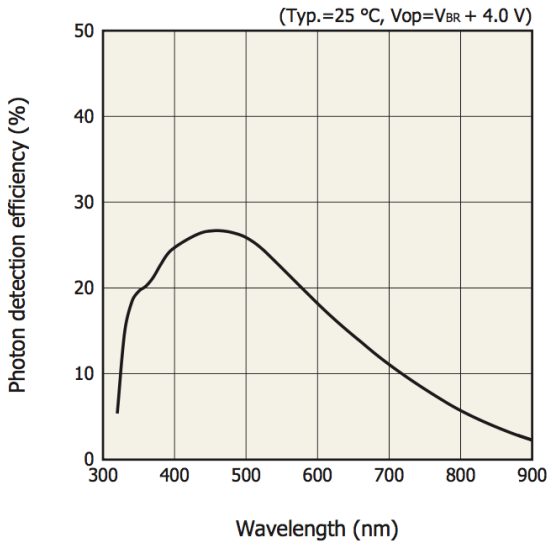

Figure 6.42: Photo detection efficiency for Hamamatsu S12572-015C SiPMs as a function of light wavelength.

Current-Voltage Results

The analysis of voltage-current data has identified the parameters of two functions which describe the relationship between breakdown voltage and temperature (eqn.6.17) and between SiPM resistance and temperature (eqn.6.18):

$$V_{breakdown} = m_V T + q_V \tag{6.17}$$

$$R_{SiPM} = m_R T + q_R \tag{6.18}$$

where $V_{breakdown}$ is the breakdown voltage, m_V is equal to 0.023 ± 0.004 V/°C, T is the temperature, q_V is equal to 63.973 ± 0.072 V, R_{SiPM} is the SiPM's resistance, m_R is equal to -0.750 ± 0.414 Ω/°C and q_R is equal to 107.865 ± 6.312 Ω.

Figure 6.43a shows the SiPM breakdown voltage as a function of temperature, while figure 6.43b shows the SiPM resistance as a function of temperature. Both figures show also a linear fit to the data.

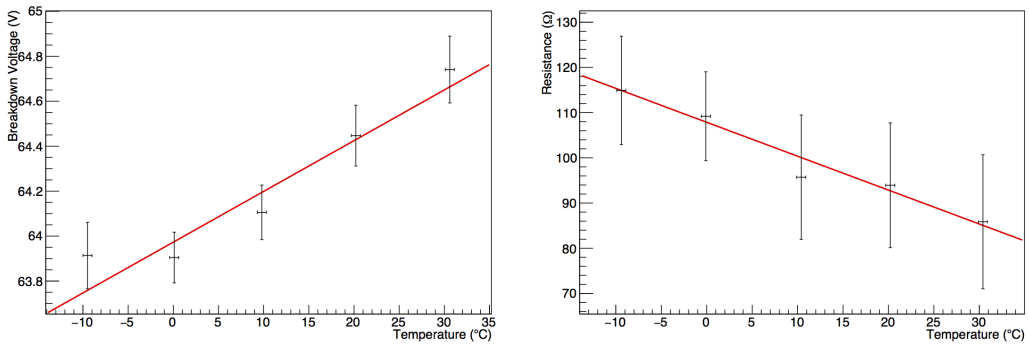

(a) (b)

Figure 6.43: SiPM's breakdown voltage (a) and resistance (b) as a function of temperature with a linear fit function.

Single Pulse Results

The typical output signals of Hamamatsu S12572-015C are shown in figure 6.44 which has been obtained superposing pulses acquired with the oscilloscope.

The average pulse shapes for 1 photo electron (PE) at different temperatures and bias voltage are compared in figures 6.45a and 6.45b. The superposition of SiPM pulses (fig.6.45a) shows the variability of the device at different temperatures, while the distance between peaks at different bias

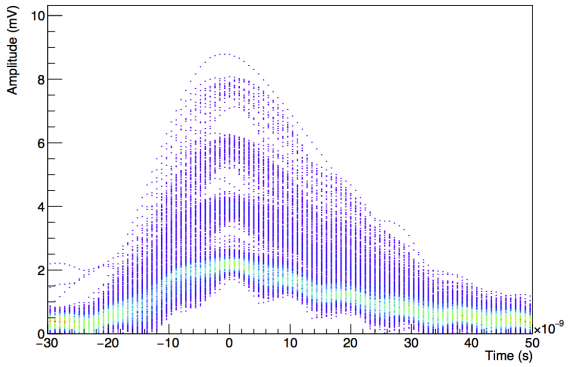

Figure 6.44: The typical output signals of Hamamatsu S12572-015C at -10°C and 4 V overvoltage.

voltage (fig.6.45b) shows the proportionality between overvoltage and device amplification (fig.6.46a).

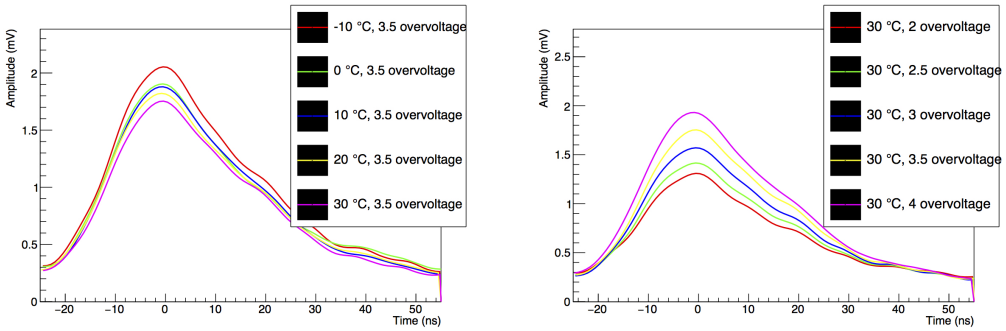

(a) (b)

Figure 6.45: The left plot shows average pulse shapes for 1 PE at different temperatures, while the right plot shows average pulse shapes for 1 PE at different overvoltages.

The gain and the cell capacitance of the silicon photomultiplier can be obtained by the analysis of average pulse shapes. Figure 6.46a shows the gain of the device as a function of overvoltage while figure 6.46b shows its cell capacitance as a function of overvoltage.

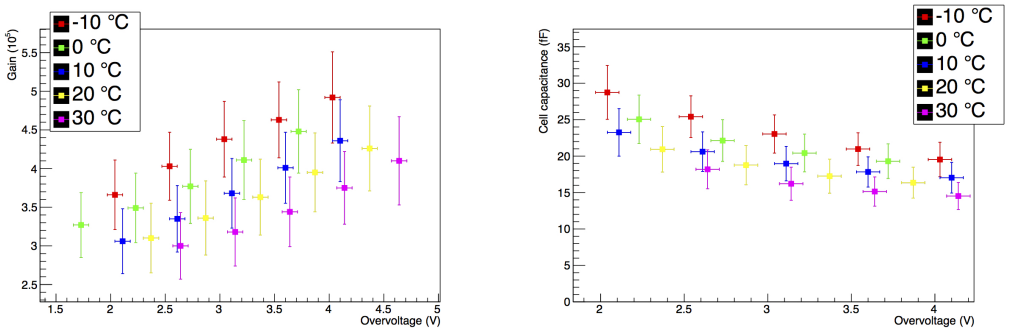

(a) (b)

Figure 6.46: Internal gain of SiPM (a) and cell capacitance of the device (b) as a function of overvoltage at different temperatures with some linear fit functions.

Noise Results

The noise analysis of pulses acquired in the climate chamber allows to define some important parameters of the device. Figures 6.47a and 6.47b show the dark noise frequencies as a function of temperature and overvoltage, respectively. In the first plot data are fitted with an exponential function, while in the second with a linear function.

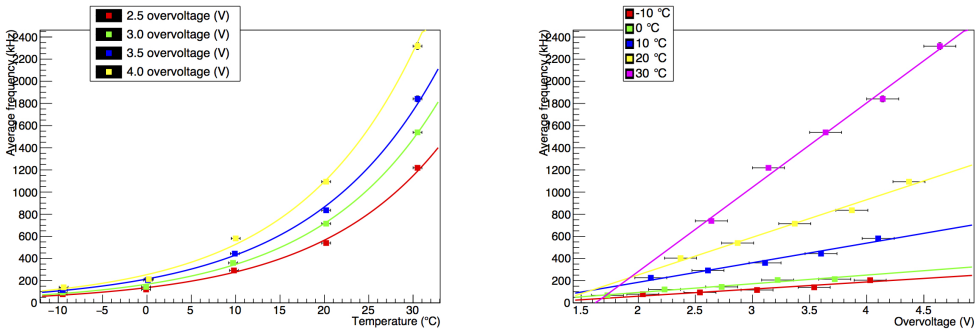

(a) (b)

Figure 6.47: The left plot shows the dark noise frequency as a function of temperature at different overvoltages, while the right plot shows the same data, but as a function of overvoltage at different temperatures.

Figure 6.48a shows the ratio between events with single cross-talk (DiCT(2pe)) and events without cross-talk (DP(1pe)) as a function of temperature, while figure 6.48b shows the ratio between event in excess of Poissonian fit in the afterpulse bump (AP+DeCT) and the integral of Poissonian fit of frequency data (PDC+DiCT).

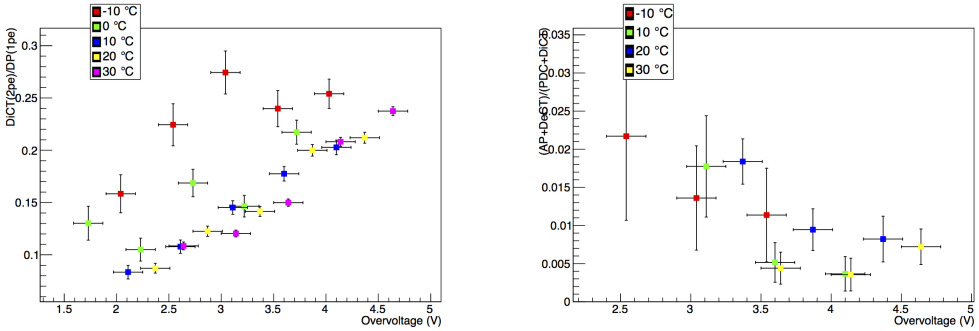

(a) (b)

Figure 6.48: Ratios between events with single cross-talk (DiCT(2pe)) and events without cross-talk (DP(1pe)) (a) and ratio between afterpulse's pulses (AP+DeCT) and the integral of frequency fit function (PDC+DiCT) (b).

Figures 6.49 show the probabilities to have noise events without cross-talk (a), with only one secondary avalanche (b), with more than one secondary avalanche (c) or to have afterpulses (d).

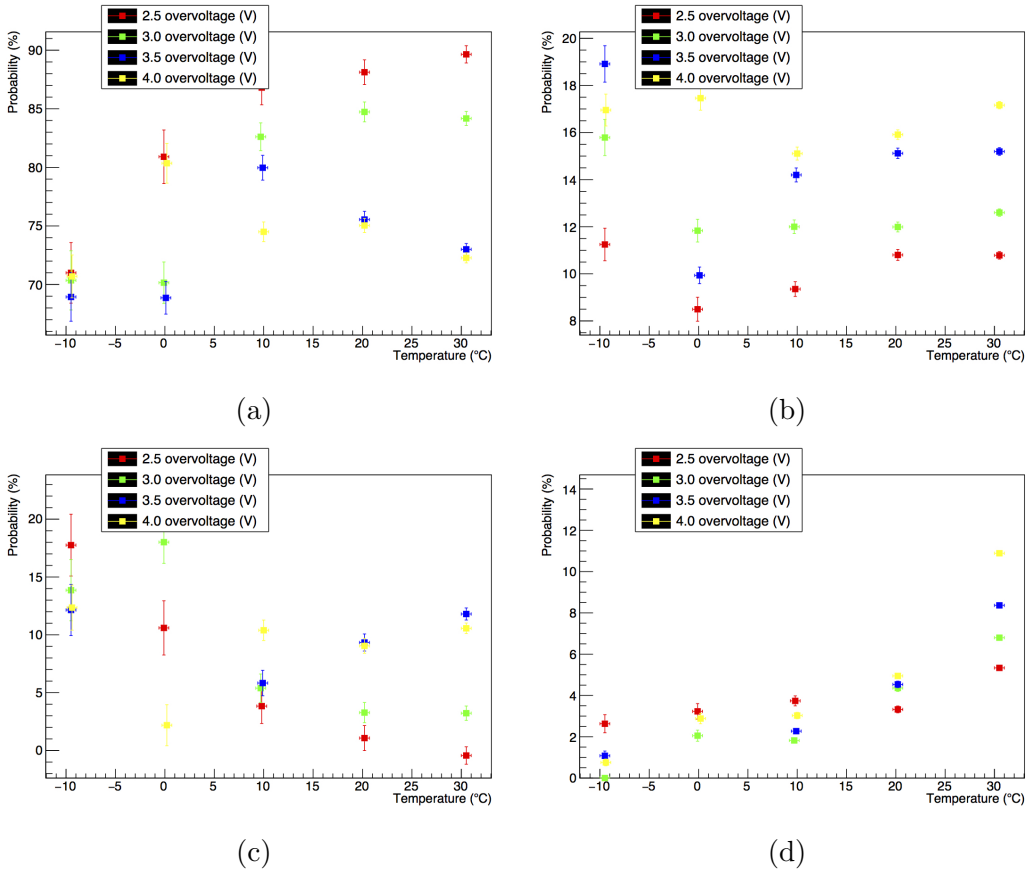

Figure 6.49: The plots show the probabilities to have noise events without cross-talk (a), with only one secondary avalanche (b), with more than one secondary avalanche (c) or to have afterpulses (d).

6.1.7 FBK NUV-HD 6x6

Device Description

The FBK NUV-HD 6x6 device is a silicon photomultiplier based on the Near Ultra-Violet (a.k.a. NUV) detection technology developed by Fondazione Bruno Kessler (FBK), with a sensitive area of 6x6 mm^2 and a square cell pitch of 30 μm. Figure 6.50 shows the photo detection efficiency for NUV SiPMs as a function of light wavelength provided by the manufacturer.

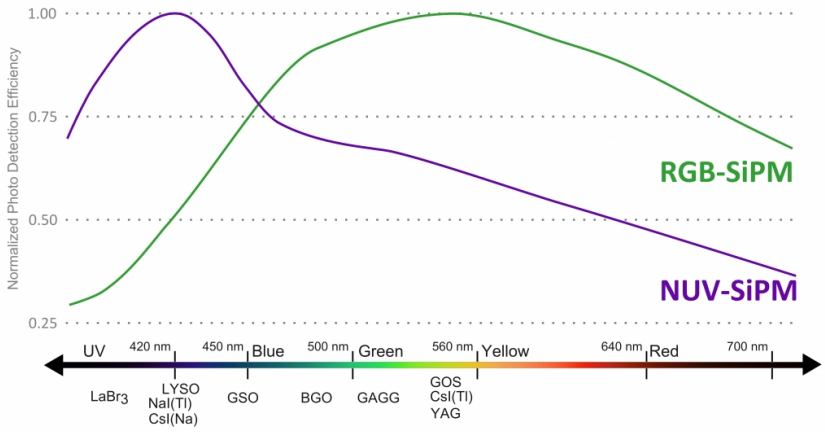

Figure 6.50: Normalized photo detection efficiency for FBK NUV-HD 6x6 SiPMs as a function of light wavelength.

Current-Voltage Results

The analysis of voltage-current data has identified the parameters of two functions which describe the relationship between breakdown voltage and temperature (eqn.6.19) and between SiPM resistance and temperature (eqn.6.20):

$$V_{breakdown} = m_V T + q_V \tag{6.19}$$

$$R_{SiPM} = m_R T + q_R \tag{6.20}$$

where $V_{breakdown}$ is the breakdown voltage, m_V is equal to 0.027 ± 0.022 V/°C, T is the temperature, q_V is equal to 27.163 ± 0.253 V, R_{SiPM} is the SiPM's resistance, m_R is equal to -0.270 ± 0.447 Ω/°C and q_R is equal to 98.856 ± 8.028 Ω.

Figure 6.51a shows the SiPM breakdown voltage as a function of temperature, while figure 6.51b shows the SiPM resistance as a function of temperature. Both figures show also a linear fit to the data.

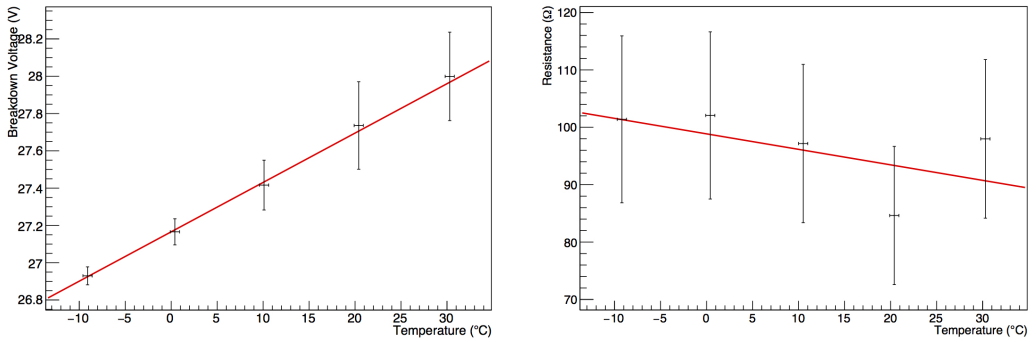

(a) (b)

Figure 6.51: SiPM's breakdown voltage (a) and resistance (b) as a function of temperature with a linear fit function.

Single Pulse Results

The typical output signals of FBK NUV-HD 6x6 are shown in figure 6.52 which has been obtained superposing pulses acquired with the oscilloscope.

The average pulse shapes for 1 photo electron (PE) at different temperatures and bias voltage are compared in figures 6.53a and 6.53b. The superposition of SiPM pulses (fig.6.53a) demonstrates the good stability of the device at different temperatures, while the distance between peaks at different bias voltage (fig.6.53b) shows the proportionality between overvoltage and device amplification (fig.6.54a).

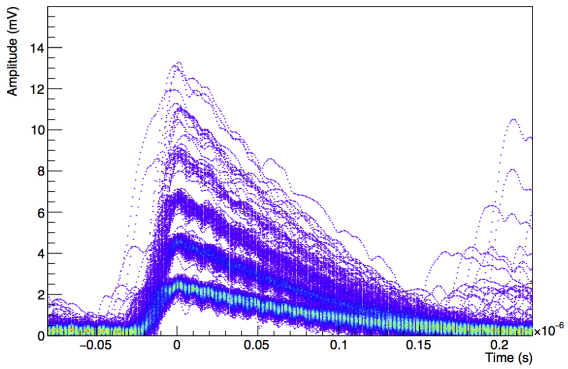

Figure 6.52: The typical output signals of FBK NUV-HD 6x6 at -10°C and 6.5 V overvoltage.

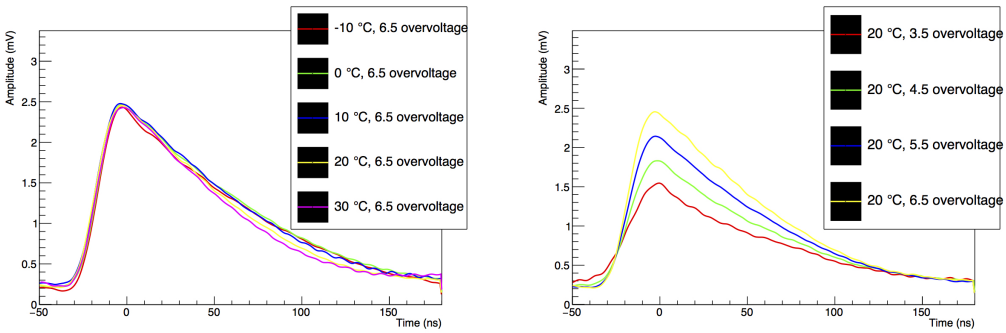

(a) (b)

Figure 6.53: The left plot shows average pulse shapes for 1 PE at different temperatures, while the right plot shows average pulse shapes for 1 PE at different overvoltages.

The gain and the cell capacitance of the silicon photomultiplier can be obtained by the analysis of average pulse shapes. Figure 6.54a shows the gain of the device as a function of overvoltage while figure 6.54b shows its cell capacitance as a function of overvoltage. The excellent thermal stability of the device allows to fit the data with the two function:

$$G = m_G \cdot V_{over} + q_G \tag{6.21}$$

$$C_{cell} = \frac{k_C}{\sqrt{V_{over} - V_C}} \tag{6.22}$$

where V_{over} is the overvoltage, G is the gain, m_G is equal to $(1.41 \pm 0.25) \cdot 10^5$ V^{-1}, q_G is equal to $(4.29 \pm 1.25) \cdot 10^5$, k_C is equal to $(92.18 \pm 13.11) \cdot 10^{-15}$ $\mathrm{F}\sqrt{\mathrm{V}}$ and V_C is equal to -1.30 ± 1.73 V.

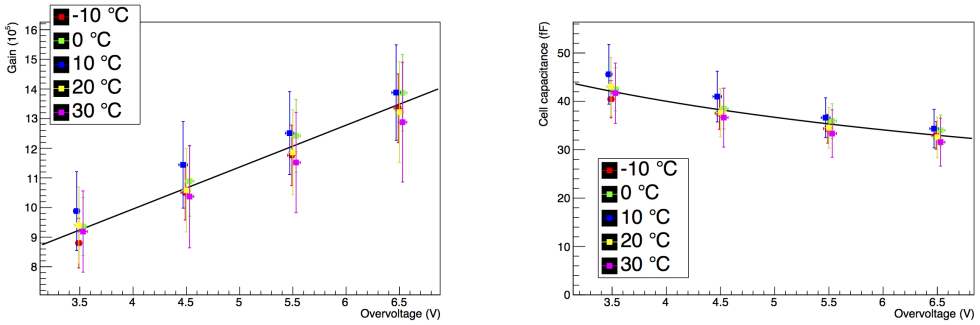

(a) (b)

Figure 6.54: Internal gain of SiPM as a function of overvoltage at different temperatures with a linear fit function (a) and cell capacitance of the device as a function of overvoltage at different temperatures with fit function 6.22.

Noise Results

The noise analysis of pulses acquired in the climate chamber allows to define some important parameters of the device. Figures 6.55a and 6.55b show the dark noise frequencies as a function of temperature and overvoltage, respec-

tively. In the first plot data are fitted with an exponential function, while in the second with a linear function.

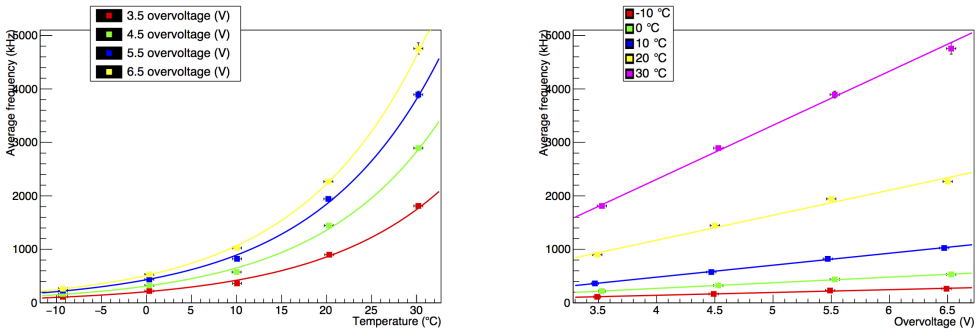

(a) (b)

Figure 6.55: The left plot shows the dark noise frequency as a function of temperature at different overvoltages, while the right plot shows the same data, but as a function of overvoltage at different temperatures.

Figure 6.56 shows the ratio between events with single cross-talk (DiCT(2pe)) and events without cross-talk (DP(1pe)) as a function of temperature, while figures 6.57 show the probabilities to have noise events without cross-talk (a), with only one secondary avalanche (b) or with more than one secondary avalanche (c).

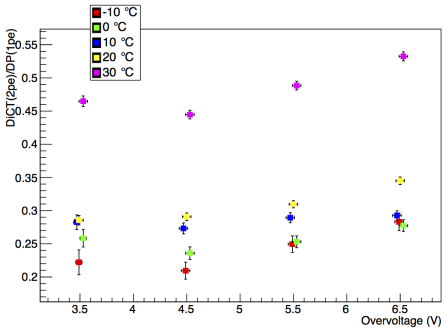

Figure 6.56: Ratios between events with single cross-talk (DiCT(2pe)) and events without cross-talk (DP(1pe)).

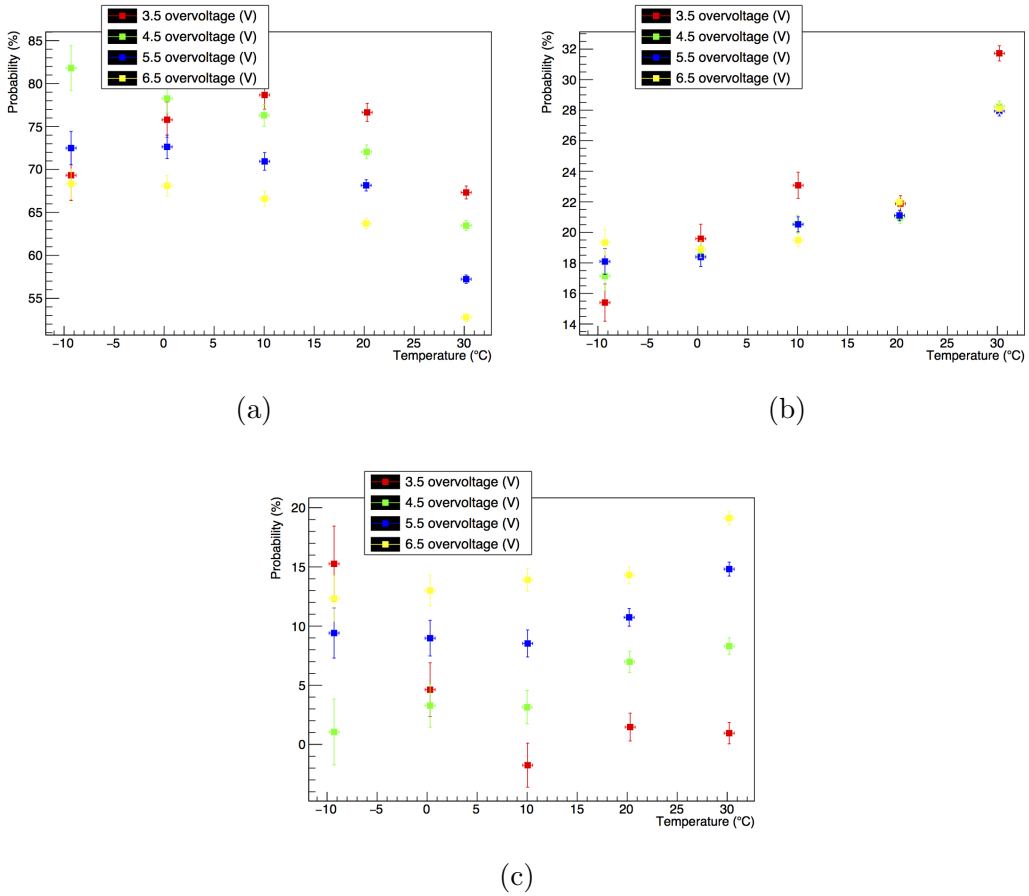

(a)

(b)

(c)

Figure 6.57: The plots show the probabilities to have noise events without cross-talk (a), with only one secondary avalanche (b) or with more than one secondary avalanche (c).

6.1.8 Summary

This subparagraph shows some summary tables of the most relevant results of each SiPM tested.

SiPM	Breakdown Voltage Function $V_{breakdown} = m_V T + q_V$		Resistance Function $R_{SiPM} = m_R T + q_R$	
	m_V (V/°C)	q_V (V)	m_R (Ω/°C)	q_R (Ω)
FBK NUV 3x3	0.021 (± 0.002)	25.553 (± 0.030)	-5.53 (± 0.32)	678.24 (± 5.25)
Hamamatsu S13360-3050CS	0.048 (± 0.007)	50.752 (± 0.147)	-0.566 (± 0.246)	132.035 (± 4.277)
Hamamatsu S13360-6050CS	0.048 (± 0.005)	51.160 (± 0.053)	-0.420 (± 0.320)	72.491 (± 5.219)
FBK RGB 3x3	0.022 (± 0.002)	27.495 (± 0.022)	-0.479 (± 0.463)	147.663 (± 8.581)
Hamamatsu S10362-11-050C	0.046 (± 0.003)	67.331 (± 0.068)	-1.582 (± 0.513)	336.322 (± 4.382)
Hamamatsu S12572-015C	0.023 (± 0.004)	63.973 (± 0.072)	-0.750 (± 0.414)	107.865 (± 6.312)
FBK NUV-HD 6x6	0.027 (± 0.022)	27.163 (± 0.253)	-0.270 (± 0.447)	98.856 (± 8.028)

Table 6.1: Summary table of current-voltage's results.

SiPM	Gain Function $G = m_G \cdot V_{over} + q_G$		Cell Capacitance Function $C_{cell} = k_C/\sqrt{V_{over} - V_C}$	
	m_G ($\cdot 10^5$ V^{-1})	q_G ($\cdot 10^5$)	k_C ($\cdot 10^{-15}$ $F\sqrt{V}$)	V_C (V)
FBK NUV 3x3	1.98 (± 0.25)	2.38 (± 0.73)	99.57 (± 15.65)	-1.95 (± 1.53)
Hamamatsu S13360-3050CS	5.59 (± 0.49)	4.54 (± 1.36)	291.01 (± 454.54)	-3.45 (± 1.97)
Hamamatsu S13360-6050CS	not available	not available	not available	not available
FBK RGB 3x3	7.23 (± 5.98)	1.56 (± 1.68)	572.83 (± 328.48)	-18.13 (± 24.21)
Hamamatsu S10362-11-050C	not available	not available	not available	not available
Hamamatsu S12572-015C	not available	not available	not available	not available
FBK NUV-HD 6x6	1.41 (± 0.25)	4.29 (± 1.25)	92.18 (± 13.11)	-1.30 (± 1.73)

Table 6.2: Summary table of gain's and cell capacitance's results.

SiPM	Overvoltage (V)	Dark Frequency (kHz)	Cross-talk ratio $\frac{\text{DiCT(2pe)}}{\text{PD(1pe)}}$	Afterpulse ratio $\frac{\text{(AP+DeCT)}}{\text{(PDC+DiCT)}}$
FBK NUV 3x3	3.02 (± 0.03)	531 (± 9)	0.254 (± 0.008)	0.013 (± 0.002)
Hamamatsu S13360-3050CS	3.08 (± 0.06)	211 (± 4)	0.037 (± 0.005)	0.009 (± 0.004)
Hamamatsu S13360-6050CS	3.04 (± 0.12)	860 (± 14)	0.078 (± 0.004)	not available
FBK RGB 3x3	3.06 (± 0.04)	1164 (± 18)	0.244 (± 0.006)	0.003 (± 0.002)
Hamamatsu S10362-11-050C	1.87 (± 0.15)	332 (± 7)	0.139 (± 0.012)	0.430 (± 0.012)
Hamamatsu S12572-015C	2.87 (± 0.14)	540 (± 10)	0.123 (± 0.005)	0.011 (± 0.003)
FBK NUV-HD 6x6	3.49 (± 0.04)	899 (± 13)	0.286 (± 0.007)	not available

Table 6.3: Summary table of noise's results at 20 °C and intermediate overvoltage. Afterpulse is the ratio between afterpulse's pulses (AP+DeCT) and the integral of frequency fit function (PDC+DiCT).

6.2 Comparative Discussion

The comparison of experimental results does not draw a silicon photomultiplier better than other devices in all features but it reveals the superiority of groups of device in specific fields. In general the hamamatsu silicon photomultipliers show a better cross-talk noise, while the SiPMs of Fondazione Bruno Kessler offer a remarkable temperature stability.

The Hamamatsu S13360-6050CS and the FBK NUV-HD 6x6 are the silicon photomultipliers which better fit the requests of CTA cameras (dimension, spectral range, photo detection efficiency, low noise, ...). For this reason they are the most interesting ones and they deserve a direct comparison of their most important parameters.

Figure 6.58 shows the breakdown voltage for 6050CS (red line) and NUV-HD (blue line). The silicon photomultiplier of Fondazione Bruno Kessler has a lower breakdown voltage, about half the Hamamatsu device, furthermore the slope of linear fit function for NUV-HD is inferior to 6050CS (tab.6.1). These two feature make the device of FBK more thermal stable and energy saver than Hamamatsu one.

Figures 6.59a and 6.59b show the pulse shape at different temperatures for the two devices. The thermal stability of pulse shape is much better for the NUV-HD than for the 6050CS. In instruments without thermal control (e.g. the camera of small-size telescope of CTA) this can be an interesting feature (for example in the design of read-out system).

Figure 6.60a shows the dark noise frequency at 30 °C for Hamamatsu 13360-6050CS (red line) and FBK NUV-HD 6x6 (blue line). For overvoltage inferior to 6 V the dark noise frequency of FBK photomultiplier is lower than Hamamatsu one, however, at same gain, the 6050CS has lower dark noise than NUV-HD (fig.6.60b).

Figures 6.61a and 6.61b show the peak amplitude distribution of FBK

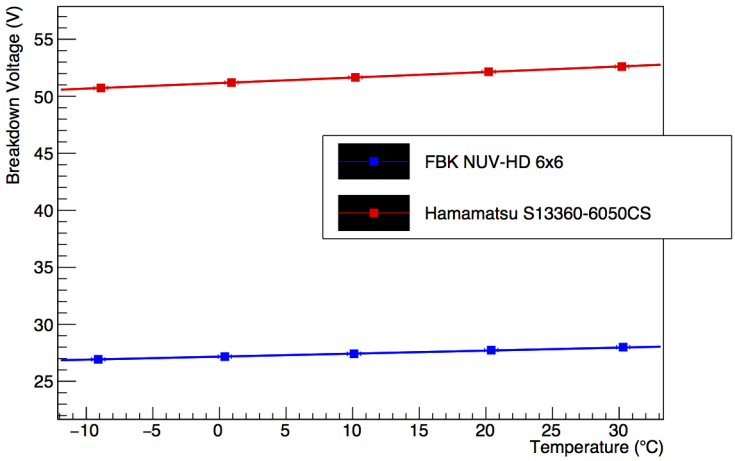

Figure 6.58: Breakdown voltage for 6050CS (red line) and NUV-HD (blue line).

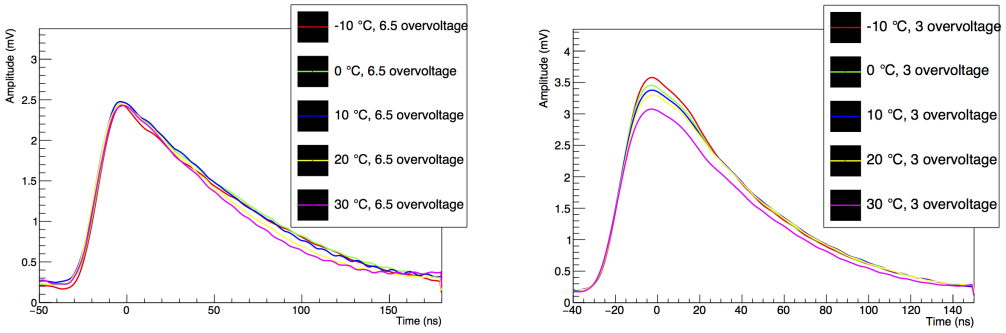

(a) (b)

Figure 6.59: Pulse shape of FBK NUV-HD 6x6 (left frame) and Hamamatsu 13360-6050CS (right frame) at different temperatures.

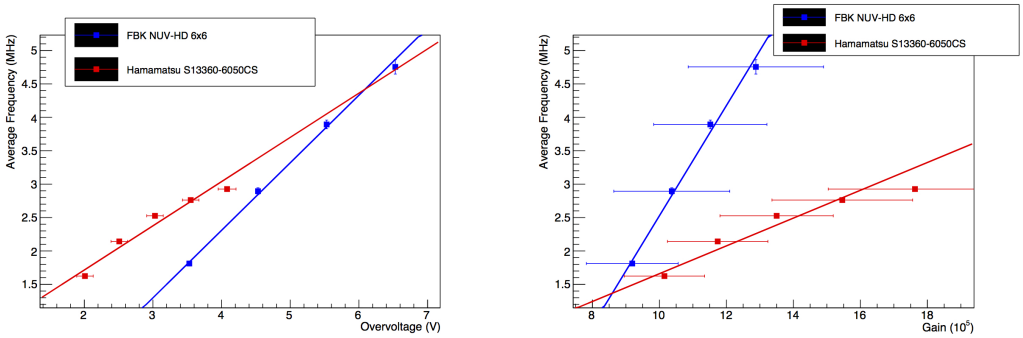

(a) (b)

Figure 6.60: Dark noise frequency at 30 °C for Hamamatsu 13360-6050CS (red line) and FBK NUV-HD 6x6 (blue line) as a function of overvoltage (left frame) and gain (right frame).

NUV-HD 6x6 and Hamamatsu 13360-6050CS at 30° C and 3.5 V overvoltage. The silicon photomultiplier of Hamamatsu produces less cross-talk than device of FBK, which is also confirmed by figure 6.24a and 6.56.

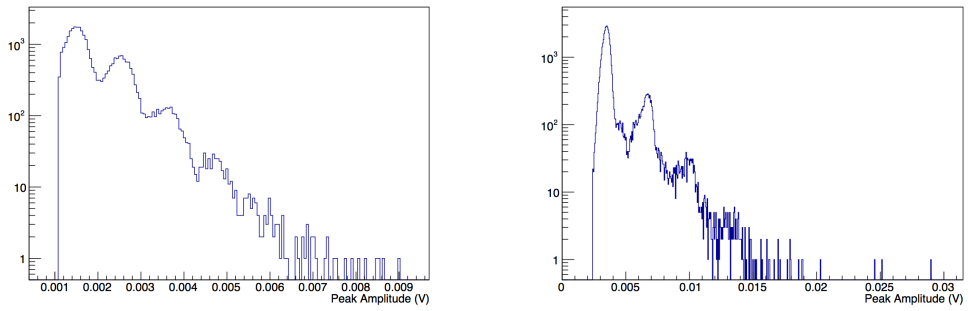

(a) (b)

Figure 6.61: Peak amplitude distribution of FBK NUV-HD 6x6 (left frame) and Hamamatsu 13360-6050CS (right frame) at 30° C and 3.5 V overvoltage.

The results of this direct comparison demonstrate that both silicon photomultipliers are good candidate for cameras of CTA telescopes. Specifically the FBK NUV-HD 6x6 is a great photo-sensor for instrument without thermal control (*i.e.* camera of CTA small-size telescope) while Hamamatsu 13360-

6050CS is a good candidate for detector with thermal control (*i.e.* camera of CTA large-size telescope). However, some doubts persist in Hamamatsu silicon photomultipliers, due to the unknown peaks in the amplitude distributions.

Conclusions

The aim of this thesis was a comparative investigation of silicon photomultipliers (SiPMs) in view of potential utilization in CTA cameras. The first phase of the study was the development of a semi-automatic test system to acquire data in a short interval of time in a practicable way, while the following phase was the acquisition and analysis of data from SiPMs under test.

One of the most interesting improvement in CTA observatory will be the use of SiPM as photon detectors for the telescope cameras. SiPMs have many key advantages compared with photomultiplier tubes, such as low voltage operation (typically $\sim$ 20 - 100 Volts), low power consumption (≤ 50 μW/mm^2), resistance to high light levels (critical to the continuation of observation during bright moonlight periods with cherenkov telescopes), excellent pulse height resolution, insensitivity to magnetic fields and single photon sensitivity. However, they have also some drawbacks, such as dark noise (fake pulses caused by random thermal excitation in the depleted region), cross-talk (by-product of a pixel avalanche is photons which can propagate inside the SiPM and generate fake avalanche in other pixels) and afterpulses (charger carriers trapped during the avalanche, which can generate a second avalanche in the same pixel).

The study of each silicon photomultiplier started with a static characterization, in order to find the breakdown voltage and the resistance of the device. Then detailed measurements of gain, single-cell signal shape and noise (dark noise, cross-talk and afterpulses) have been performed with analysis of waveforms acquired with a picoscope. Both static and dynamic properties were

studied as a function of temperature under controlled conditions by performing the measurements in a climatic chamber. Control and data acquisition were managed by LabView ad-hoc programs and, wherever possible, the procedure was automated and organized such as to enable a number of SiPMs to be characterized in sequence using a system of relays. Numerical and analytical methods were applied to the data collected, to estimate the SiPMs' characteristics.

Strengths and weaknesses of each device has been highlighted through the comparison of the experimental results, which has revealed the superiority of groups of device in specific fields. In general the Hamamatsu silicon photomultipliers show a better cross-talk noise, while the SiPMs of Fondazione Bruno Kessler offer a remarkable temperature stability. The FBK NUV-HD 6x6 and Hamamatsu S13360-6050CS are the devices which better fit the requests of CTA cameras (dimension, spectral range, photo detection efficiency, low noise, ...) among those studied. The FBK SiPM has an impressive thermal stability of pulse shape and a breakdown voltage lower than 13360-6050CS, while the cross-talk of Hamamatsu device is better than FBK one. The dark noise of two device is, instead, comparable. An unexpected peak has been observed in the amplitude distribution of Hamamatsu devices. This peak poses some unresolved questions about the behaviour of Hamamatsu silicon photomultipliers, which may be resolved with some additional test on the devices.

The acquisition set-up and the analysis software have proved their versatility, allowing to characterize silicon photomultipliers with very different features. The set-up shows some limitations in the waveforms acquisition and in the relay system, an oscilloscope with higher sample rate and an improved electronic design could remove these limitations. The analysis software doesn't show any weak point, but it could benefit from a simpler user interface than root command line.

The assembled probe station establishes a new, cheap, "fast", scalable and

modular system to define the features of silicon photomultipliers with the potential to become a useful instrument in mass SiPMs' characterization.

Bibliography

[1] R. Giacconi et al., *Evidence for x Rays From Sources Outside the Solar System*, *Phys. Rev. Lett.* **9** (1962) 439.

[2] M. S. Longair, *High Energy Astrophysics*, Cambridge University Press, Cambridge (2011).

[3] F. De Sabata, *Monte Carlo Simulations for the Čerenkov Telescope MAGIC-II and Design of a Novel Quantum Interferometer*, Ph.D. Thesis, Università di Udine, Udine Italy (2009).

[4] Magic website of ETH Institute for Particle Phisics [http://ihp-lx.ethz.ch/Stamet/magic/magic.html].

[5] O. Mansutti, *Possible Evidence for a New Light Boson from Gamma-Ray Cosmic Propagation*, Ph.D. Thesis, Università di Udine, Udine Italy (2009).

[6] A. Franceschini, G. Rodighiero, M. Vaccari, *The extragalactic optical-infrared background radiation, its time evolution and the cosmic photon-photon opacity*, Astron. Astrophys. **487** (2008) 837 [arxiv.org/abs/0805.1841v2].

[7] N. Galante, *Very High Energy observation of GRBs with the MAGIC Telescope*, Ph.D. Thesis, Università di Siena, Siena Italy.

[8] V. Scapin, *Observations of Gamma-Ray Burst Afterglows with the Magic Telescope*, Ph.D. Thesis, Università di Udine, Udine Italy (2010).

[9] F. Dazzi, *A New Stereoscopic Sum-Trigger-II for the MAGIC Telescopes*, Ph.D. Thesis, Università di Udine, Udine Italy (2012).

[10] N. Mankunzhiyil, *Magic γ-ray Observations of Distant AGN and a Study of Source Variability and the Extragalactic Background Light Using Fermi and Air Cherenkov Telescope*, Ph.D. Thesis, Università di Udine, Udine Italy (2010).

[11] The CTA Consortium, *Design Concepts for the Cherenkov Telescope Array*, (2010) [arxiv.org/abs/1008.3703v2].

[12] A. De Angelis, M. J. M. Pimenta, *Introduction to Particle and Astroparticle Physics*, Springer-Verlag, (2015).

[13] W. R. Leo, *Techniques for Nuclear and Particle Phisics Experiments*, Springer-Verlag, (1994).

[14] G. F. Knoll, *Radiation Detection and Measurement*, John Wiley & Sons, New York (1979).

[15] A. Bouvier, L. Gebremedhin, C. Johnson, A. Kuznetsov, D. A. Williams, N. Otte, R. Strausbaugh, N. Hidaka, H. Tajima, J. Hinton, R. White, M. Errando, and R. Mukherjee for the CTA consortium, *Photosensor Characterization for the Cherenkov Telescope Array: Silicon Photomultiplier versus Multi-Anode Photomultiplier Tube*, (2013), [http://arxiv.org/abs/1308.1390].

[16] C. Piemonte; Fondazione Bruno Kessler, Trento, Italy; A. Ferri; A. Gola; A. Picciotto; T. Pro; N. Serra; A. Tarolli and N.

Zorzi; *Development of an automatic procedure for the characterization of silicon photomultipliers*; Nuclear Science Symposium and Medical Imaging Conference (NSS/MIC), 2012 IEEE; 428-432; [DOI: 10.1109/NSSMIC.2012.6551141]

[17] M. Morháč, J. Kliman, V. Matoušek, M. Veselský, I. Turzo., *Background elimination methods for multidimensional gamma-ray spectra*, NIM, A401 (1997) 113-132.

[18] C. G Ryan et al., *SNIP, a statistics-sensitive background treatment for the quantitative analysis of PIXE spectra in geoscience applications*, NIM, B34 (1988), 396-402.